





### DIPLOMARBEIT

# MAXI - Macro XRF Scanning Device with mm Spot Size for A4 Area Scans

zur Erlangung des akademischen Grades

# Diplom-Ingenieur

im Rahmen des Studiums

# Technische Physik

eingereicht von

#### Patrick Kraus

Matrikelnummer: 11806478

Atominstitut der Technischen Universität Wien
Betreuung Betreuer: Ao. Univ. Prof.i.R. DiplIng. Dr. techn. Peter Wobrauschek (ATI) Mitbetreuerin: Ao.Univ.Prof. DiplIng. Dr.techn. Christina Streli (ATI)
Wien, December 17, 2024

(Unterschrift Verfasser)	(Unterschrift Betreue	r)



#### **Abstract**

The determination of the elemental composition of larger surfaces for so-called macroscopic position sensitive imaging offers use-cases in various areas like characterization of alloys or imaging of electronic boards, cultural heritage or even biological and medical uses like measurements of skin samples. One approach to measure the composition relies on the usage of Macro X-ray fluorescence (Ma-XRF) spectrometers. The sample can be area-scanned in the x/y plane by the spectrometer and the resulting elemental intensity can be converted into a map for visualization.

This thesis focuses on the further development of a macroscopic X-ray fluorescence (Ma-XRF) spectrometer named MAXI. The thesis can be segmented into three different categories: the mechanical design/construction, the implementation of safety features and improvements of the accuracy for slightly curved samples. The setup was designed around an SDD detector by KETEK and a mini-X X-ray tube by AMPTEK. The mechanical design includes an aluminium frame with guide rails, that allow the detector and the X-ray tube to be exchanged easily. The safety features protect both the measuring head and the sample by preventing possible collisions. The improvement for slightly curved samples is achieved by integrating a visual AI that automatically optimizes the z position of the system. This is realized by checking the position of two differently coloured (red and green) laser pointers. The motion control is integrated in the software which allows the user to change the x,y and z position. A new detector collimator has been designed and manufactured that results in a clean blank spectrum. The setup also allows the exchange of the detector collimator between 1mm to 3mm. The sample stage is moved by two stepper motors, that allow for movements in the x/y plane and offers enough space to fit samples up to the paper format A4  $(210mm \times 297mm)$  into the spectrometer. The stepsize can be varied to adjust the resolution according to the inputs of the user. The size of the sample stage makes it possible to mount multiple smaller samples in the spectrometer, thus serving as a sample changer. The device only requires electrical power for operation. This is achieved by using main components that do not require an external supply, like the motors, the peltier cooled detector and the air-cooled X-ray tube.

The development of the spectrometer started at the Institute of Atomic and Subatomic Physics of the TU Vienna and was concluded at the X-ray Center of the TU Vienna.

## Zusammenfassung

Die Bestimmung der elementaren Zusammensetzung größerer Oberflächen mittels makroskopischer ortssensitiver Analyse findet Anwendung in vielen verschiedenen Themenbereichen, wie die Bestimmung der elementaren Zusammensetzung von Legierungen, Scans elektronischer Platinen, Cultural Heritage bzw. auch biologische und medizinische Anwendungen wie das Scannen von Hautproben. Eine Möglichkeit diese Zusammensetzung zu vermessen beruht auf der Verwendung von makroskopischer Röngtenfluoreszenz, oder Ma-RFA, Spektrometer. Die Probe kann von dem Spektrometer in der X/Y Ebene abgerastert werden und die resultierende elementaren Intensitäten in eine Karte für Visualisierung umgewandelt werden.

Ziel dieser Arbeit ist die Weiterentwicklung eines makroskopischen Röntgenfluoreszenz (Ma-RFA) Spektrometers genannt MAXI. Die Arbeit kann in drei Segmente gegliedert werden: das mechanische Re-Design bzw. die Fertigung, die Implementierung von Sicherheitselementen und die Verbesserung der Genauigkeit von leicht gekrümmten Oberflächen. Das Testsetup wurde um einen SDD Detektor von KETEK und eine mini-X Röntgenröhre von AMPTEK designed. Im neuen Aluminiumrahmen wurden Führungen integriert, welche einen einfachen Tausch des Detektors und der Röntgenröhre erlauben. Die Sicherheitselemente schützen sowohl die Messeinheit als auch die Probe indem mögliche Kollisionen erkannt und vermieden werden. Diese Optimierung wurde mittels Integration einer grafischen KI erreicht, welche die Z-Komponente des Systems optimiert. Der relative Abstand zwischen Probe und Messeinheit wurde mit zwei verschiedenfarbenen Laserpointern (rot und grün) realisiert. Die Motorsteuerung wurde ins Gesamtprogramm integriert und ermöglicht dem Nutzer, die X,Y und Z Koordinaten einzustellen. Es wurde ein neuer Detektorkollimator hergestellt, welcher es ermöglicht ein sauberes Blank Spektrum zu erhalten. Weiters ermöglicht das Setup den Wechsel des Detektorkollimators zwischen 1mm bis 3mm. Die Probebühne kann mittels zwei Schrittmotoren in horizontaler Ebene (X/Y Achse) bewegt werden und erlauben das Abrastern einer Probe bis zum Papierformat A4 (210mm x 297mm). Die Schrittweite kann durch die Eingabe des Anwenders/der Andwenderin angepasst werden um die Auflösung einzustellen. Die Größe der Probenbühne ermöglicht es auch mehrere kleine Proben zu platzieren, daher kann man die Probenbühne als Probenwechsler verwenden. Das Spektrometer benötigt nur elektrische Spannung (240V) für den Betrieb. Dies ist ermöglicht durch die Verwendung von Spannungs- und Stromquelle, welche keine zusätzliche Versorgung, z.B. Wasserzufluss bzw. Kühlung von Flüssigstickstoff, benötigen. Dies trifft zu auf den Peltier-gekühlten Detektor, die luftgekühlte Röntgenröhre und die Motoren.

Die Entwicklung des Spektrometers hat am Atominstitut der TU Wien gestartet und wurde am Röntgenzentrum der TU Wien abgeschlossen.



# Thanks and Acknowledgments

First and foremost I want to thank my supervisor Ao. Univ. Prof. i.R. Dipl.-Ing. Dr. techn. Peter Wobrauschek for his support and unending enthusiasm during this thesis.

Moreover, I would like to thank Ao. Univ. Prof. Dipl.-Ing. Dr. techn. Christina Streli for integrating me in the group and all the nice discussions during the coffee breaks.

In addition I want to thank Dipl.-Ing. Dr.techn. Dieter Ingerle for aiding me with all software related issues.

Furthermore, I thank Dipl.-Ing. Dr.techn. Peter Kregsamer for giving advice and discussing possible solutions.

I also would like to thank Heinz Matusch and the rest of the workshop team at the ATI for their fast work on all parts that were produced during this thesis.

Additionally, I want to give my gratitude to my family and friends who supported me during my entire studies. I especially want to thank my grandfather Josef Wurm, who inspired me to learn about technology from a young age.

A special thanks is dedicated to my girlfriend, Vanessa Groiß, who never failed to support me during the most stressful phases in the last few years.

Lastly, I would like to thank and acknowledge my friends and fellow physics students who accompanied throughout my Bachelors and Masters studies: Lorenz Fischer, David Fürlinger, Andrea Pupic, Sabine Steiner, Magdalena Stelzer, Lara Brukner and Johannes Berger.

# Contents

Αŀ	ostract	2
Zι	sammenfassung	3
1	Thanks and Acknowledgments	4
2	Introduction	7
3	Theory  3.1 Generation of X-rays 3.2 Bremsstrahlung 3.3 Characteristic Radiation 3.4 Interaction between Matter and X-rays 3.5 Photoelectric Absorption 3.6 X-ray Scattering 3.7 Measuring the Fluorescence Intensity 3.8 Evaluation of Spectra 3.9 Limit of Detection 3.10 Geometric Optic 3.11 Euler Method 3.12 Machine Learning 3.13 Semiconductors 3.14 Silicon Drift Detectors	8 10 11 14 16 17 19 20 22 23 24 25 26
4	Detector and X-ray Tube4.1X-ray Tube-AMPTEK Mini X4.2Detector-KETEK Vitus H150	30 30 31
5	The Setup 5.1 Detector Collimator 5.2 Adaptation to the Measuring Head 5.3 Integration of Z Motor 5.4 Main Components of Light Barrier 5.5 Schematic of the System	35 35 36 39 42
6	<ul> <li>Z Position Optimization</li> <li>6.1 Distance dependent Loss of Counts</li> <li>6.2 Adaptation to Setup of Height Optimization</li> <li>6.3 Integration of YOLOv5</li> </ul>	44 45 46

7	Safe	ty Features of MAXI	54
	7.1	Anti Collision - Light Barrier	54
		7.1.1 Design of the Focusing Lens	55
	7.2	End Switches	59
8	Moa	surements	63
U	8.1	Determination of the spot size	
	8.2	Blank Spectrum	
	8.3	Determination of Lower Limits of Detection	
	0.0	8.3.1 500ng of Cu on Kapton Foil	
		8.3.2 800ng of Mo on Quartz Carrier	
	0.1	Quantification of Samples	
	8.4	•	
		8.4.2 NIST Soda-Lime Container Glass Standard 621	
	0 =	8.4.3 10 Euro Cent Coin	
	8.5	Ammonite	
	8.6	Analysis of a Painting	
	8.7	Mapping a Pattern in Cu	
	8.8	Determination of Resolution of the Z Optimization	
	8.9	Z Scan on Gd Screen	
		Reproducibility of Z Optimization	
		Characterization of Light Barrier	
	8.12	Collision Prevention in $y$ Direction with Light Barrier	81
9	Con	clusion and Outlook	83
•	9.1	Conclusion	
	9.2	Outlook	
	5.2	Outlook	00
10	Арр	endix	84
	10.1	Programs	84
	10.2	Drawings	87
	10.3	Setup the Light Barrier	142
		10.3.1 Removing the Light Barrier	142
		10.3.2 Mounting the Light Barrier	
		10.3.3 Adjustment of Pin Height	
		10.3.4 Angle Adjustment	
	D.1. 1	· ·	
11	Bibl	iography	146

## 2 Introduction

This work aims to redesign the macroscopic X-ray spectrometer, nicknamed MAXI, which has already been developed during the course of other projects and theses, primarily by Utz [1] and Allinger [2] at the Institute of Atomic and Subatomic Physics of the TU Vienna. One aspect of this redesign is to improve the precision of its mechanical parts. This allows for a reduced uncertainty when trying to repeat a measurement at a certain coordinate. The other requirement for this setup allows for easy maintenance and safe exchange of the tube and the detector by suitable guide rails.

Furthermore, an automation, which enables the device to adjust its z coordinate automatically, was implemented. This allows the user to capture a 2D map of samples with slight curvatures. These automatic movements also required to integrate safety measurements that prevent the device from colliding with the sample. Where possible, it was intended to integrate only low-cost components with short delivery times.

In the upcoming chapters, I will delve into the theoretical background concerning Xrays, its generation and the detection of X-rays. This is followed by a section that describes the experimental setup with a focus on the optimization of the z coordinate and the safety measurements. I conclude this work with measurement results that allow characterizing the MAXI.

# Theory

In this chapter, the theoretical basis of this thesis will be discussed. The topics of X-ray generation, interaction between matter and X-rays, fluorescence and the detector are covered.

#### 3.1 Generation of X-rays

The discovery of X-rays traces back to Wilhelm Conrad Röntgen in 1895, for which he was awarded the first Nobel Prize in Physics in 1901. In the following decades, the principles of X-rays were applied not only in medical diagnostics, but later also in the study of materials.

In 1913, Sir William Henry Bragg and Sir William Lawrence Bragg, father and son, demonstrated diffraction of X-rays by a crystal, using the first X-ray spectroscope. Their explanation led to the derivation of their famous equation:  $\lambda * n = 2 * d * sin(\theta)$ , where d is the lattice distance and  $\theta$  is the angle of incidence. In the same year Henry Moseley discovered a relationship between the wavelength of the characteristic X-rays and the atomic number of the element.

X-rays are the part of the electromagnetic radiation in the energy range of approximately 0.1-100 keV. The most common means of X-ray photon generation is done via X-ray tubes. Other means of creating X-rays are the synchrotrons, liquid metal jet and laser induced plasma sources, however, in this thesis only X-ray tubes are used, and other means of generation are not further elaborated upon. Generally, X-ray tube are evacuated cylinders in which electrons are emitted by a heated wire, the cathode, and accelerated towards the anode, which is usually on ground potential. A high voltage generator supplies the X-ray tube with high voltage that is connected to the anode and the cathode, which is in contact with ground potential. The resulting electric field causes the acceleration of the electrons. The voltage must be adjusted according to the anode material since materials with higher atomic number require more energy to create Xrays depending on the energy of the absorption edge for the relative shell considered. The conventional design for an X-ray tube uses a side window close to the anode, which has been illustrated in figure 3.1 [3]. For high power tubes, water cooling is necessary, whereas for low power tubes with a power consumption of only a few W, such as the one used in this thesis, air cooling is sufficient.

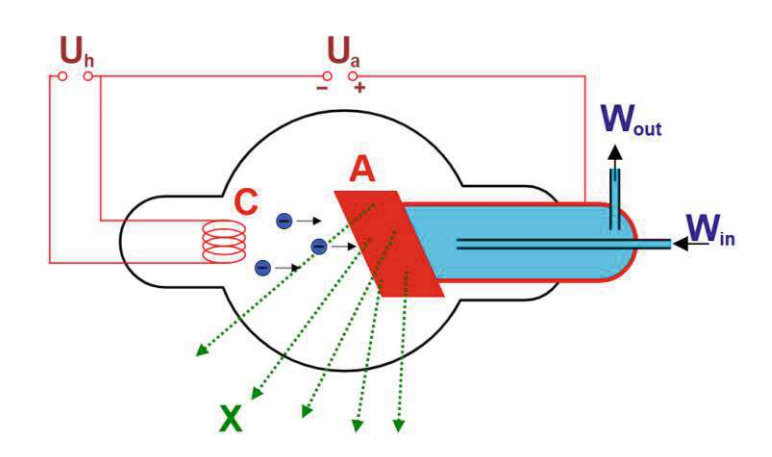


Figure 3.1: Schematic of an X-ray tube with side window.[4]

Another common design for X-ray tube is called transmission target X-ray tube, where the anode is directly located on the exit window, where the X-ray photons leave the tube. This approach allows for a more compact design with a short distance between the anode and the sample and has been used in this diploma thesis. An illustration of this design can be seen in figure 3.2.[5]

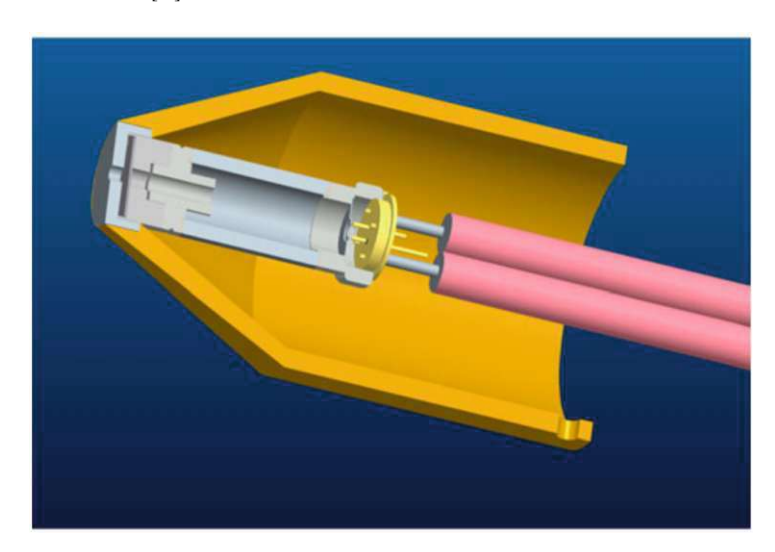


Figure 3.2: Illustration of a transmission X-ray tube.[5]

A majority of the kinetic energy of the electrons (roughly 99%) is converted into heat, while the remaining 1% generates the bremsstrahlung and characteristic radiation if the electron exceeds the binding energy of an electron bound to an atom of the target material. The resulting radiation from the tube is a superposition of these effects.

#### 3.2 Bremsstrahlung

The bremsstrahlung produces a continuous spectrum that can cover up to three orders of magnitude. This part of the spectrum is created by the deceleration of the electrons in the target when the electrons interact with the strong coulomb field of the nuclei and the electron shells. An electron can lose its energy in several steps or in a single collision and can therefore, emit a photon with the total electron energy or multiple photons corresponding to only parts of the electrons total energy. For the case of a total energy transfer in a single collision, the energy of the photon equals the elemental charge times the accelerating voltage:  $E_{max} = eU$ . Since no higher energy transfer is possible, the bremsstrahlung is cut-off at this point, which can be converted to a minimum wavelength by using:  $\lambda_{min} = \frac{hc}{eU}$ , where h is the Planck constant and c is the speed of light. This effect creates a background radiation which generally makes it more difficult to distinguish between characteristic peaks for analytical purposes, especially for lighter elements. Figure 3.3 and figure 3.4 compare the energy dispersive and wavelength dispersive representation[3].

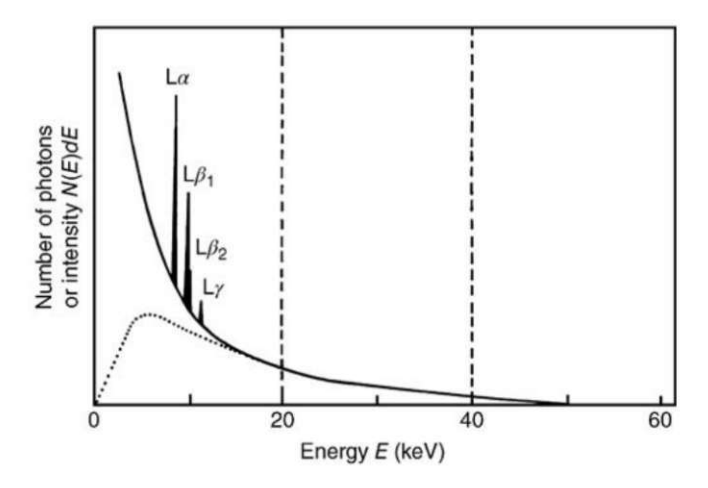


Figure 3.3: Spectrum represented in energy dispersive mode. The cut-off voltage is 50kV.[3]

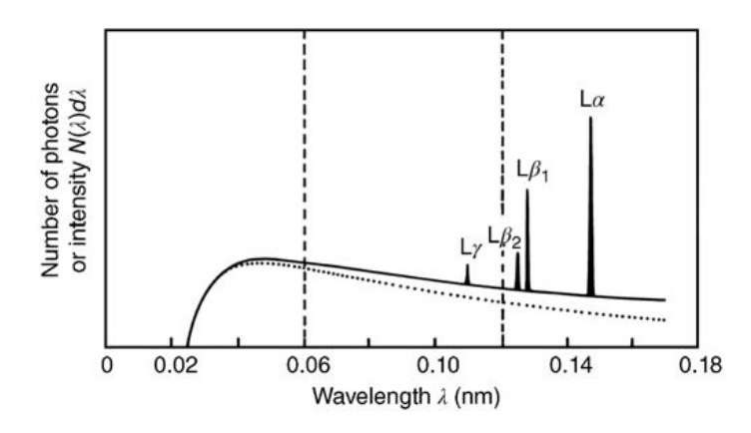


Figure 3.4: Spectrum represented in wavelength dispersive mode.[3]

The created electrons are filtered by the exit window of the tube. The distribution of the intensity can be approximated by [3]:

$$N(E)\Delta E \approx kIZ(\frac{E_0}{E} - 1)\Delta E$$
 (3.1)

Where  $N(E)\Delta E$  is the number of photons in the energy range from E to  $E + \Delta E$ , I is the tube current, k is a constant and Z is the mean atomic number [3]. The intensity of the continuous spectrum depends linearly on the tube current and the applied voltage.

#### 3.3 Characteristic Radiation

The characteristic radiation, or often called line spectrum, is created due to an ejection of an electron from its bound state with a nucleus caused by photon or electron that exceeds the binding energy of this particular bound electron. This vacancy is an instable state, that is filled by an outer bound electron. The energy difference between the previous, outer, state and the subsequent, inner, state equals the energy of the photon that is emitted[3]:

$$E_{photon} = E_{previous} - E_{subsequent} \tag{3.2}$$

In the anode material of the X-ray tube, the excitation is mainly caused by electrons and mainly by primary X-ray photons in the sample material. The binding energies of the electrons in bound states are characteristic for a specific element, which allows one to distinguish between different elements. Figure 3.5 shows three principal series, the K, L and M series. The letter indicates the shell in which the vacancy is located. Each series consists of several individual peaks, which are, in the Siegbahn notation, ordered from the most intense to the least intense peak and labelled with greek letters in alphabetical order. A further index differentiates the peaks using arabic numbers. Another way to

name the electron transition is to use the notation by the International Union of Pure and Applied Chemistry or IUPAC for short. Both notations are shown in figure 3.6.

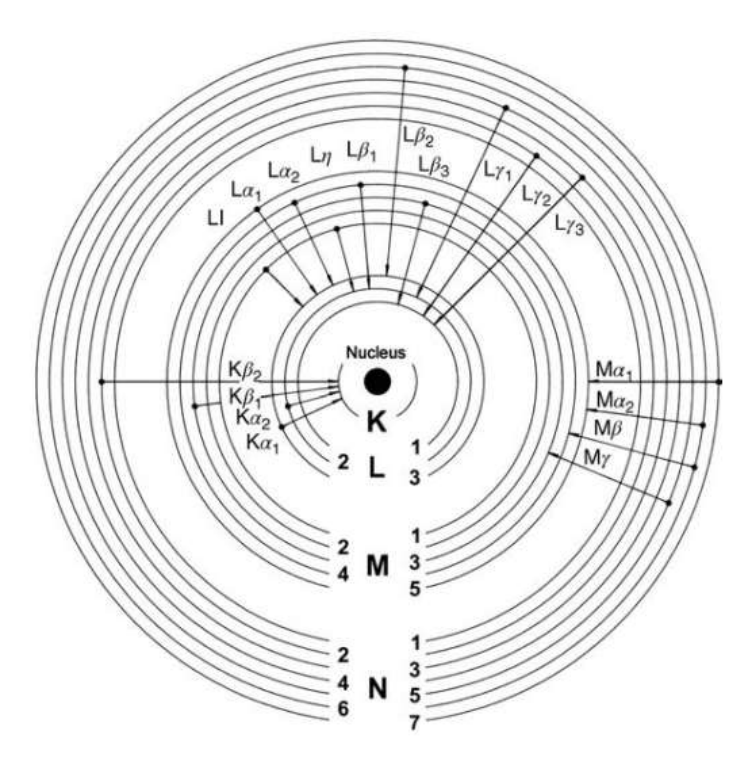


Figure 3.5: Possible electron transitions in a heavy atom [3]

Siegbahn	<b>IUPAC</b>	Siegbahn	<b>IUPAC</b>	Siegbahn	<b>IUPAC</b>	Siegbahn	IUPAC
$K\alpha_1$	$K-L_3$	$L\alpha_1$	$L_3-M_5$	$L_{\gamma_1}$	L2-N4	$M\alpha_1$	$M_5-N_7$
$K\alpha_2$	$K-L_2$	$L\alpha_2$	$L_3-M_4$	$L_{\gamma_2}$	$L_1-N_2$	$M\alpha_2$	$M_5-N_6$
$K\beta_1$	$K-M_3$	$L\beta_1$	$L_2-M_4$	$L_{\gamma_3}$	$L_1-N_3$	$M\beta$	$M_4-N_6$
$K\beta_2^{\rm I}$	$K-N_3$	$L\beta_2$	L3-N5	$L_{\gamma_4}$	$L_1-O_3$	$M\gamma$	$M_3-N_5$
$K\beta_2^{\text{II}}$	$K-N_2$	$L\beta_3$	$L_1-M_3$	$L_{\gamma_4'}$	$L_1-O_2$	$M\zeta$	$M_{4,5}-N_{2,3}$
$K\beta_3$	$K-M_2$	$L\beta_4$	$L_1-M_2$	$L_{\gamma_5}$	$L_2-N_1$		
$K\beta_4^{I}$	$K-N_5$	$L\beta_5$	L3-O4,5	$L\gamma_6$	L2-O4		
$K\beta_4^{II}$	$K-N_4$	$L\beta_6$	$L_3-N_1$	$L\gamma_8$	$L_2-O_1$		
$K\beta_{4x}$	$K-N_4$	$L\beta_7$	L3-O1	$L_{\gamma_8}$	L2-N6,7		
$K\beta_5^{\rm I}$	$K-M_5$	$L\beta_8$	$L_3-N_{6,7}$	$L_{\eta}$	$L_2-M_1$		
$K\beta_5^{II}$	$K-M_4$	$L\beta_9$	$L_1-M_5$	Ll	$L_3-M_1$		
		$L\beta_{10}$	$L_1-M_4$	Ls	$L_3-M_3$		
		$L\beta_{15}$	L3-N4	Lt	$L_3-M_2$		
		$L\beta_{17}$	$L_2-M_3$	Lu	L <sub>3</sub> -N <sub>6,7</sub>		
				Lv	$L_2-N_{6,7}$		

Figure 3.6: Comparision between the Siegbahn and IUPAC notation[3]

Not all transitions between shells are allowed, however, and the most probable transitions are the so-called dipole transitions. The selection rules for the dipole are given by [6]:

$$\Delta l = +/-1; \Delta m = 0, +/-1 \tag{3.3}$$

These rules are based on the conservation of angular momentum. [6]

Following the ejection of an inner electron and the subsequent occupation of this vacancy by an outer electron, a photon of characteristic energy is emitted, which causes one of two different processes: the emission of the X-ray photon or the Auger-Meitner effect (also often called Auger effect). If the photon excites another outer electron within the same atom, this electron is ejected from the shell and is called an Auger electron. The other process is the direct emission of the photon, which is the basis for X-ray fluorescence, or XRF. The second process dominates for heavier elements. The trajectory of an Auger electron can easily be altered using magnets, leaving only the fluorescence photons to be detected. The relationship between the creation of Auger electrons and X-ray photons can be approximated with the fluorescence yield  $\omega_i$ , which is displayed in figure 3.7[3].

$$\omega_i = \frac{Z^4}{A + Z^4} \tag{3.4}$$

The constant A has different values for different series, for the K-series A roughly equals  $9*10^5$  and for the L-series  $7*10^7$ . After the absorption of the initial photon, the sum of the individual probabilities for the generation of an X-ray photon or an Auger-Meitner electron is 1:  $\omega_i + a_i = 1$ , where  $a_i$  describes the yield for Auger-Meitner electrons.

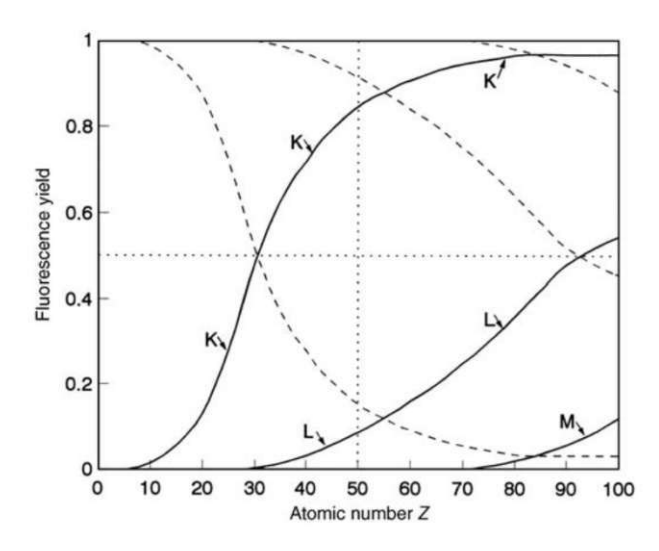


Figure 3.7: The fluorescence yield for different series as a function of the atomic number. Fluorescence yield(——) and Auger electron yield (- - - -)[3]

The intensity for a characteristic line can be described with the empiric formula [3]:

$$N_{line}(E_{ij}) = kIg_{ij}\omega_i * E_{min}^m (\frac{E_0}{E_{min}} - 1)^m$$
(3.5)

Where  $N_{line}(E_{ij})$  is the number of photons for the energy  $E_{ij}$ , k is a constant, I is the electron current,  $g_{ij}$  is the emission rate of the line i in series j and  $\omega$  is the fluorescence yield.  $E_0$  is the exciting potential of the X-ray tube,  $E_{min}$  is the critical excitation energy for the spectral series, and m is an exponent, with a value usually below 2. This suggests that the intensity is linear in the electron current and changes non-linearly in the accelerating voltage  $U_0$  due to the relation  $E_0 = eU_0$ , where e is the elemental charge. [3]

#### 3.4 Interaction between Matter and X-rays

When a beam of X-rays passes through a medium its intensity will decrease because of different interaction effects. This is described by the Lambert-Beer law that can be written as [3]:

$$N(d) = N_0 * exp[-\frac{\mu}{\rho}\rho d] \tag{3.6}$$

Where  $N_0$  is the initial number of photons hitting the surface of the material, d is the thickness of the material,  $\rho$  is the density of the material, N(d) is the number of photons at the depth d and  $\mu$  is the linear absorption coefficient [3].

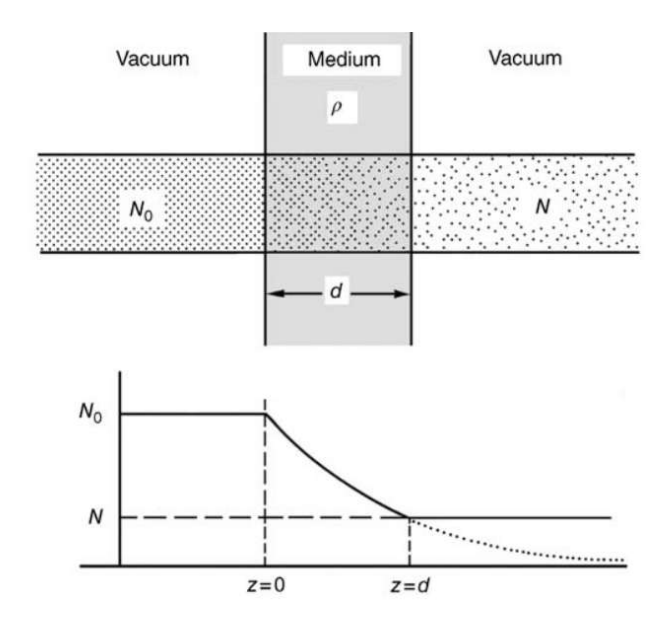


Figure 3.8: Attenuation of an X-ray beam in a medium.[3]

The term  $\frac{\mu}{\rho}$  is called the mass attenuation coefficient. For mixed materials, individual components can be added to obtain the total mass coefficient, with  $c_i$  being the mass fraction for different elements:  $(\frac{\mu}{\rho})_{total} = \sum c_i(\frac{\mu}{\rho})_i$  [3]. The specific values for the mass coefficients are dependent on the energy, and the element can usually be taken from tables.

The attenuation is caused by three interactions: the photoelectric absorption, X-ray scattering and pair production. For lower energies, the photoelectric absorption is most likely up to roughly 100keV, the X-ray scattering dominates up to 1MeV, after which pair production is possible and takes over as main interaction. The energy range of pair production lays way above the energies that are used for X-rays and will not be explained in detail any further.

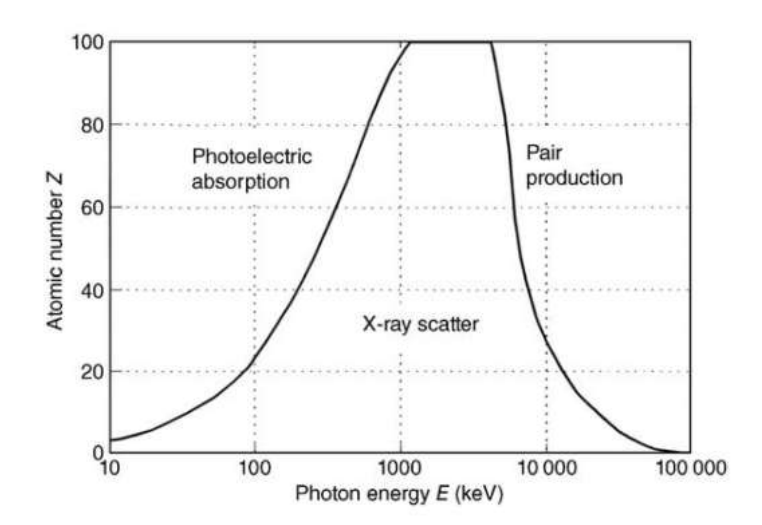


Figure 3.9: The three effects causing attenuation in matter. Each effect dominates in a specific energy range and depends on the atomic number.[3]

#### 3.5 Photoelectric Absorption

For energies below 100keV, the absorption due to the photoelectric effect is the most probable effect. A photon is absorbed by a bound electron, which causes this electron to be ejected from the atom whose kinetic energy is given by the difference between the energy of the photon and the binding energy of the electron. As described in section 3.1, this vacancy is immediately filled with an outer bound electron, which leads to the emission of an X-ray fluorescence photon. The specific mass-absorption coefficient  $(\frac{\tau}{a})$ can be used to evaluate the photoelectric absorption. It can be approximated by the Bragg-Pierce law[3]:

$$(\frac{\tau}{\rho})_j = k_j(\frac{Z^3}{E^{\frac{8}{3}}})$$
 (3.7)

In figure 3.10 below, the mass-absorption coefficient for molybdenum is plotted against the photon energy in a double-logarithmic plot.

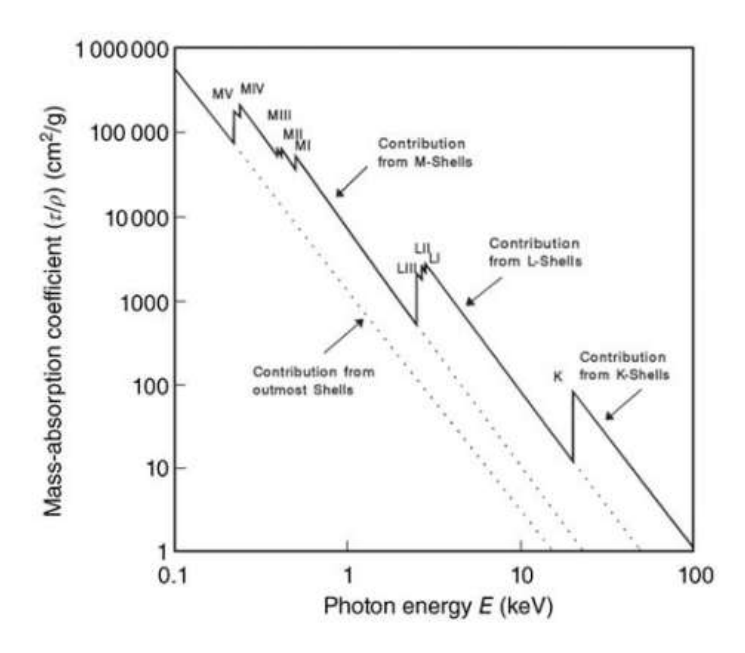


Figure 3.10: The photoelectric mass absorption coefficient plotted against the photon energy.[3]

In the figure above, the mass absorption coefficient decreases with a negative slope of  $-\frac{8}{3}$  with increasing energy. This behaviour persists until the photon energy increases so far that electrons of another shell can be ejected, thus, increasing the mass-absorption coefficient again[3].

### 3.6 X-ray Scattering

The scattering of X-ray represents a relatively small component of the absorption when compared to the photoelectric effect. One characteristic of the scattering is that the atoms are not ionized, only deflected from their position. It can be distinguished between elastic and inelastic scattering. Elastic scattering happens when the incident wave, the photon, causes the electrons of the atom to oscillate in the frequency of the initial wave. This atom becomes a dipole and emit a spherical wave with the frequency of the original photon [7]. This is called Rayleigh scattering and it is always a coherent collision, which indicates a fixed relationship between the phases of the incoming and outgoing photon[3]. Furthermore, all electrons contribute to Rayleigh scattering, therefore, the coherent scattering intensity increases directly proportional to the atomic number [8]. The intensity of the elastically scattered radiation depends on the scatter angle  $\Psi$  with the behaviour [8]:

$$I = \frac{I_0}{R^2} (1 + \cos^2(\Psi)) \tag{3.8}$$

Where  $I_0$  is the intensity of the primary non-polarized radiation on a sphere with the diameter called R. This intensity is minimal for  $\Psi = 90$  [8]. Hence, a 90 geometry is a common experimental setup for XRF spectrometers.

Compton scattering is the process that describes the inelastic scattering, where the photon collides with a free electron or an electron that is loosely bound to an atom. The ratio of the energy of the reflected photon E' and the energy of the incident photon Ecan be described by using the formula[3]:

$$\frac{E'}{E} = [1 + (1 - \cos(\Psi))\frac{E}{E_0}]^{-1}$$
(3.9)

Where  $E_0$  is the rest energy of the electron and  $\Psi$  is the angle of deflection. Using this relation, it is possible to calculate the scatter angle  $\Psi$  with the energy of the incoming and scattered photon. It is also possible to describe the change in energy as a change of the wavelength  $d\lambda[3]$ :

$$d\lambda = \lambda_C (1 - \cos(\Psi)) \tag{3.10}$$

 $\lambda_C = \frac{hc}{E_0}$  is the Compton wavelength which has a value of 2.426pm for electrons[3]. Since only the outer, loosely bound electrons contribute to the incoherent scattering, its intensity is practically independent of the atomic number. The ratio of the intensities of the coherent and incoherent scattering can be used to estimate the average atomic number of the sample.[8]

An example of a spectrum with the visible Compton and Rayleigh peak can be seen below in Figure 3.11.

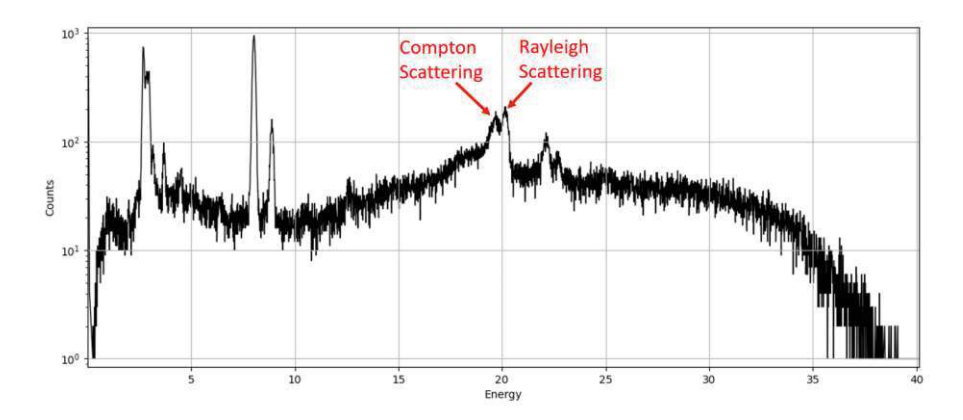


Figure 3.11: A spectrum of a Cu sample excited using a Rh tube. The respective Rh scatter peaks are indicated in red.

## 3.7 Measuring the Fluorescence Intensity

Theoretically, if all fundamental parameters that effect the fluorescence intensity of a specific element are known, then the fluorescence intensity for a line can be calculated. A general case of the contributions to the intensity of a fluorescence signal is outlined in figure 3.12 and further elaborated upon. In this example, the signal is coming from an infinitesimal layer located in a given depth of the sample, after being excited by a source. An integral over the whole thickness of the sample and the complete energy range results in the intensity for a specific line. For thick samples it is crucial to consider the inter element absorption, where the fluorescence photons are partly absorbed by other elements before exiting the sample. [9].

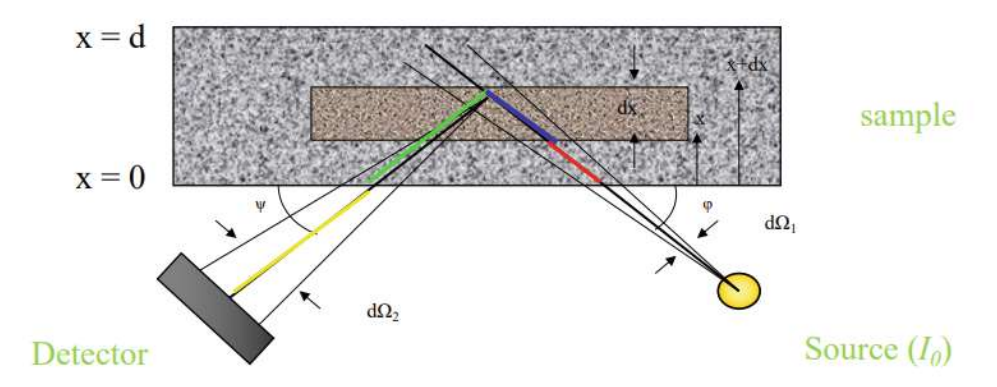


Figure 3.12: Illustration of the path the X-ray photon takes from the source (X-ray tube) via the sample to the detector. Each contribution is shown in different colour[9].

$$I(E_{K\alpha}^{i}) = \int_{E=E_{abs}^{i}}^{E=E_{max}} \int_{x=0}^{x=d} \underbrace{I_{0}(E)}_{I} * \underbrace{G_{1}}_{II} * \underbrace{\frac{\rho}{\sin(\phi)} \frac{\tau_{K}^{i}(E)}{\rho}}_{III} * \underbrace{\frac{\omega_{K}^{i} * p_{\alpha}^{i} * \underbrace{c^{i}}_{V} * \underbrace{V^{i}(E)}_{VI} * \underbrace{e^{-(\frac{\mu(E)}{\rho * \sin(\phi)} + \frac{\mu(E_{K\alpha}^{i})}{\rho * \sin(\psi)}) * \rho * x}}_{VII} * \underbrace{G_{2}}_{VIII} * \underbrace{f(E_{K\alpha}^{i})}_{IX} * \underbrace{\epsilon(E_{K\alpha}^{i})}_{X} dx dE$$

$$(3.11)$$

I = the intensity generated by the X - ray tube

II = the geometry factor, caused by the shape and distance of thedetector, and optionally a collimator

III = photoelectric absorption within dx under consideration of theentering angle

IV = fluorescence yield and probability of emission for a specific line

V = concentration of element i

VI = interelement absorption

VII = absorbtion of the entering radiation and exiting rediation

VIII = geometry factor of the detector

IX = attenuation by air absorption on path between sample and detector

 $X = detector\ efficiency\ including$ 

all absorbers Be contact dead layer and thickness of the detector

[9]

### 3.8 Evaluation of Spectra

There are multiple approaches on how to evaluate a captured spectrum. In the most convenient case, the characteristic lines in the spectrum are far away from each other, thus, allowing the user to simply set a region of interest (ROI) around the peak. The trapeze-shaped background is then subtracted from the gross counts in the region, resulting in the net count for the selected line. Figure 3.13 and 3.14 show one case in which a ROI yields results sufficient for many applications.

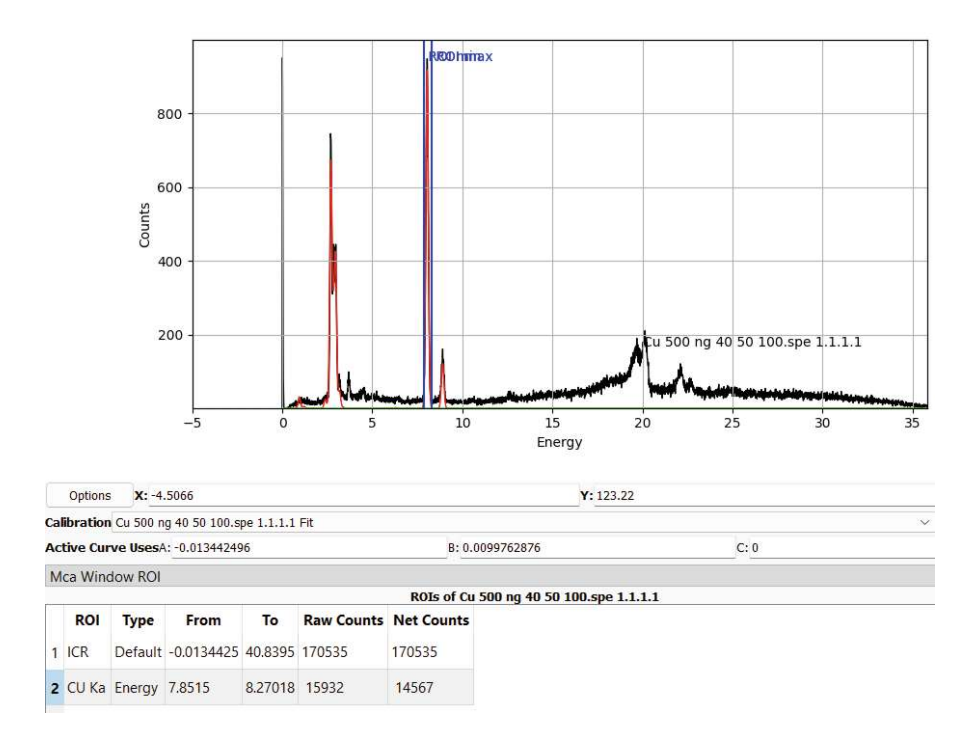


**Figure 3.13:** One example in PyMCA [10] where Cu K $\alpha$  is of interest. The peak is only surrounded by a smooth background; hence, the spectrum does not need to be deconvoluted. The counts are displayed at the bottom.

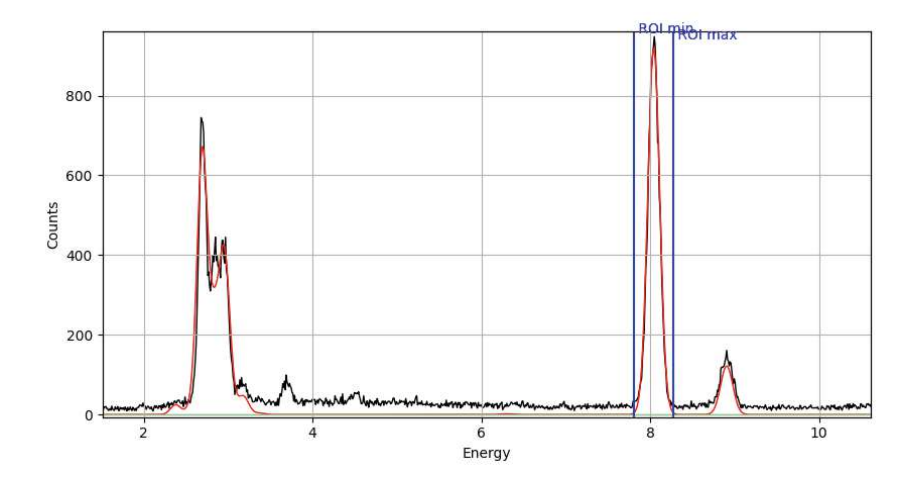


Figure 3.14: A close-up of the ROI.

If, however, two or multiple line are close in the spectrum or even overlap each other the peaks must be deconvoluted. Otherwise, one region might contain counts of a neighbouring region. This is a common issue for metals, where the  $K\beta$  line overlaps with the  $K\alpha$  line of the elements with the next higher atomic number. A number of programs have been developed to compute this devoncolution namely:

- AXIL, by IAEA [11]
- PyMCA, by ESRF [10]
- jpeakfit, developed in-house [12] [13]

#### 3.9 Limit of Detection

One way to determine the smallest quantity of a specific element that can be detected is to use the lower limit of detection, or LLD, within a level of confidence (i.e.  $2\sigma$ ). The LLD is defined as:

$$LLD = \frac{3\sqrt{N_{NB}}}{N_{sample}} w_{sample} \tag{3.12}$$

Where  $N_{NB}$  is the number of background counts,  $N_{sample}$  is the number of counts in the peak and  $w_{sample}$  is the concentration of the element in the sample [8].

#### 3.10 Geometric Optic

The propagation of an electromagnetic wave and interaction with other waves are, in principle, given by the Maxwell equation. However, a classical description may give adequate insight in the behaviour of light when the contribution of interference effects can be considered negligible. This approach proves useful when the considered distances are far larger than the coherence length in which stable interference patterns can occur[14]. In this thesis, this formalism has been used to describe the optics necessary for safety features, specifically the light barrier in section 7.1.

When a beam of light, or a plane wave reaches an interface between two media with two different optical densities, the phenomena refraction and reflection may be observed. In case of transitioning from an optically thinner to an optically thicker medium, the incoming beam of light will be directed away from the interface [14]. This is illustrated below in figure 3.15.

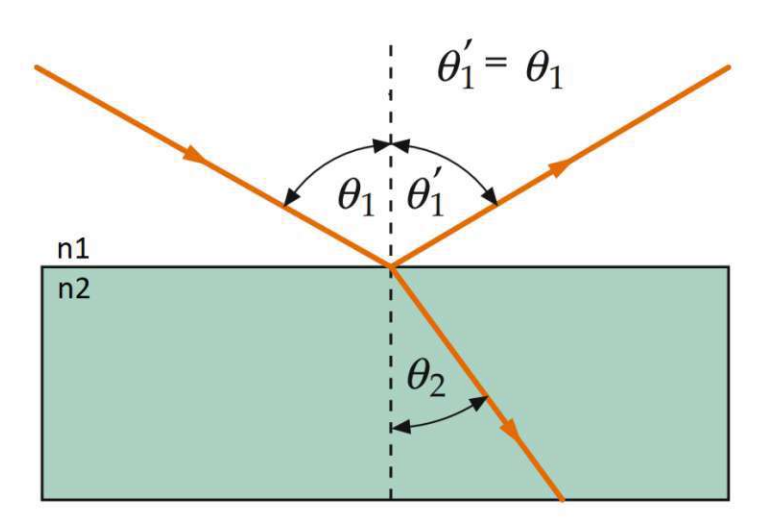


Figure 3.15: One example of refraction for the case  $n_2 > n_1[6]$  (edited)

This is described by the law of refraction by Snellius:

$$\frac{\sin(\theta_1)}{\sin(\theta_2)} = \frac{n_2}{n_1} \tag{3.13}$$

[14]

#### 3.11 Euler Method

One way to solve differential equations a numerical approach. An advantage of solving differential equation numerically is that the initial or boundary conditions are required to solve the equation, hence, those conditions do not need to be solved explicitly. There are multiple methods that can be implemented to solve a differential equation [15]. For this thesis, the Euler method was used to determine the shape of the aforementioned focusing lens in section 7.1.1.

To find a solution for the function y(x), an explicit form for y'(x), which is often written as y'(x) = f(x, y) in literature, is a requirement. This function f(x, y) can therefore be used to determine a new step for the discrete function  $y_k(x_k)$ . The general formula for calculating the following value of  $y_k(x)$  is  $y_{k+1} = y_k + f(x_k, y_k) * \Delta x$  where  $\Delta x$  is the difference between  $x_{k+1} - x_k$  [15].

#### 3.12 Machine Learning

During the course of this thesis, a visual AI was used to interpret the camera input for determining the distance between the sample and the measuring head (see section 6). This section gives a short summary on the types of AI and evaluation metrics.

Machine learning is a term referring to algorithms that allow a computer to learn from the data provided. Generally, a machine learning algorithm falls in one of two categories: supervised learning and unsupervised learning. Since only supervised machine learning was used in this thesis, only this category will be explained further.

In supervised learning, the algorithm is provided with some training data that already maps the input to the desired output. The initial mapping of the training data has to be done manually or by using a different, already existing, AI. This process is called labelling.[16] Supervised machine learning can further be divided into two sub-categories: classification or regression. Classification is used when the output falls into a set of predetermined classes, in other words, the labels are discrete. In the case of regression, the labels are continuous.[17] Classification was used for this thesis.

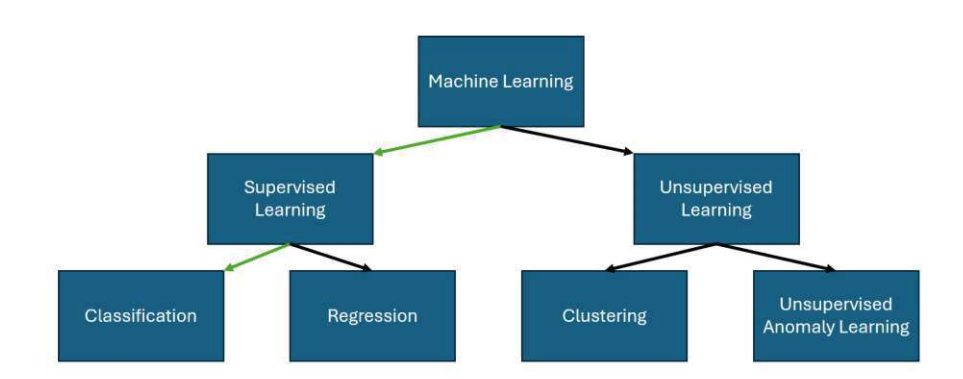


Figure 3.16: A graphical overview of the machine learning algorithms. The green arrows highlight the categories, which are discussed in greater detail in this section.

When training the algorithm, the test data is split into two categories: the training set and the validation set. The training set is used to adjust the mapping of inputs to outputs in the algorithm and the validation set is used to verify how good this mapping is. If the discrepancy is too significant, the process is repeated, and the mapping will be changed again. It is important to mention that the validation set should not contain data identical to the training set. [17]

A few important metrics for evaluation are called precision and recall. Precision measures what percentage of the output, labelled by the algorithm, was also labelled in the validation data set. Recall measures what percentage of the validation data set was also correctly labelled by the algorithm. The algorithm tries to maximize this value during the training process. The loss measures the difference between the prediction from the actual labels. The algorithm tries to minimize this value during the training process. [17]

#### 3.13 Semiconductors

In XRF most detectors of interest are based on semiconductors in which the atoms are orientated in a crystalline structure. The electrons bound to the nuclei reside in discrete energy levels which are grouped in multiple band that are separated by the band gap. The lower band is called the valance band, and it is occupied by electrons that can be excited and thus transferred to the higher energy band, the conduction band. One of the most commonly implemented semiconductor materials is silicon. Pure silicon, however, is of little use when considering detector materials and 'impurities' are therefore purposefully added. These elements usually have either one additional electron or a vacancy, when compared to the silicon atom which has four valance electrons. This implies that either elements from the fifth (donor atom) or the third main group (acceptor atom) are added. When impurities, as mentioned above, are present, the semiconductor is referred to as 'doped'. This is illustrated in figure 3.17[18].

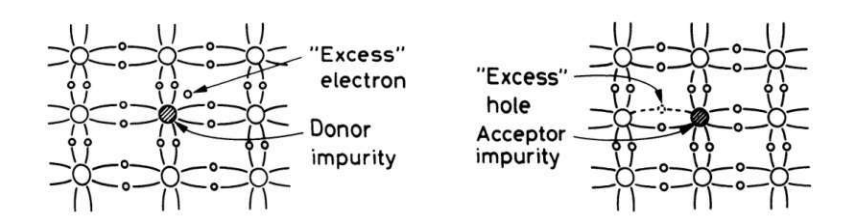


Figure 3.17: Introduction of a donor and acceptor.[18]

When doping the semiconductor correctly, one important feature of this technology, the p-n junction, can be implemented. This region of the semiconductor is created by bringing an n-doped material (donor) together with a p-doped material (acceptor) [18]. In order to fill the vacancy, the electrons of the n-doped material close to the p-doped material will diffuse into the p-doped region. This causes the n-doped region close to the interface to be positively charged and the p-doped region to be negatively charged. Due to the difference in charge an electric field is created, that accelerates free charge carriers out of this region. A schematic illustration can be seen below in figure 3.18.

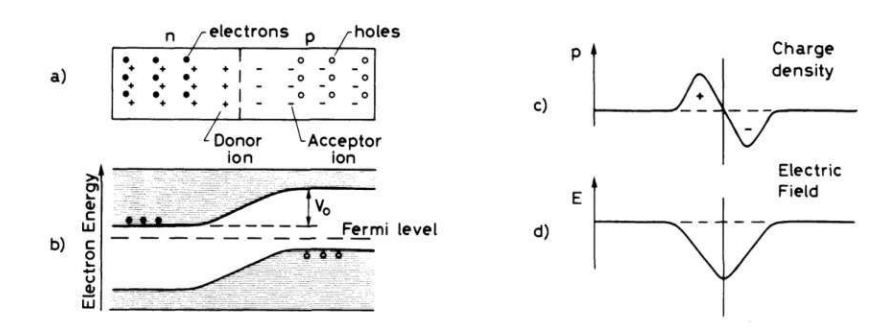


Figure 3.18: a) Diagram of a p-n junction, b) Electron energy levels at junction, c) Charge distribution, d) Electric field[18]

The extent of this region, the junction, can be altered by applying a so-called bias voltage to the detector. A negative potential on the p-doped side, attracting the holes away from the junction, while a positive potential on the n-doped side will attract the electrons in a similar matter. This increases the region affected by the electric field also-called the depletion zone [18]. The depth of this zone increases with the applied bias voltage until the geometrical limitations of the detector are reached. This voltage is named full depletion voltage.

#### 3.14 Silicon Drift Detectors

In modern detector technology, it can be distinguished between PIN detectors and silicon drift detectors (SDD). Below in figure 3.19 the basic layout including the typical diffusions are sketched out.

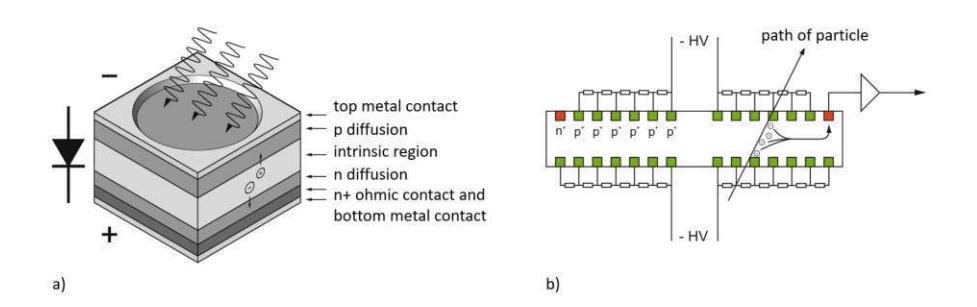


Figure 3.19: An illustration showing the basic layouts of a) a PIN diode and b) a silicon drift detector[19](edited)

The common choice for XRF is an SDD which will be explained in detail this section.

The positions of the n-doped and the p-doped region affect the direction in which the charge carriers are depleted. One example is called the sideways depletion, which can be achieved by implanting two p-doped regions opposite of each other and an isolated n-doped region on one side. By applying a negative potential on the p-doped, the cathode, region a depletion zone will emerge around each p-doped area. When lowering this voltage further, the depletion zones will touch each other. In this case the electric field decreases linearly towards the middle of the detector volume, which in turn causes a parabolic potential with its minimum in the middle[19].

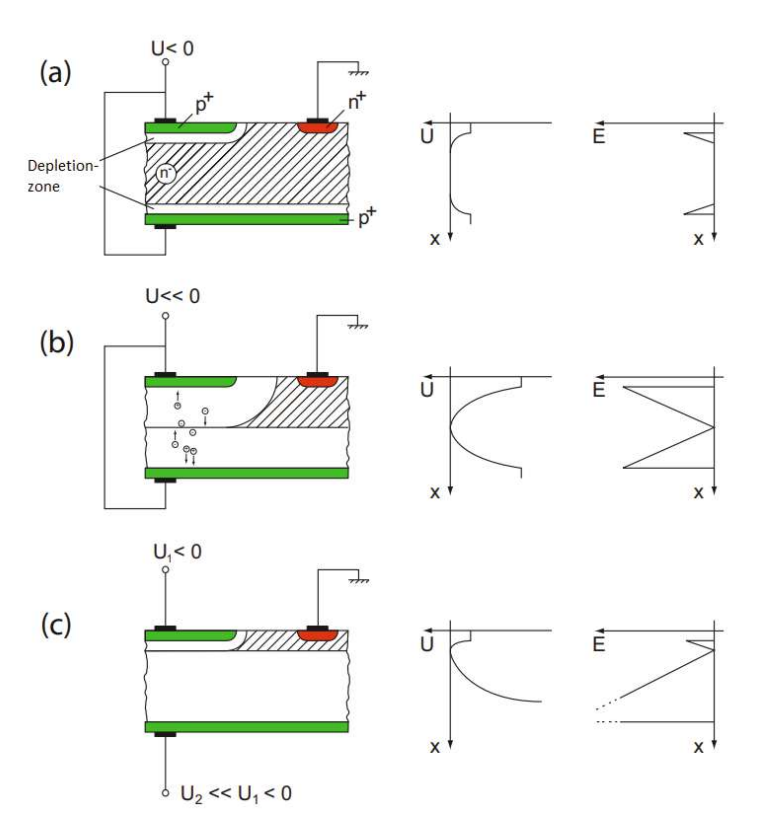


Figure 3.20: Principle of sideways depletion a) U<0, detector not fully depleted, b) U«0, depletion zones touch each other, c) displacement of potential minimum, due to different applied voltages [19] (edited)

The positive charge carriers are collected at the p-doped region and the negative charge carriers are repelled towards the middle between the p-doped regions, in other words the electrons will move to the minimum of the potential parabola. In figure 3.20, the affect of an applied voltage is shown and the corresponding potential on the right side.

This principle is usually expanded upon by adding multiple opposing pairs of cathodes. The negative voltage is distributed in equidistant steps and reaches 0V on the cathode next to the anode as can be seen in figure 3.21[19].

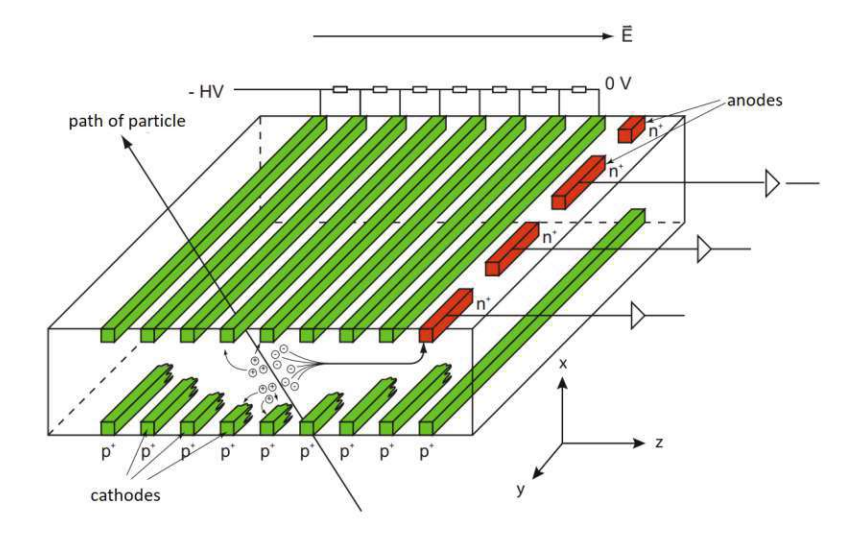


Figure 3.21: The introduction of a sideways linear electric field causes a drift of the electrons towards the anode. [19] (edited)

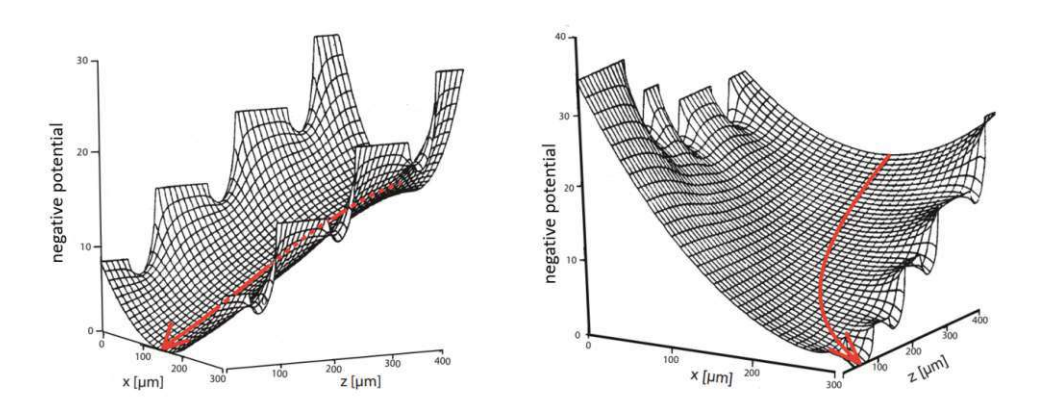


Figure 3.22: The negative charge carriers follow the minima of the parabolas until they reach the anode. [19] (edited)

Using this setup, a linear electric field is superposed on the parabolas between each pair of cathodes, resulting in drift path for the charge carriers. The resulting potential is shown in figure 3.22[19]. The charges are then collected at the anode and the resulting

signal is processed by the detector electronics.

# 4 Detector and X-ray Tube

This section highlights the properties of the two main components of the system, the silicon drift detector and the X-ray tube.

## 4.1 X-ray Tube-AMPTEK Mini X

The setup utilises low power a Mini-X X-ray tube by the company AMPTEK as excitation source. As mentioned in section 3.1, it is a transmission X-ray tube, which enables the user to get the tube closer to the sample, when compared with a side window X-ray tube.



Figure 4.1: The detector including the detector electronics [20]

Rh
$0.75 \mu \mathrm{m} \; (+/ ext{-} \; 0.1 \mu \mathrm{m})$
10 kV to 50 kV
5 μA to 200 μA
$1~\mathrm{Sv/h}$ @ 30 cm on axis, 50 kV and 80 $\mu\mathrm{A}$
$<10^6$ counts per second/ $mm^2$ on the axis
$4\mathrm{W}$ max @ 100% duty cycle
Be, window at ground
127 μm
approximately 2 mm
120°
Air cooled

A set of X-ray collimators can be inserted into the tip of the tube. In this setup, a

brass collimator with an opening of 1mm diameter with a 1mm thick aluminium cap is used to avoid backscatter of brass into the detector.

### 4.2 Detector-KETEK Vitus H150



Figure 4.2: The detector including the detector electronics [23]

Energy resolution	$\leq 136 \text{ eV}$
Peak to background	> 15,000
Peak to tail	>2,000
Optimal peaking time at max. cooling	1µs
Absorption depth Si	$450 \mu m$
Peak shift stability up to 100 kcps	<1 eV
max. input count rate	2,000  kcps
Window Be DuraCoat Plus	$25 \mu \mathrm{m}$
Cooling performance	$\Delta T > 90 \mathrm{K}$
On-chip collimator	multilayer

# The Setup

The setup can be broken down into a few main components: the X-ray tube, the detector, the frame and the software. As an X-ray source a 4 Watt Mini-X X-ray tube [20] by the company AMPTEK [21] was used and as a detector an AXAS-D SSD detector [23] by the company KETEK [22] was used. Details to each can be found in the according subsections. The frame, which has been mostly redesigned during this thesis, was based on the diploma theses of Alexander Utz[1] and Peter Allinger[2]. Most of the fabricated components are made from alumiunum or 3D printed PLA plastic, depending on the required strength, complexity of the design or whether electrical insulation is needed or not.

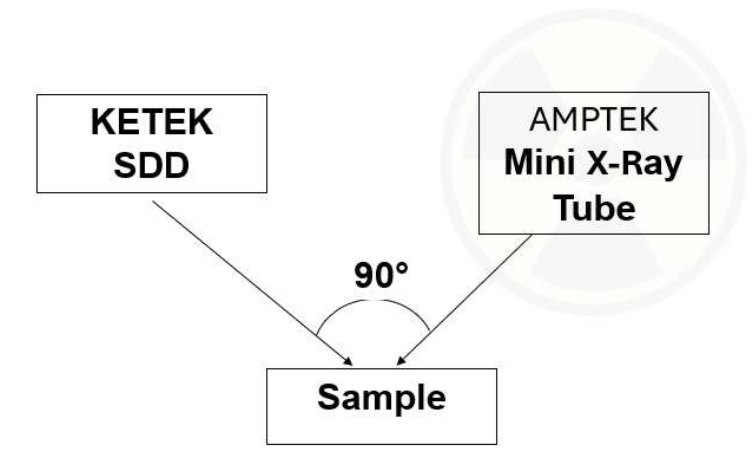


Figure 5.1: The basic geometry used to design the MAXI

Figure 5.1 displays the basic geometry used to construct the MAXI, especially the frame and the parts that are attached to the frame.

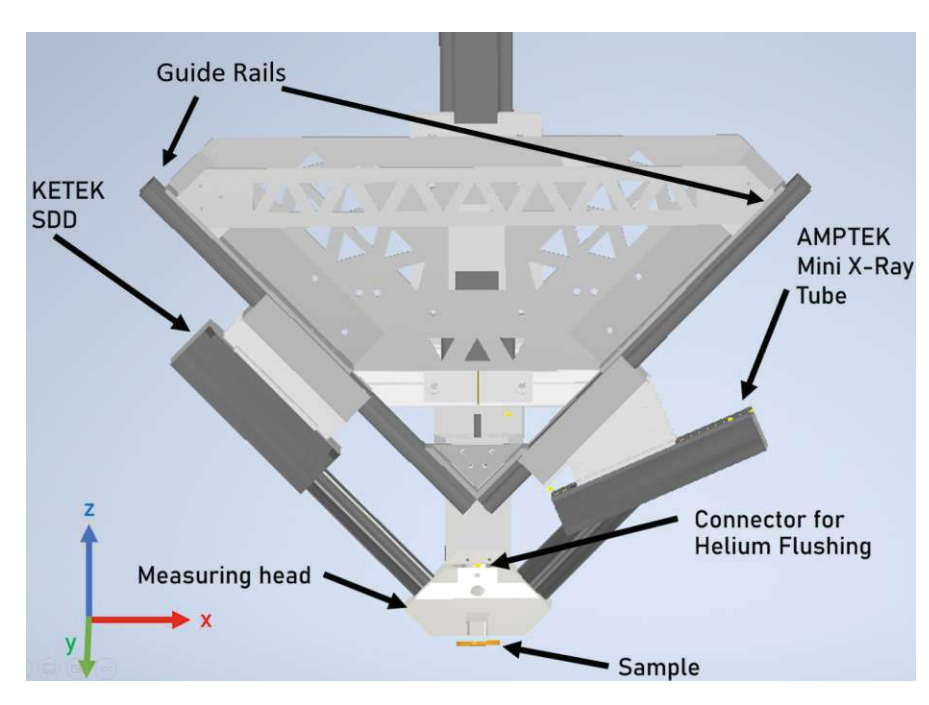


Figure 5.2: Rendering of the frame and the attached components of the MAXI in Autodesk Inventor

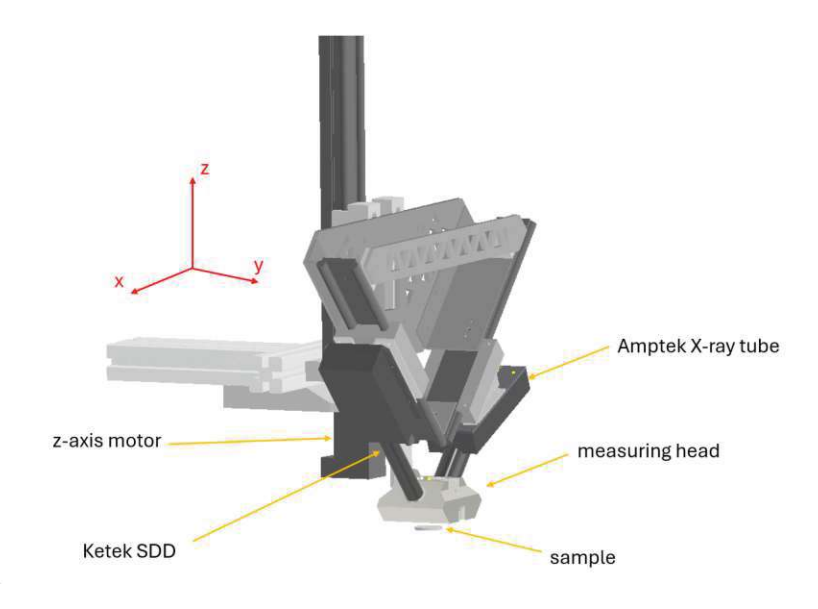


Figure 5.3: An assembly of the major components in Autodesk Inventor

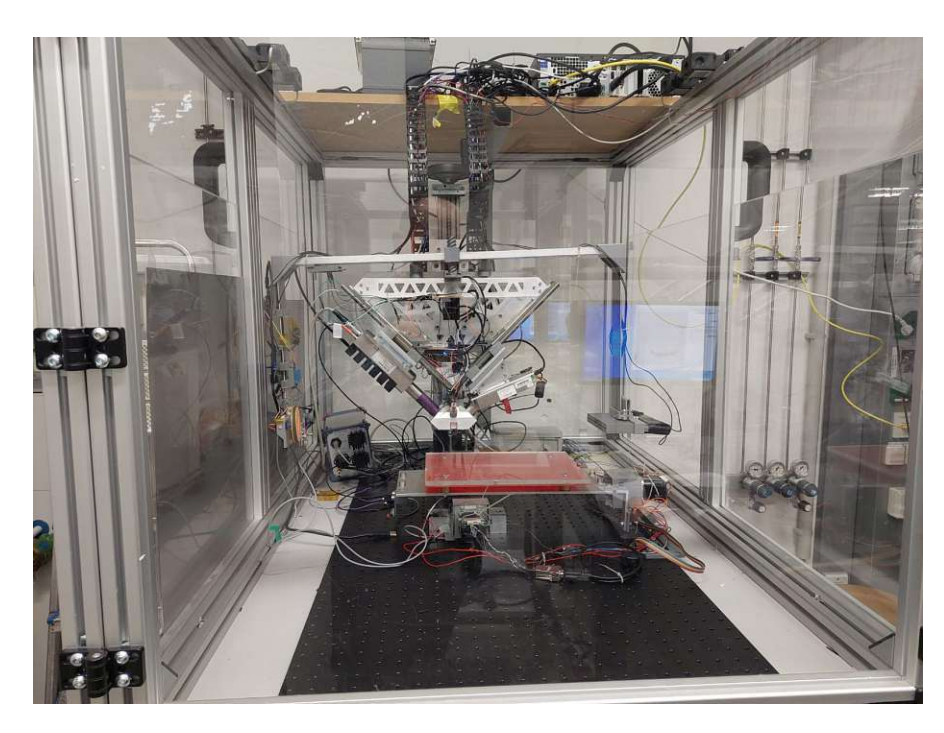


Figure 5.4: A picture of the setup in the lab. On top of the wooden board of the measuring cage, the 24V power supply, power sockets and the PC including a USB hub are placed. On top of the triangular frame, a rail is positioned, which holds the components for the light barrier (section 5.4 and section 7.1)

The frame is positioned above x-y table which can be moved using the X-Spect software. Both the frame and the table are mounted on a breadboard. One of the most important parts is the measuring head at the bottom of the frame (see illustration 5.3). It not only houses the tips of the tube and the detector, but also two laser pointers each directed 45° downwards. The beams of the laser pointer cross each other in the position that coincides with the position of the focal point of the X-ray tube when inserted. The rails, on which the X-ray tube and detector are positioned, allow for easy and safe exchange of the detector and the tube.

The frame, which can be seen in more detail in figure 5.2 can be moved up and down along the z-direction using the stepper motor (see figure 5.3). The requirements for the redesign of the frame were that the detector and X-ray tube had to be easily accessible and exchangeable. Furthermore, the weight should be kept as low as possible in order to not put strain on the motor for the z axis. The motor used is a PD2-C4118L1804-E-01 stepper motor by Nanotec [24]. Alternatively, the handle on the top of the MAXI can be used to move the frame up or down. The z motor, however, must be disconnected from the X-Spect software to adjust the height manually. A detailed explanation on how this motor is controlled follows in section 6.

#### 5.1 Detector Collimator

A new detector collimator has been designed and constructed using 3D printing. The hole is conically shaped, with a diameter of 3mm at the bottom and 11mm at the top. It has been printed using a transparent PLA plastic. The absence of pigments implies, that the plastic only contained the elements hydrogen, carbon and oxygen. Hydrogen does not emit fluorescence photons, and the other two elements pose a difficulty detecting, due to absorption and the low fluorescence yield. None of these elements are detected practically using this setup, thus serving as an adequate shielding from undesired X-ray photons, e.g. photons produced from within the measuring head. For this reason, a clean blank spectrum (see section 8.2) is achieved.

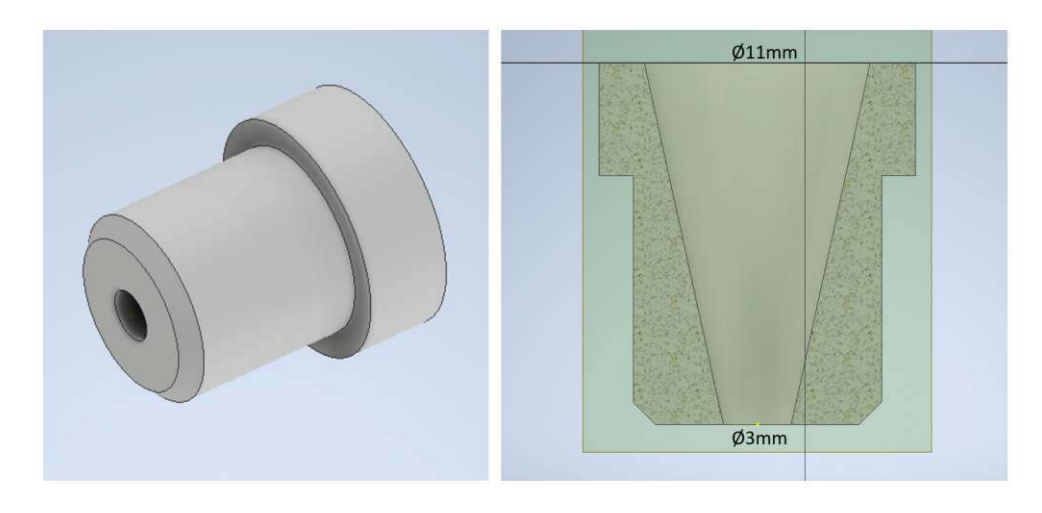


Figure 5.5: The design for the collimator in Autodesk Inventor.

#### 5.2 Adaptation to the Measuring Head

The measuring head, which was designed and constructed during a previous diploma thesis by Allinger [2], has been subject to changes. These changes are primarily limited to removing the externally attached LED lights and inserting internal SMD lights. This allows the user to illuminate the sample in a position where the measuring head is only a few millimeters away from the sample. The difference in the design can be seen in figure 5.6.

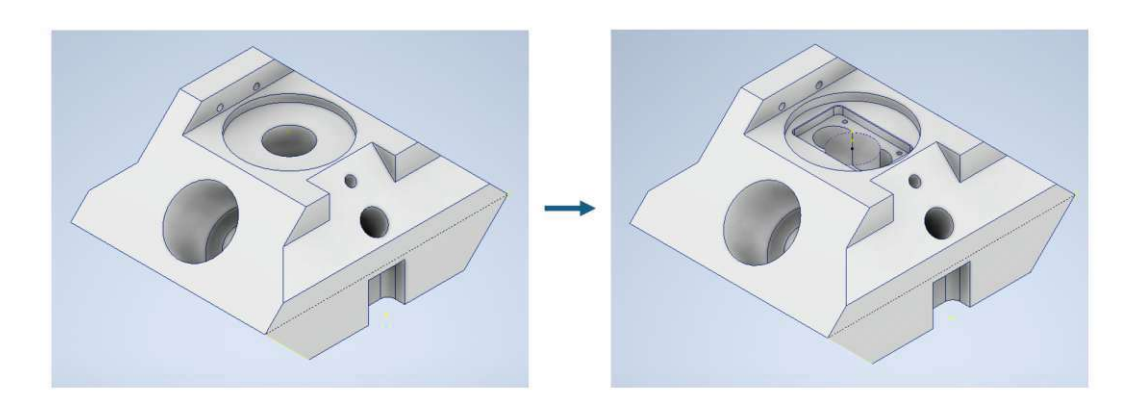


Figure 5.6: On the left: the original measuring head by Allinger [2]. On the right: the adapted measuring head which allows for internally mounted lighting.

To position the LEDs inside the measuring head a holder has been designed which houses a strip of 4 SMD LEDs. Two of these holders can be screwed in the top of the measuring head with enough space left to fit in the camera between the holders.

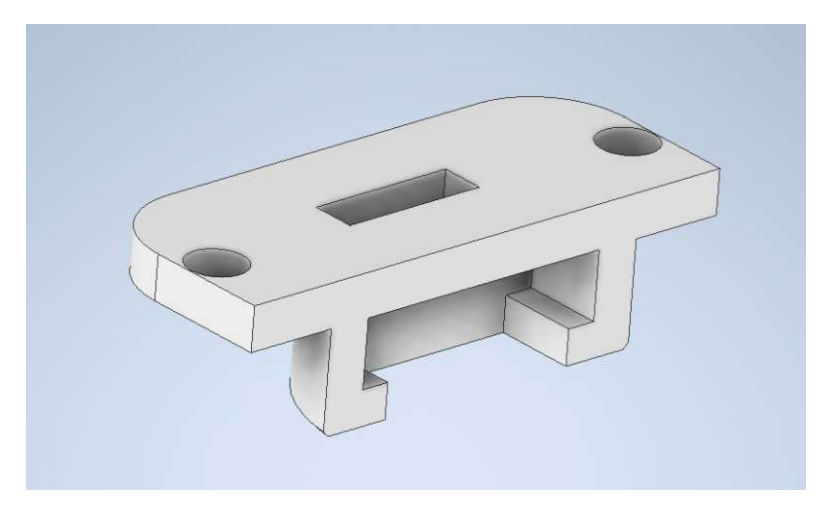


Figure 5.7: The holder for the SMD LEDs is 3D printed and screwed in the holes in the rectangular shaped insert of the measuring head.

### 5.3 Integration of Z Motor

The stepper motor, a PD2-C4118L1804-E-01 by Nanotec [24] responsible for movement perpendicular to the sample stage, has been mounted on the bottom of the rail behind the triangular aluminium frame.



Figure 5.8: A picture of the z motor.

The technical details are summarized in the table below.

Size	$42\mathrm{mm}$
Fieldbus	-
Holding Torque	$50 \mathrm{Ncm}$
Rated Current (RMS)	1.8A
Number of Digital Inputs	6
Type of Digital Inputs	24V, 5/24V switchable
Number of Analog Inputs	1
Type of Analog Inputs	$0.20 \mathrm{mA}/0$ - $10 \mathrm{V}$ switchable
Number of Digital Outputs	2
Type of Digital Output	open-drain $(max.24V/100mA)$
Encoders	integrated
Encoder Resolution	1024
Encoder Type	single-turn absolute
Weight	$0.5 \mathrm{kg}$
NEMA	17
Interface	USB
Operating Voltage	12VDC-48VDC
Peak Current (RMS)	3A
Length	74mm

In this setup, the motor is supplied with 24V. The motor can be configured and controlled using the software Plug&Drive Studio 1.[25]

The motor is connected to the thread next to the vertical rail.

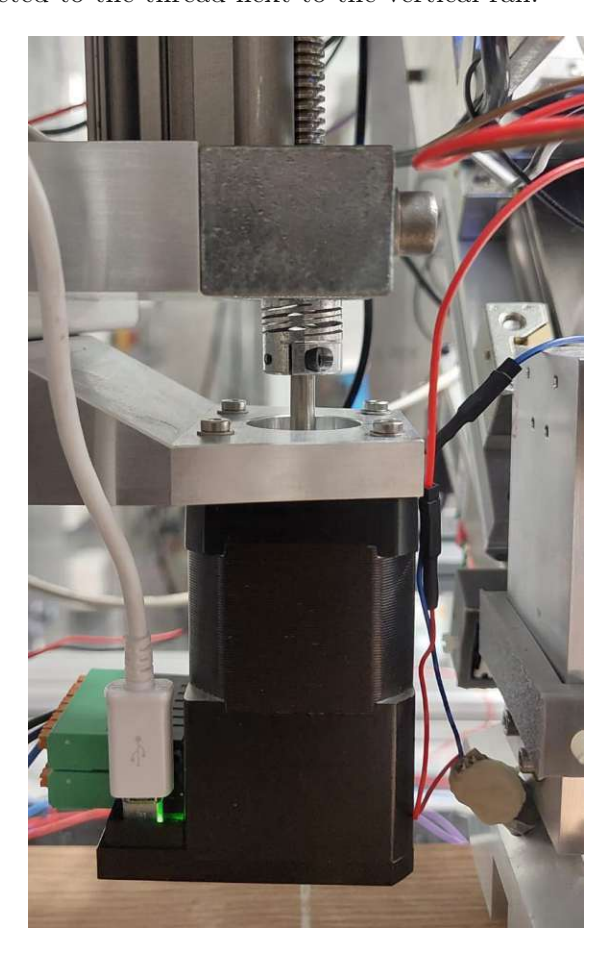


Figure 5.9: The mounting of the z motor and coupling connection to the thread.

Furthermore, below the handle, on the top end of the thread, a ball bearing has been positioned to distribute the weight of the frame and main components on the rails in the back. Without this component, the motor would have to bear the entire weight of the frame, and thus, possibly exceed the maximum holding torque of the stepper motor. Using the program Plug&Drive Studio, the position can be set by writing to the object, seen below in figure 5.10.

### 607Ah Target Position

This object specifies the target position in user-defined units for the Profile Position and Cyclic Synchronous

### **Object description**

Index 607A<sub>h</sub> Target Position Object name Object Code VARIABLE INTEGER32 Data type

Savable yes, category: application

Access read / write PDO mapping RX-PDO

Figure 5.10: The object responsible for setting the target position

## 5.4 Main Components of Light Barrier

One of the safety features, which are elaborated upon in more detail in section 7, is the light barrier. The main components of this feature will be explained in this section. Below in figure 5.11, the belt system for the movement of the laser diode is displayed. Figure 5.12 shows the holder for the focusing lens, which is located on the other side of the spectrometer.

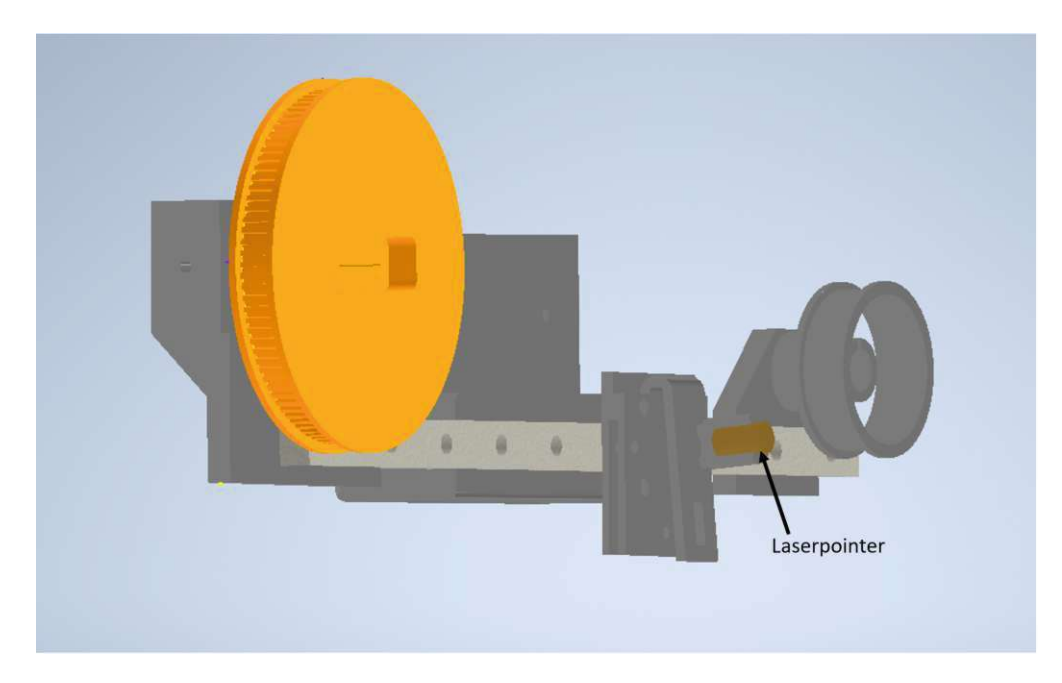


Figure 5.11: The components used for linear motion of the laser diode.

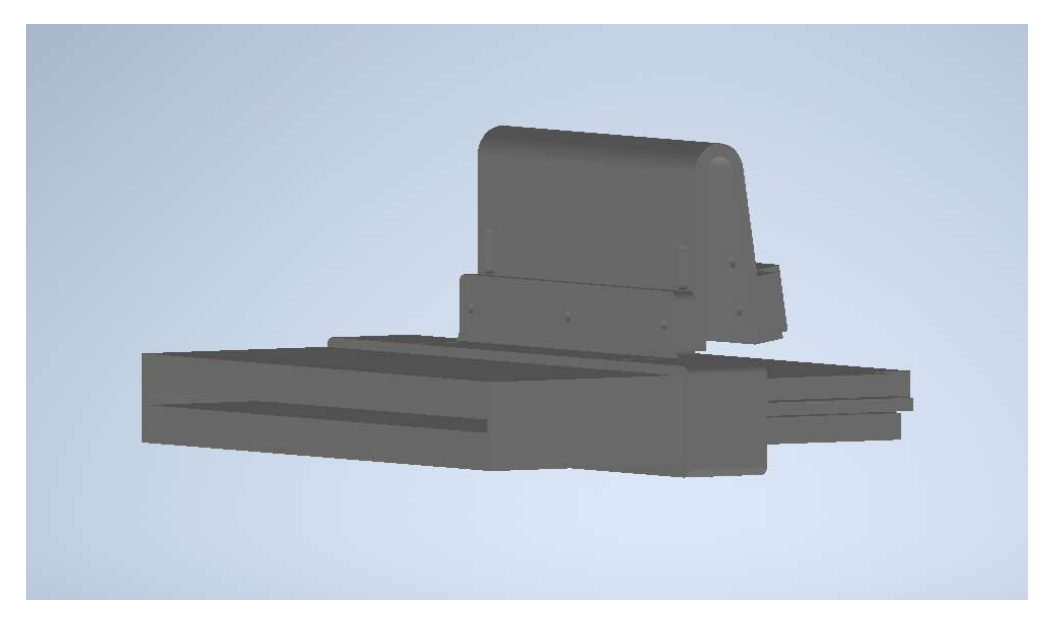


Figure 5.12: The components that hold and help align the focusing lens.

The entire light barrier is mounted to a rail that is positioned on top of the triangular frame. One issue with this positioning is that the detector and the X-ray tube can not be replaced without removing the rail. An explanation on how to remove and correctly align the rail can be found in the appendix in section 10.3. The rail has to be placed in the 3D printed pins, which consists of two separated threads the lock the pin at the correct position. This is intended to help with the alignment of the light barrier.

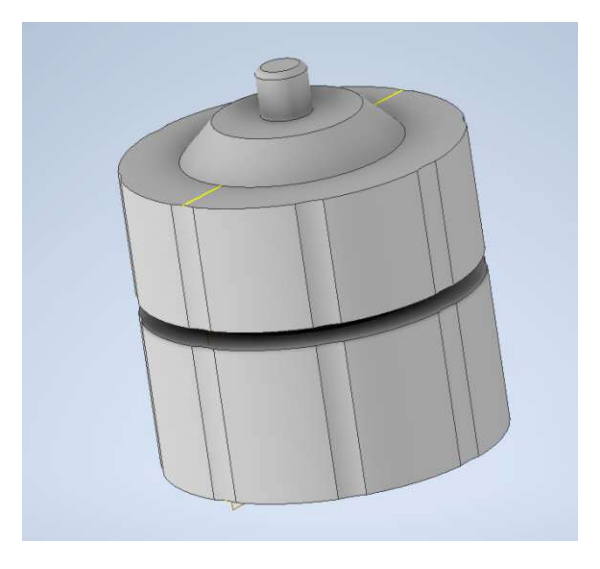


Figure 5.13: The pin the rail is placed on.

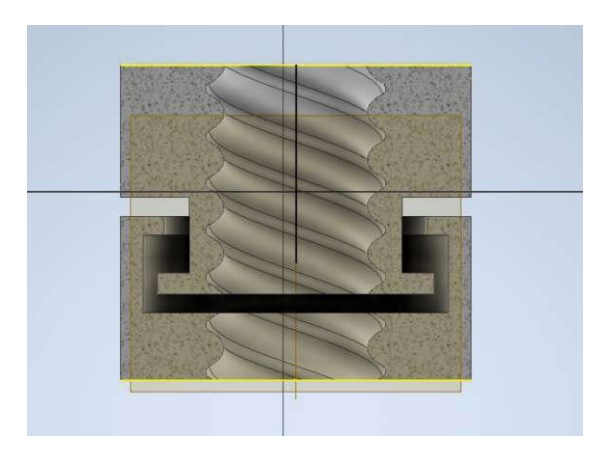


Figure 5.14: The cross-section of the pin, showing the two separate thread segments. Twisting the segments against each other increases the friction thus locking the position of the pin on the thread.

# 5.5 Schematic of the System

An overview of the electrical connections and wires is given below in figure 5.15. Wires that run behind the frame are shown as a dashed line. Furthermore, at the top of the wooden board, the wires have been labelled to indicate the connected device. The schematic has been made using the program ProfiCAD.

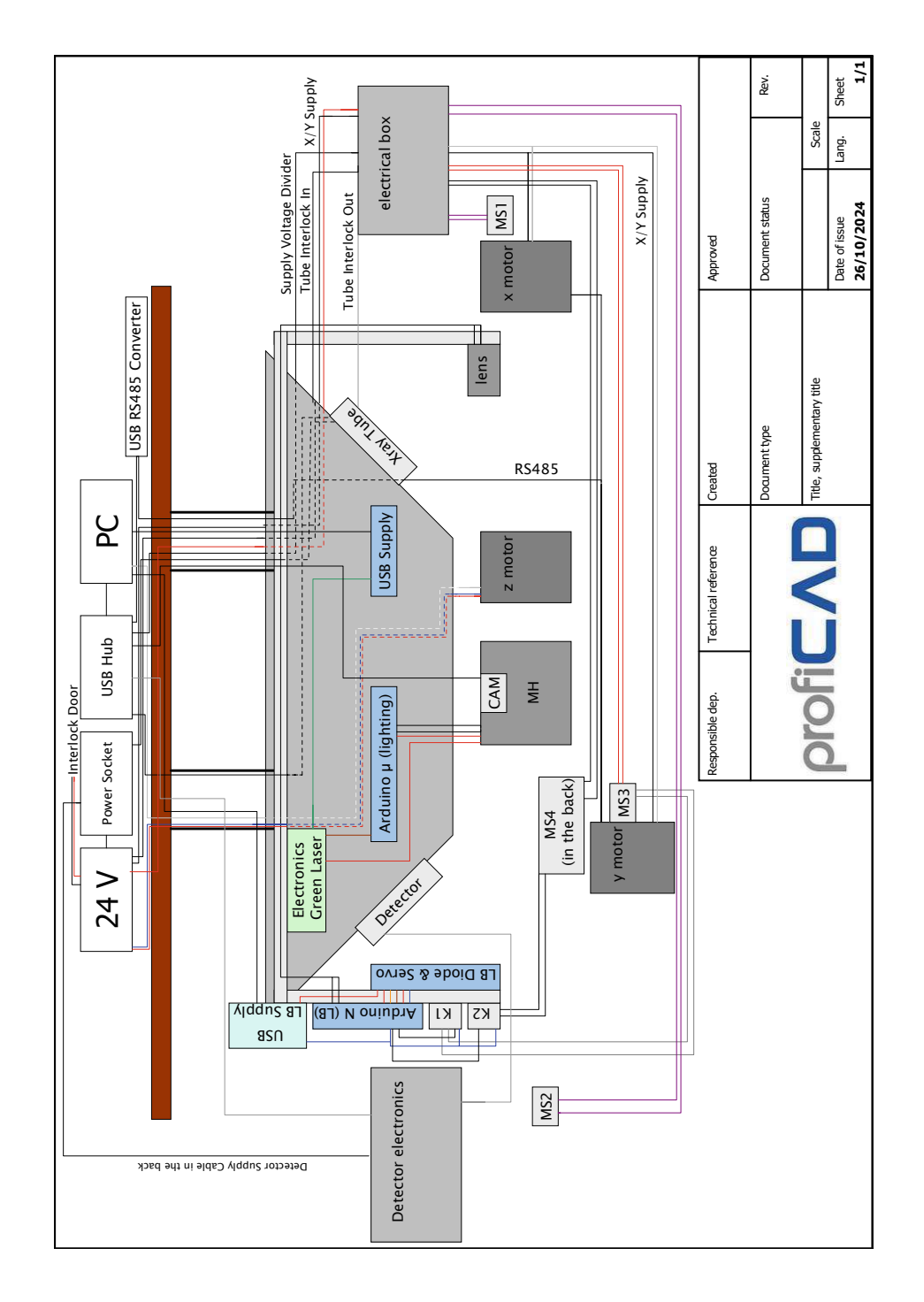


Figure 5.15

# 6 Z Position Optimization

## 6.1 Distance dependent Loss of Counts

The X-ray tube only excites a relatively small portion of the sample, while the detector only detects the fluorescence photons from a specific part of the sample, hence it is paramount to verify that the detector captures the signal that is best excited by the source. Otherwise, a loss in intensity is to be expected. The measurements below aim to quantify this behaviour.

The first set of measurements has been performed on a thin Au layer (roughly  $500\mu m$ ) on glass under the following conditions:

- V=40kV
- I=15µA
- Measurement time per point: 20sec

A few selected points have been re-measured to also test the reproducibility. Considering the statistical error is  $\Delta N = \sqrt{N}$  where N is the number of counts for this measurements [8] it can be assumed that the repeatedly targeted position has correctly been reached. In the table below the deviation from the optimal position is noted with the corresponding count rate. Only a deviation of 0.9mm already results in a count loss of roughly 10%.

Distance from		
optimal position		
in mm	gross Counts 1	gross Counts 2
-1.5	36893	
-0.9	44033	
-0.3	48261	48612
0	49513	49400
0.3	48569	
0.9	45049	

A similar behaviour can be observed when examining the second measurement, which was performed using the same measurement setting as the previous scans. The sample was a fluorescence screen with a Gd layer of unknown thickness. The measurements have been repeated on the optimal point, which shows that the counts are within the statistical error.

Distance from			
optimal position			
in mm	gross Counts 1	gross Counts 2	gross Counts 3
-0.6	23703		
-0.3	24874		
0	25566	24985	24912
0.3	25122		
0.6	24014		

These measurements highlight the importance of measuring at the optimal position. It was agreed that a deviation from the optimal position up to 0.5mm still yields acceptable results. This is the precision that is required from the implementation.

## 6.2 Adaptation to Setup of Height Optimization

In the original design, two red laser diodes have been inserted in the measuring head, in such a way that they cross each other in this optimal position. One of these red laser diodes has been replaced with a green laser. The orientation of these different lasers allows the software to distinguish between z positions below the optimal point and above it. This setup, however, requires an external power supply since the Arduino is not capable of supplying both laser diodes, since the power consumption of the green laser diode by itself exceeds the maximum power output. The added components are shown below in figure 6.1.

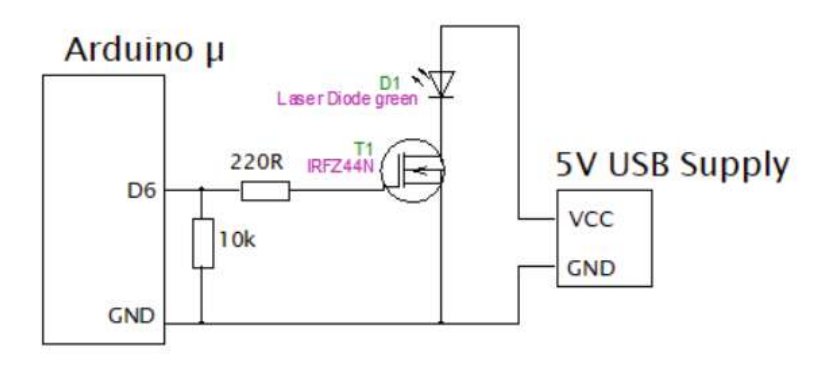


Figure 6.1: A USB cable supplies the laser diode with 5V and the intensity is regulated using a MOSFET controlled by the Arduino.

The geometry of this setup is further illustrated in figure 6.2.

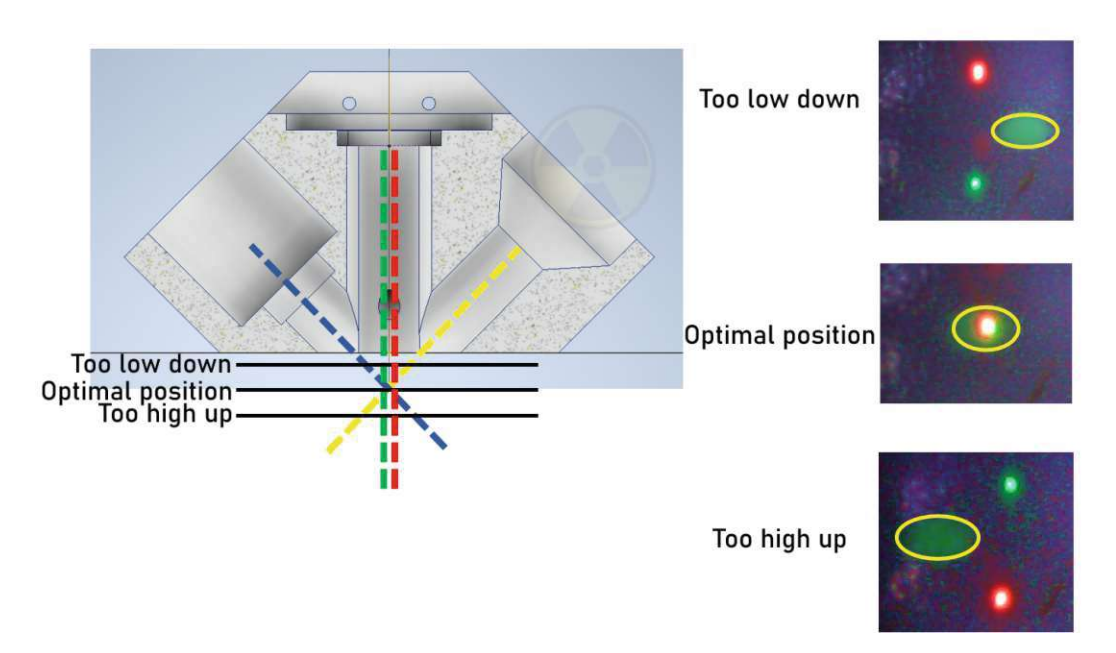


Figure 6.2: Left: a cross section displaying the optimal position. Right: the orientation of the laser pointers and the X-ray spot for different z positions.

The left-hand side shows a cross section of the measuring head, where the path of the X-ray beam is shown in yellow, the centre of the 'point of view' of the detector in blue, and the laser pointers in green and red. Using a fluorescence screen, the X-ray spot can be made visible. The distance between the measuring head and the sample results in three cases, which are illustrated on the right-hand side of the picture.

## 6.3 Integration of YOLOv5

As explained in the previous section, the laser pointers cross each other in the optimal position for the measurement; hence, the orientation and distance between these spots can be used as parameters to regulate the distance between the sample and the measuring head. The optimization of the z coordinate, or the height, relies on the usage of a visual artificial intelligence (see section 3.12). The open source software YOLOv5, where YOLO is an abbreviation for You Only Look Once, was used. [26]

To train the AI, pictures have been captured using the camera located on the top of the measuring head. The pictures contained a series of different distances between the measuring head and the sample surface and multiple samples were used to increase the variety of the training and validation data sets. The labelling was performed using the open source software labelImg [27].

The AI has been trained to detect four classes, one for each laser pointer, green and red, and one for each orientation of the laser pointers, in other words, if the distance to the sample surface is too high (class= too high up, green laser pointer on top), or if the distance is short (class= too low down, red laser pointer on top). A successful detection results in an output file containing every detected class, followed by the coordinates of the top left corner and the height and width of the detected object.



Figure 6.3: A screenshot of the software labelImg.[27] The rectangles indicate the location of an object and the colour indicates the class. The detected classes are also listed in the column on the right side of the picture.

Detections will look similar to the ones in figure 6.4, where the object has been labelled and colour-coded. Furthermore, the confidence of the specific instance of detection is also added. This can be used as a threshold to filter possibly unreliable results. A dataset of roughly 1600 pictures was used to train the machine, of which a fifth has been used for validation. An effort has been made to vary the sample surfaces and laser intensities to incorporate as many use-cases as possible in the training.

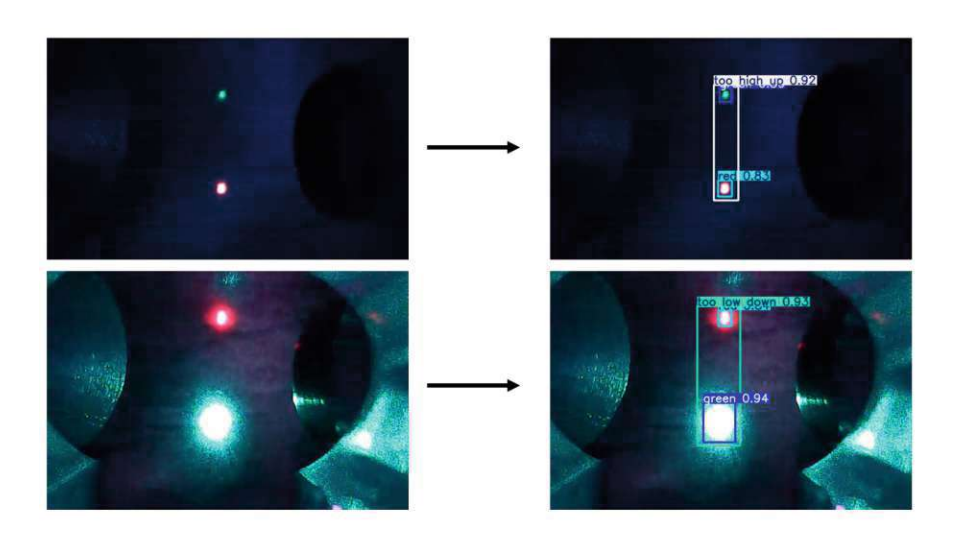


Figure 6.4: The laser pointers are mapped correctly for different laser intensities.

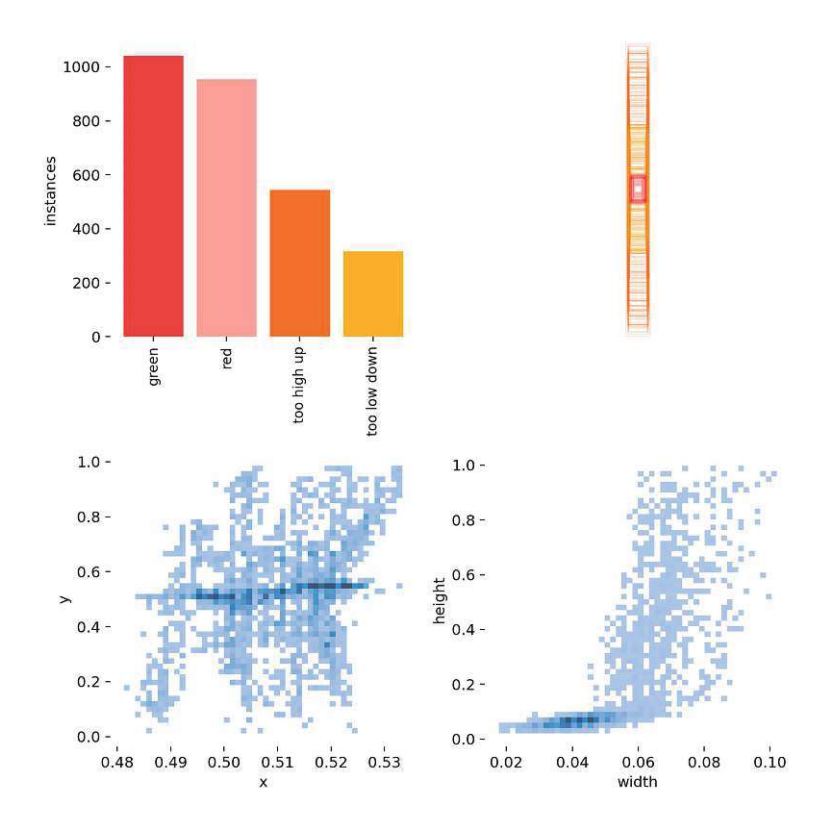


Figure 6.5: An overview of the labelled data.

Figure 6.5 shows in detail how many objects have been labelled for each class (top left). Furthermore, the locations for each of the labels is indicated (top right). Below in figure 6.6 a more detailed illustration for the coordinates, height, width and distribution for the labels is given.

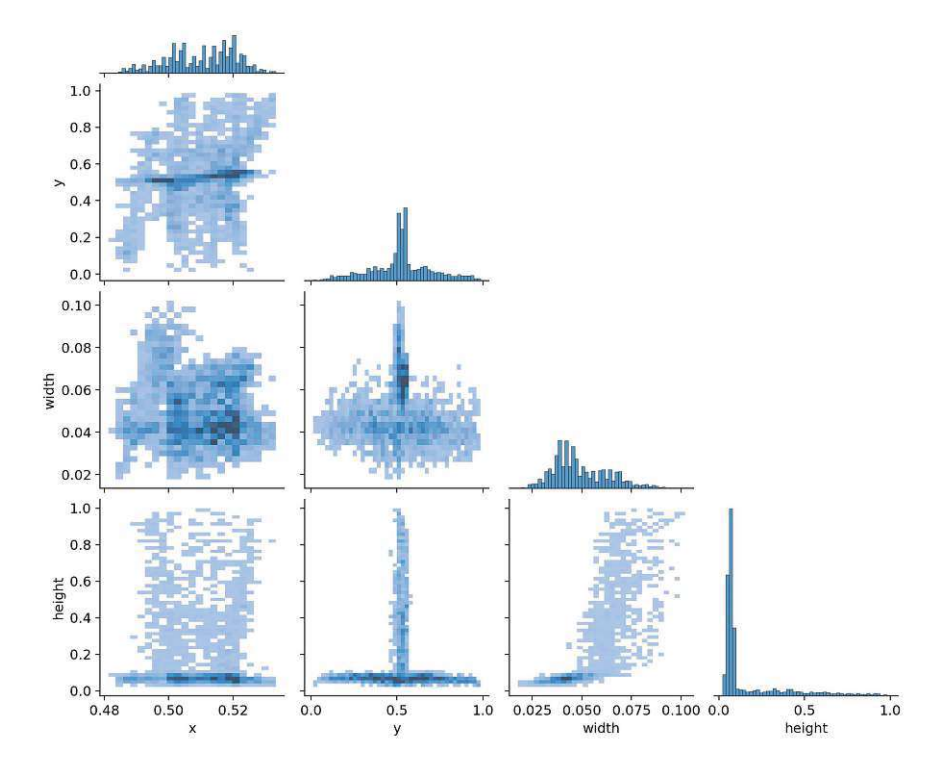


Figure 6.6: Locations and dimensions of the labelled objects.

The following figure shows the result of the training process.

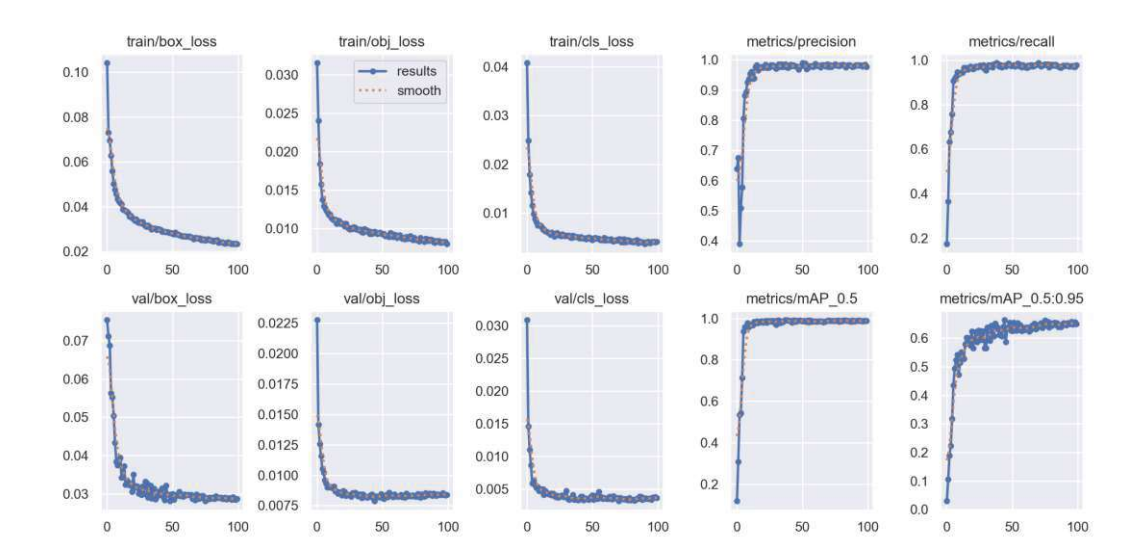


Figure 6.7: The first three plots in the first and second row concern the training and validation data set respectively, they display the loss (section 3.12). Classes loss (cls loss) measures the error for the classification, objectness loss (obj loss) calculates the error in the detection depending on if the object is in a certain grid cell or not and box loss (box loss) measures the error when determining the location of the box [28]. The plots for mAP (mean average prediction) show how often at least 5% or 95% of the area of the prediction overlaps with the area of the label. [29]

Below in figure 6.8, the so-called confusion matrix is displayed. This visualizes how often the predicted object has been detected correctly and how often it has been predicted as the wrong class. A "perfect" result would only contain "1.0" along the main diagonal.

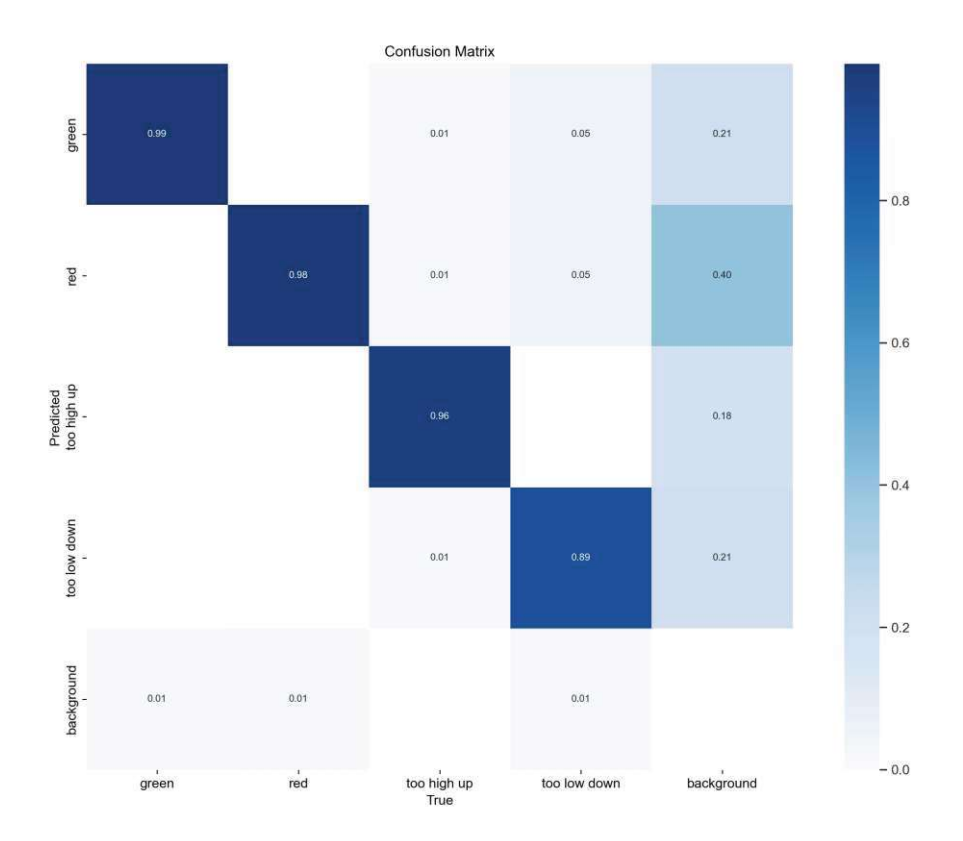


Figure 6.8: The resulting confusion matrix of the AI model.

Figure 6.9 shows the relation between the distance detected by the AI and the physical distance between the measuring head and the sample. The results of the AI detection are given in the height of the detection relative to the total height of the picture. The scans have been performed using different sample surfaces with noticeably different textures and colours. This includes the reflective surface of aluminium, pertinax in which the laser point scatters over a larger area and a black fabric, which absorbs a majority of the light. For each material the intensity of the laser has been adjusted to be of roughly equal brightness.

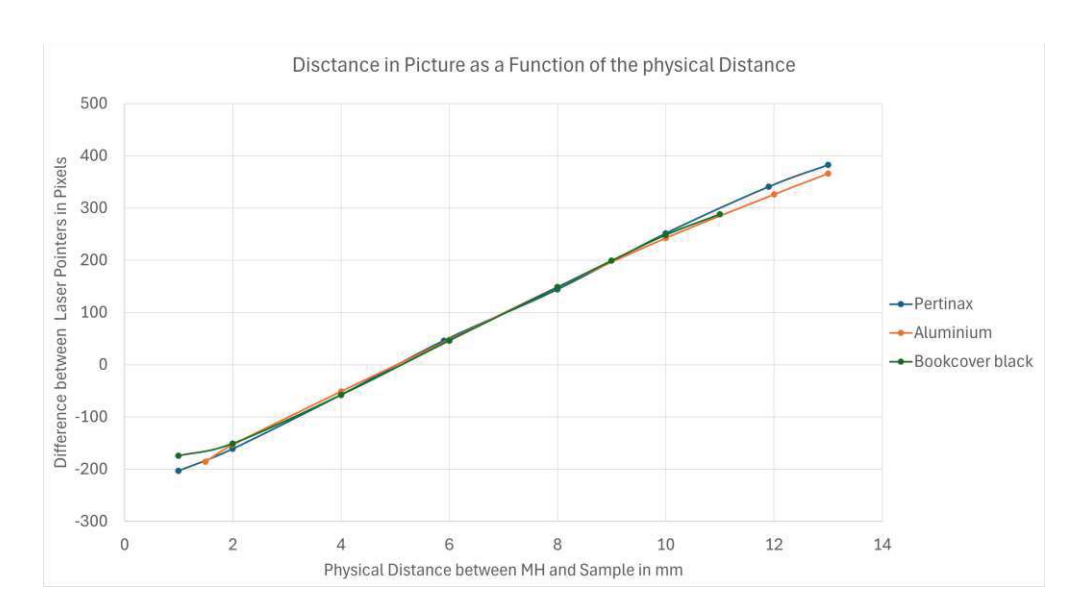


Figure 6.9: The relation between picture height and physical distance for different sample surfaces to the measuring head (MH). Below the optimal position, the difference of the laser pointers in pixel are negative.

Over most of the measured range, the behaviour shows a linear relation between the difference of pixels and physical distance.

Before the model can be implemented to the main program X - Spect it has to converted from python to C#, in other words, it has to change from a .pt file to a .onnx file. The package containing Yolov5 includes a file that allows the user to change to C#:  $python\ export.py-weights... \ weightname.pt-include\ onnx-dynamic.$ 

The difference of the y components of the two lasers is used as the parameter to calculate the distance to move up or down. Specifically, the top left corner of the detected object is used as the current position of the laser. The decision in which direction to move is then made by checking if only one of the classes too high up or too low down is detected.

In the program X - Spect the control for the optimization of the z coordinate can be found under Window - > Distance Yolo. Pressing the button Execute results in movement of the measuring head towards the optimal position when both laser pointers are in view of the camera.

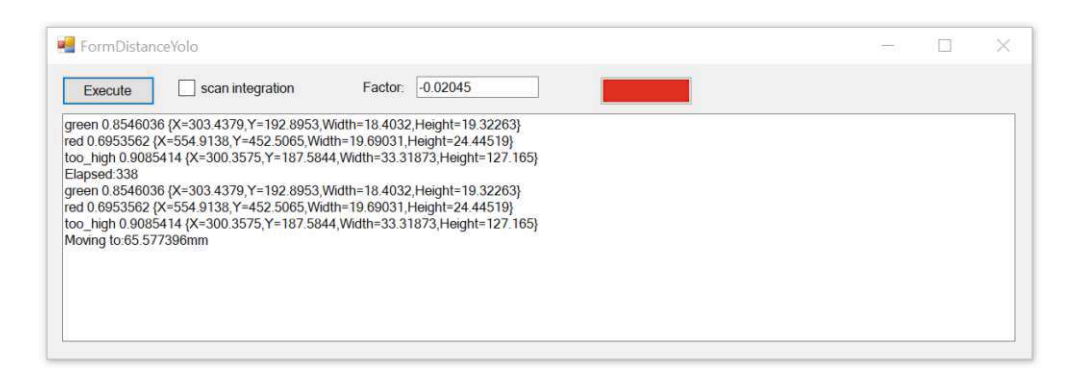


Figure 6.10: A screenshot of the DistanceYOLO window. The detected objects are listed as well as the time it took to make the prediction.

# 7 Safety Features of MAXI

Safety measures have been included in order to prevent both the spectrometer as well as the measured object/sample from taking damage.

## 7.1 Anti Collision - Light Barrier

The first safety feature that has been included is the light barrier. This system consists of one movable laser pointer, the light sensor including the focusing lens and an Arduino nano which is used for evaluating the signal. The laser pointer, which is mounted to a rail that can be moved by a servo motor, just below the measuring head. The light sensor is placed on the opposite side (see figure 7.1 below for a layout). In the case that no obstacle is positioned between the laser pointer and the light sensor, the laser beam will be redirected to one of the light depending resistors (LDRs) by the focusing lens. The light barrier requires a small set of electronics: an Arduino nano, which manages the readout of the voltage drop of the LDRs and controls the servo motor which moves the laser pointer along a rail.

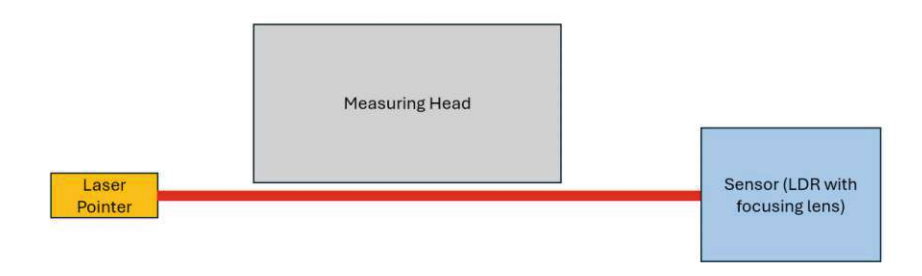


Figure 7.1: A layout of the side view of the lights barriers major components

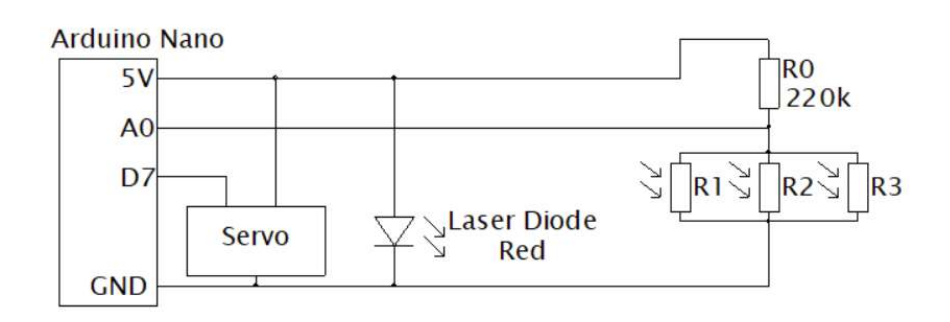


Figure 7.2: The circuit used to control the servo motor and readout the voltage drop at the resistors. The letter 'A' indicates the analogue pins and the letter 'D' indicates the digital pins of the Arduino.

The light barrier serves two functions. Firstly, during downwards movement of the z motor, it checks whether the distance between the measuring head and the sample surface is big enough to avoid any collisions. Secondly, during movements along the y axis, the laser is positioned to one of the sides of the measuring head to detect and prevent imminent collisions.

### 7.1.1 Design of the Focusing Lens

Looking at figure 7.3 it is assumed the laser beam travels from the top of the picture to the bottom, anti-parallel to the y axis. Using the law of refraction by Snellius (see section 3.10), the refracted beam can be determined. However, in most cases, this path will never intersect with the point of origin, which is where the LDR is positioned. Hence, it is necessary to tilt the slope y' (coloured orange in figure) slightly by a small angle  $\delta$ . The slope is tilted until the gradient of the refracted beam is equal to or smaller than the line that connects the current x/y position with the point of origin.

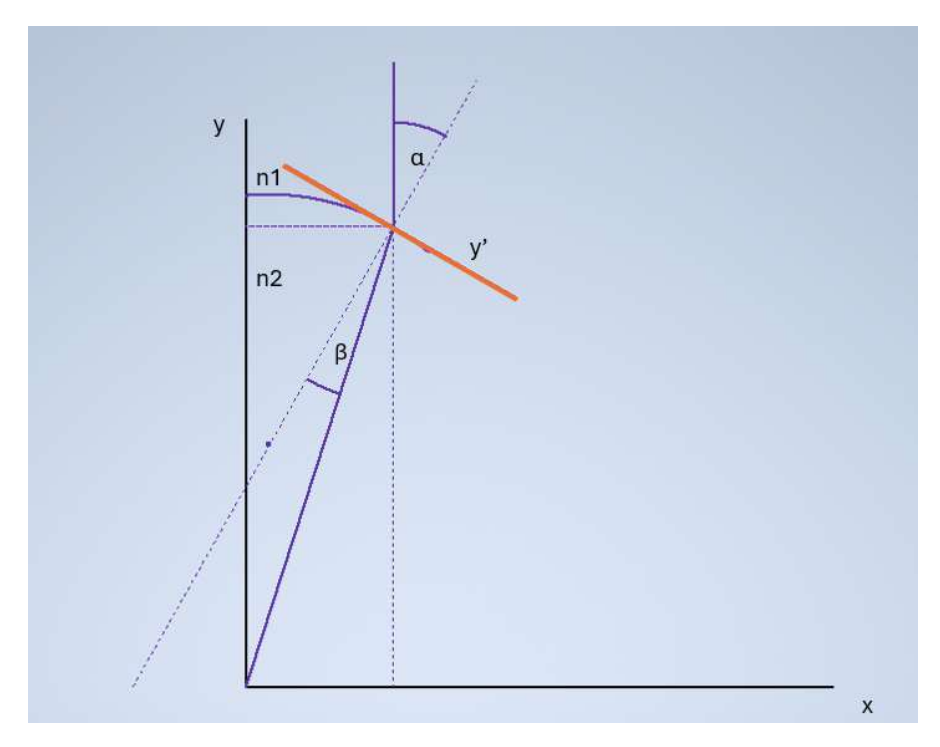


Figure 7.3: A sketch highlighting the parameters used to design the lens. The dotted line indicates the normal to the interface of the two media.

The Euler method (see section 3.11) was used to calculate function y which is the shape of a segment of the focusing lens.

The function f(x), which is necessary to calculate the function y (see section 3.11) can be obtained from the geometry sketched out in figure 7.3:

$$\beta = \arcsin(\frac{1}{n_2} * \sin(\alpha + \delta)) \tag{7.1}$$

$$k_{\beta} = \arctan(\alpha + \delta + 90 - \beta) \tag{7.2}$$

The lens is made up of three of these calculated segments in order to span across a length of 10cm, which is 2cm longer than the width of the measuring head. The refractive indices were approximated as  $n_1 = 1$  for air and  $n_2 = 1.5$  for resin.

This shape has been modelled to 3D printable positive mold, which has been used to make a negative silicon mold. This silicon mold was used to make the final lens out of resin. At each of the focal points of the lens, a slit has been milled, where the light depending resistors have been placed.

It should be noted that due to a coding error in the calculation, the curvature of the

shape is slightly too strong. This minor deviation, however, is within the tolerance since because of the relatively large active surface area of the LDR. The program has since then been corrected and can be found in the appendix under 10.1.

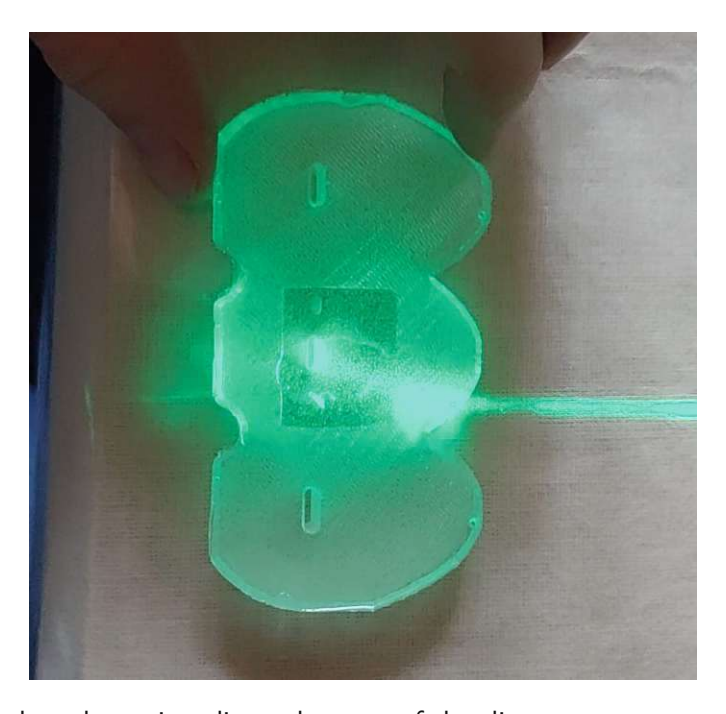


Figure 7.4: The laser beam is redirected to one of the slits.



Figure 7.5: The finished lens with the inserted light depending resistors.

In the case of a blocked beam, the Arduino will register a relatively high voltage, which corresponds to a logical low. Figure 7.6 and 7.7 illustrate the two cases. This signal in then in turn interpreted by the Arduino and sent to the main program after a status query.

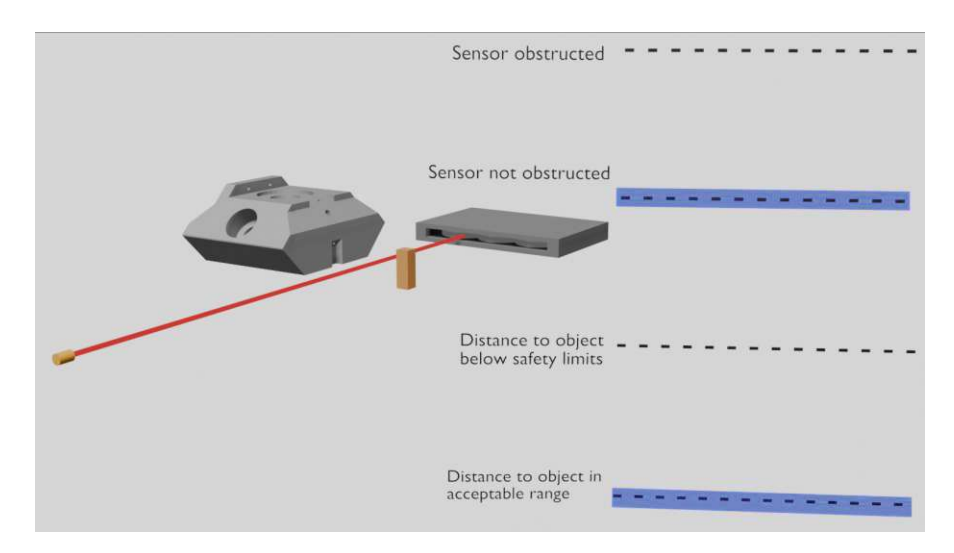


Figure 7.6: A render of the basic components of the light barrier system for the case that no obstacle has been detected. The interpretation of the logical signals is shown on the right side.

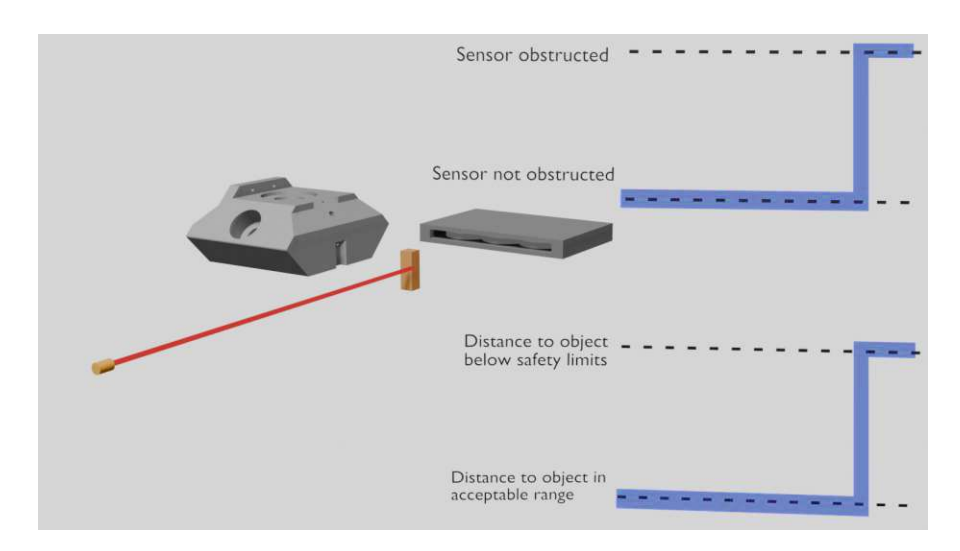


Figure 7.7: A render of the basic components of the light barrier system for the case that an obstacle has been detected. The interpretation of the logical signals is shown on the right side.

### 7.2 End Switches

The second implemented safety feature is a set of micro switches mounted on both end positions for both the x and y motor. The SMC-I12 controller board on each of the stepper motors has digital inputs which can be programmed by the user to serve different functions. Using the program NanoPro by Nanotec [30]. Figure 7.8 shows a screenshot of the program NanoPro and the interface used to choose the settings for the communication between the motor controller and the PC. The settings:

• COM 5

• Baudrate: 115200

x motor: drive address 1

• y motor: drive address 2

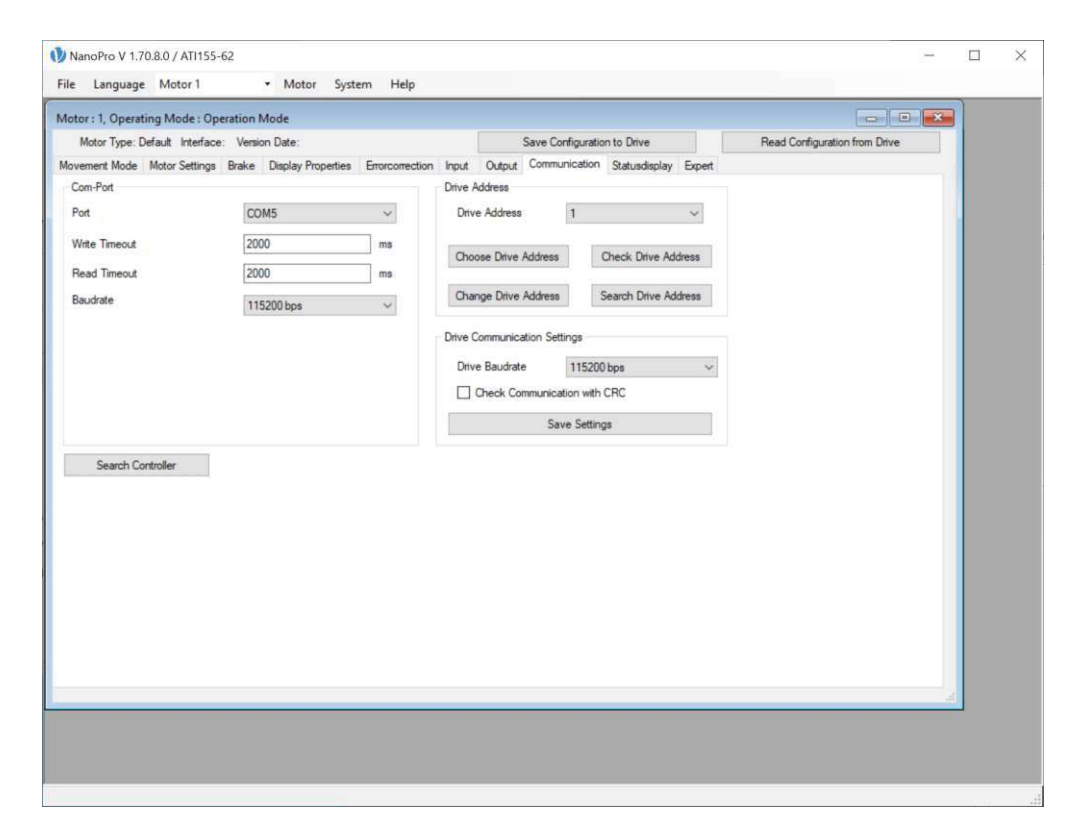


Figure 7.8: A screenshot of the communications tab in the NanoPro software. This is used to select a motor and check connections.

When changing settings on both motor controllers one must make sure to change the drive address and save the settings using the button.

Under the tab 'Input', the configuration for each digital input can be defined. In the bottom left in figure 7.9 the settings for the switch can be defined. The used micro switched are closers and the option 'Free backwards' under the point 'During Normal Operation' immediately stops any movement of the motor and only allows movements in the opposite direction as the one that was active when the switch was closed. For this application, the inputs 1 and 2 have been used and set to 'External reference switch' in the right of figure 7.9.[31]

This has been done for both motors.

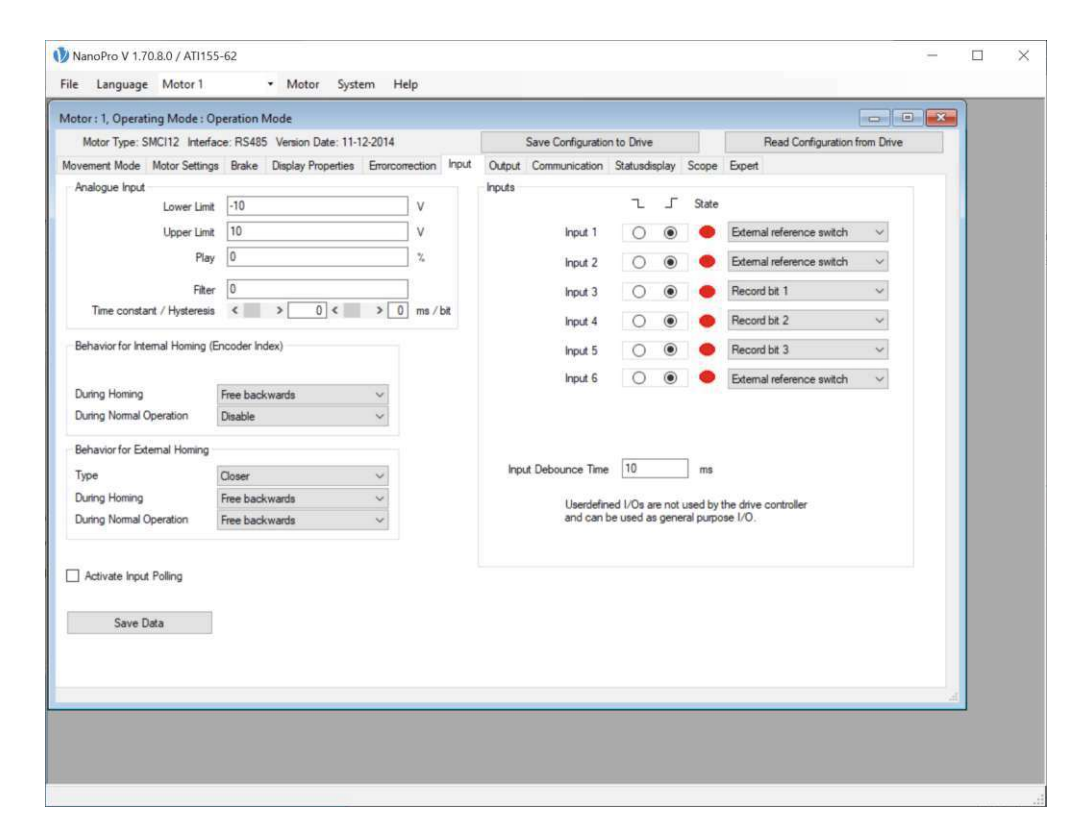


Figure 7.9: A screenshot of the Input tab in the NanoPro software.

Each microswitch have been incorporated in a voltage divider, illustrated by the schematic below.

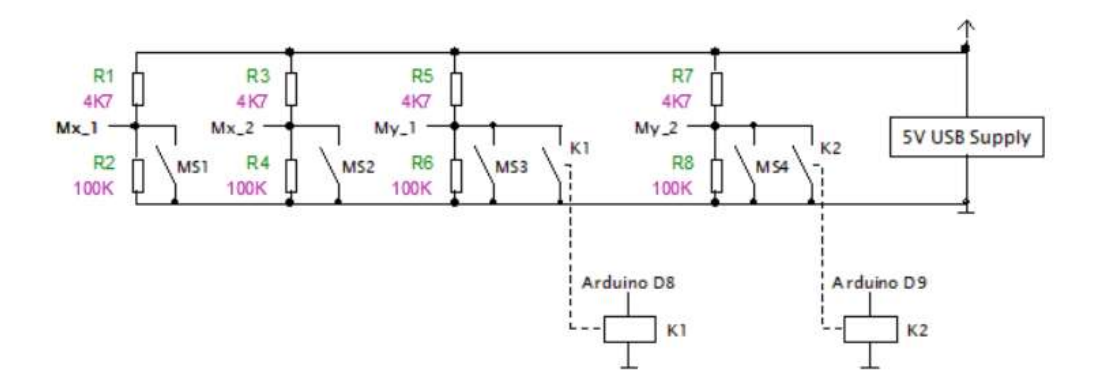


Figure 7.10: A schematic of the voltage dividers for the microswitches. The number behind the underscore indicates which digital input on the microswitch controller the wire is connected to. Furthermore, parallel to the end switches of the y motor, relays are included, these relays allow for the collision prevention for movements along the y axis.

The board, to which the voltage dividers are mounted, is located in the electrical box behind the spectrometer.

## Measurements

In this section the performed measurements are elaborated upon. The measurements include the determination of the spot size of the X-ray beam, of detection limits, quantification of standard materials, the measurements of test patterns and the evaluation of the safety features.

## 8.1 Determination of the spot size

One requirement for the MAXI is a spot size of the X-ray beam in the mm range to g. This can be verified by scanning across a thin sample, in our case a copper wire with a thickness of 0.15mm mounted on a teflon piece (see figure 8.1).

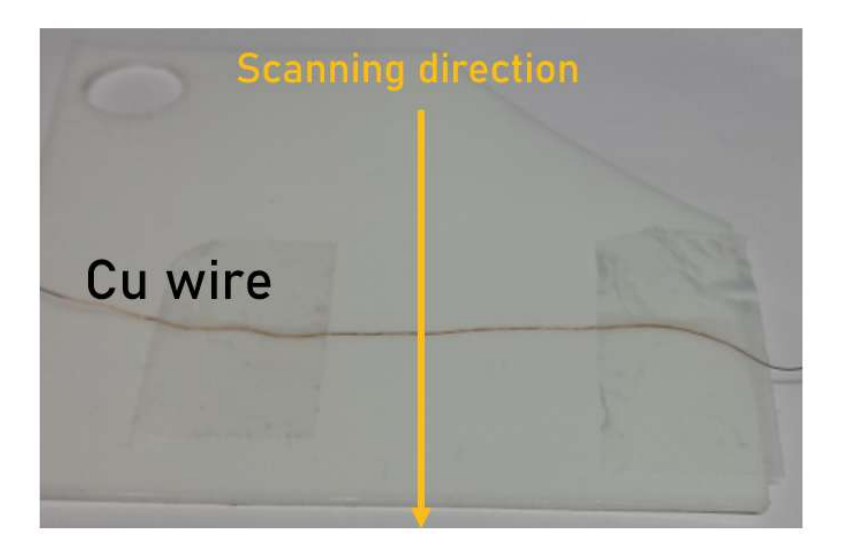


Figure 8.1: The teflon piece with the copper wire attached to it. The scanning direction is orthogonal to the orientation of the wire, which has been indicated with the yellow arrow.

The height of the frame has been manually adjusted to its optimal distance to the sample surface (see section 6 for clarification) and a line scan has been performed in the x and y direction. The following two diagrams (figure 8.2 and 8.3) show the captured copper intensity for the respective line scan. Their shapes follow a pattern that can be approximated with a gaussian, whose full width half maximum (FWHM) is used to determine the spot size. The FWHM for x-direction is 2.00mm and for the y-direction 1.41mm.



Figure 8.2: Measured data in blue. Gaussian approximation in orange. FWHM = 2.00mm

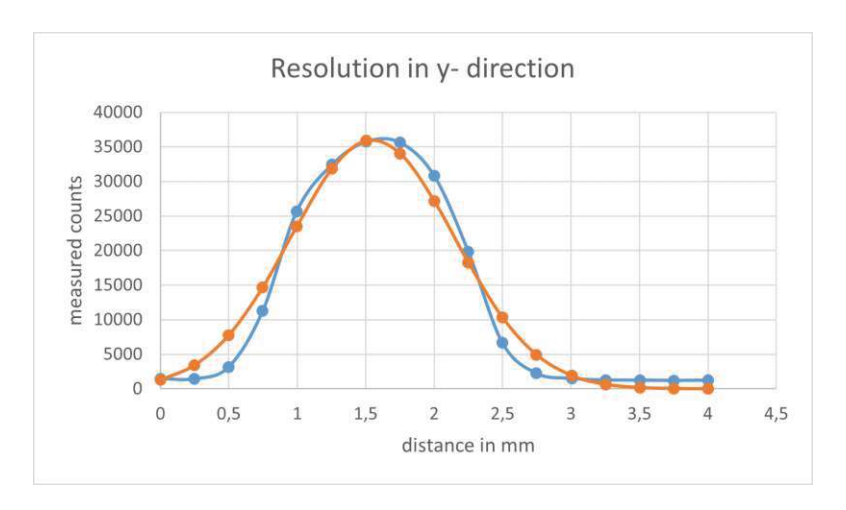


Figure 8.3: Measured data in blue. Gaussian approximation in orange. FWHM = 1.41mm

These curves, however, are not only a result of the spot size but the convolution of the spot size with the thickness of the wire  $d_{wire}$ .

$$spotsize_x = \sqrt{FWHM_x^2 - d_{wire}^2}$$

$$spotsize_y = \sqrt{FWHM_y^2 - d_{wire}^2}$$

Compensating for the dimensions of the wire, the spot size in x-direction is determined to be  $spotsize_x = 1.99mm$  and for  $spotsize_y = 1.40mm$ .

### 8.2 Blank Spectrum

To verify, if the MAXI can be used for the detection of a specific element, a blank spectrum must be acquired. For a clean sample carrier/scatterer of known composition, it can be determined with elements are already in the system. For this verification, two scatterers have been used, a silicon wafer and an  $8\mu m$  kapton foil. The spectrum can be seen in figure 8.4. It has been captured while exciting the sample with the tube setting 40kV,  $15\mu A$  for 1000sec.

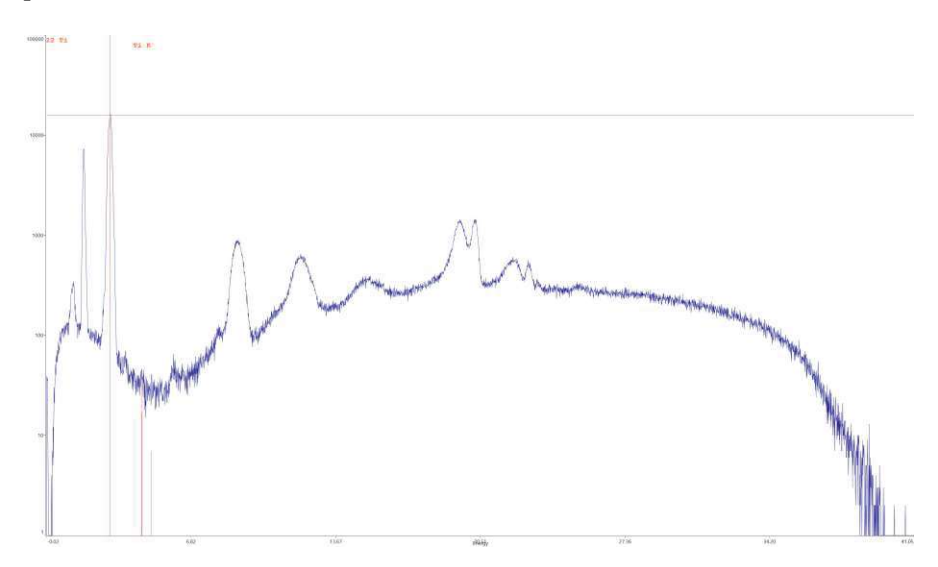


Figure 8.4: An Image of the blank spectrum of a clean silicon wafer.

The spectrum shows a distinct peak at 1.74kV which is the Si  $K\alpha$  peak and expected to be relatively high. Other peaks, which are expected to be in the system are the Rh L lines between 2.7keV and 2.9keV. Furthermore, diffraction peaks can also be seen at 8keV and 11keV At 2.9kV, the Ar  $K\alpha$  line is expected, it seems, however, to be overlapped with another diffraction peak.

The second blank spectrum has been captured using a kapton foil as a scatterer. The resulting spectrum can be seen below in figure 8.5.

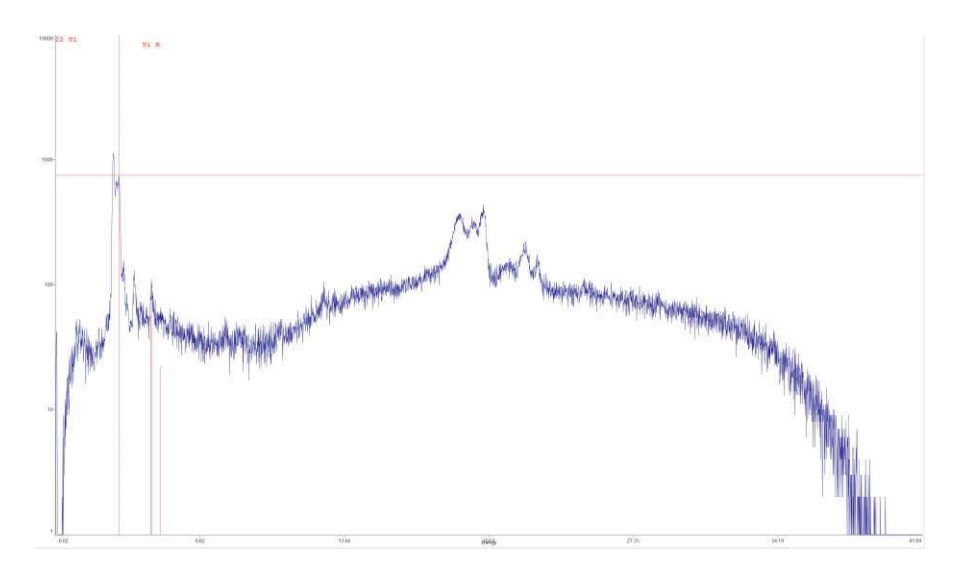


Figure 8.5: An Image of the blank spectrum of a clean kapton foil.

As is to be expected, the scatter peaks for Rh can be seen. Furthermore, Fe and Pb peaks can also be detected. Those elements, however, are contained in low quantities within the foil.

### 8.3 Determination of Lower Limits of Detection

Two samples have been prepared for these measurements. Each time, the sample has been area scanned to find the coordinate with the maximum intensity.

# 8.3.1 500ng of Cu on Kapton Foil

- V=40kV
- I=50µA
- Measurement time per point: 100sec

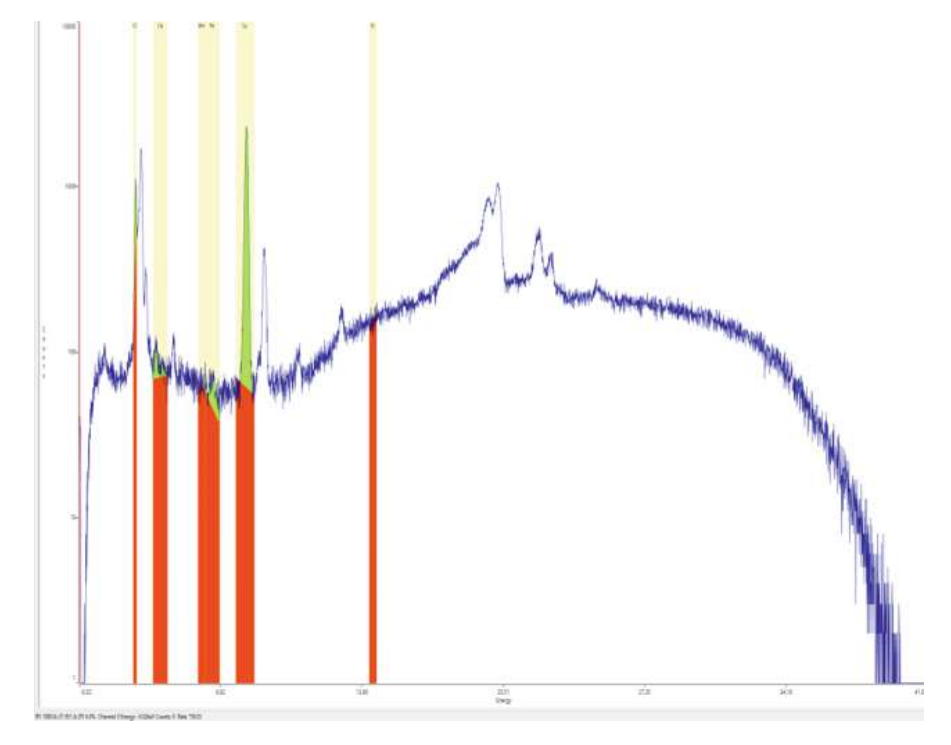


Figure 8.6: The captured spectrum for the Cu sample.

The following table shows the captured counts for the Cu K $\alpha$  ROI. Since the measurement time was 100sec, the results have to be extrapolated to 1000sec get to common  $LLD_{1000}$ .

Net Counts	15283
Background Counts	1295
LLD	1.1ng
Sensitivity	$0.33~\mathrm{cps/ng}$

## 8.3.2 800ng of Mo on Quartz Carrier

- V=40kV
- I=50μA
- Measurement time per point: 1000sec

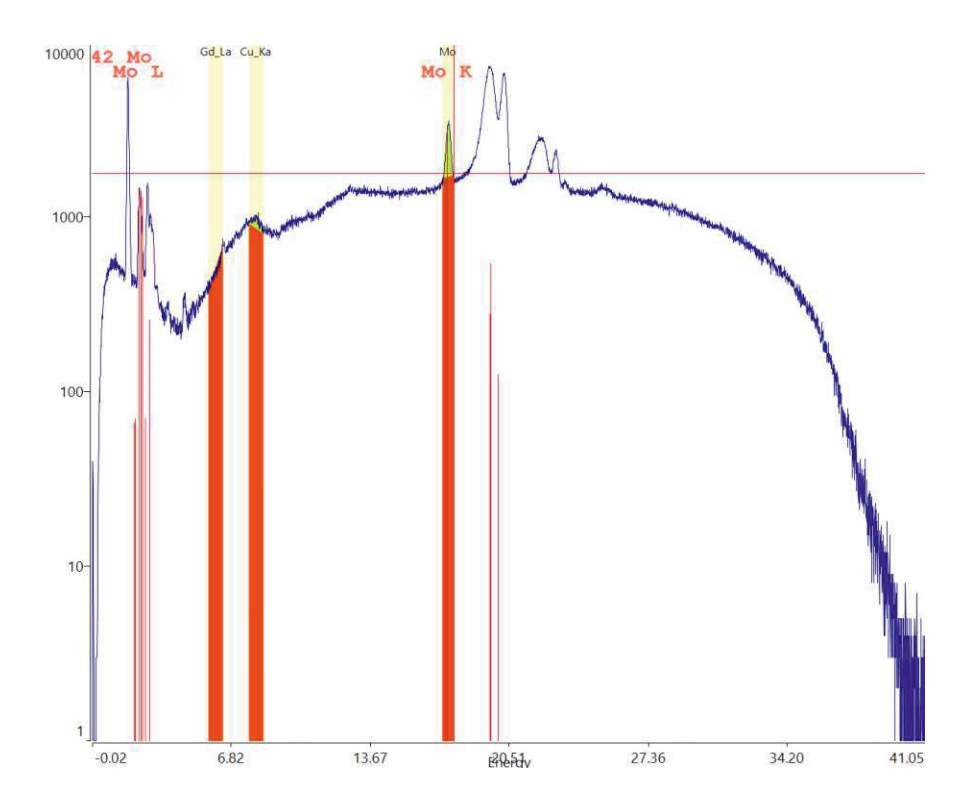


Figure 8.7: The captured spectrum for the Mo sample.

The following table shows the captured counts for the Mo K $\alpha$  ROI.

Net Counts	42185
Background Counts	93858
LLD	17,43 ng
Sensitivity	$0.17~\mathrm{cps/ng}$

### 8.4 Quantification of Samples

This subsection discusses the quantification of some sample standards. It should be noted that the following evaluations mainly serve as a prove of concept to check if the system works in acceptable parameters. A number of improvements to the measuring setup could be made like, for example, longer measurement times and the flushing of the sample with He. The last aspect has only been done for one of the following samples.

### 8.4.1 NIST Brass Standard 1103

The brass standard has been measured in air using 40kV[32]. The fitting was performed with AXIL [11] and the quantification was performed using the in-house developed quantitative analysis software ATIQuant [33].

Symbol	Results in weight %	Certified Values in weight %
Fe Ka	0.37	0.26
Ni Ka	0.22	0.15
CuKa	60.56	59.27
Zn Ka	34.81	35.72
Sn Ka	0.48	0.88
Pb La	3.56	3.73

When comparing the calculated results with the certified values, it can be seen that the values for the main components are within 1.5% of the certified values.

### 8.4.2 NIST Soda-Lime Container Glass Standard 621

The glass standard has been measured in air using 40kV [35]. The fitting was performed with AXIL [11] and the quantification was performed using the in-house developed quantitative analysis software ATIQuant [33].

Symbol	Results in weight %	Certified Values in weight %
$SiO_2$	68.005	71.13
$\overline{Na_2O^*}$	13.00	12.74
$\overline{CaO}$	13.235	10.71
$Al_2O_3^*$	2.70	2.76
$K_2O$	2.5954	2.01
$\overline{MgO}$	-	0.27
$\overline{SO_3}$	0.2345	0.13
$\overline{BaO}$	0.13812	0.12
$Fe_2O_3$	0.042537	0.040
$As_2O_3$	0.016015	0.030
$TiO_2$	0.02.9998	0.014
$\overline{ZrO_2}$	0.00369	0.007

Some of the elements (indicated with \*) could not be determined since He flushing was not used. Therefore, it was necessary to enter values for the quantification, otherwise the result would have been way off. The results for the main components are within a few percent, they could, however, be improved by flushing the sample with He.

### 8.4.3 10 Euro Cent Coin

The coin has been measured in air using 40kV [34]. The fitting was performed with AXIL [11] and the quantification was performed using the in-house developed quantitative analysis software ATIQuant [33].

Symbol	Results in weight %	Certified Values in weight %
Al Ka	5.90	5.00
CuKa	87.89	89.00
Cu Ka	5.33	5.00
$\overline{Zn \ Ka}$	0.88	1.00

Like the measurement before, it can be seen that the values for the main components are within 1.2% of the certified values.

### 8.5 Ammonite

The first sample chosen to test the resolution was an ammonite, whose distinct colour pattern and spiral offer an opportunity to visualize the limits of the MAXI. The following settings were used for the measurement:

• V=40kV

I=50μA

• Range: 25mm\*25mm

• Step size: 0.5mm

• Measurement time per point: 10sec

• Total measurement time: roughly 9h

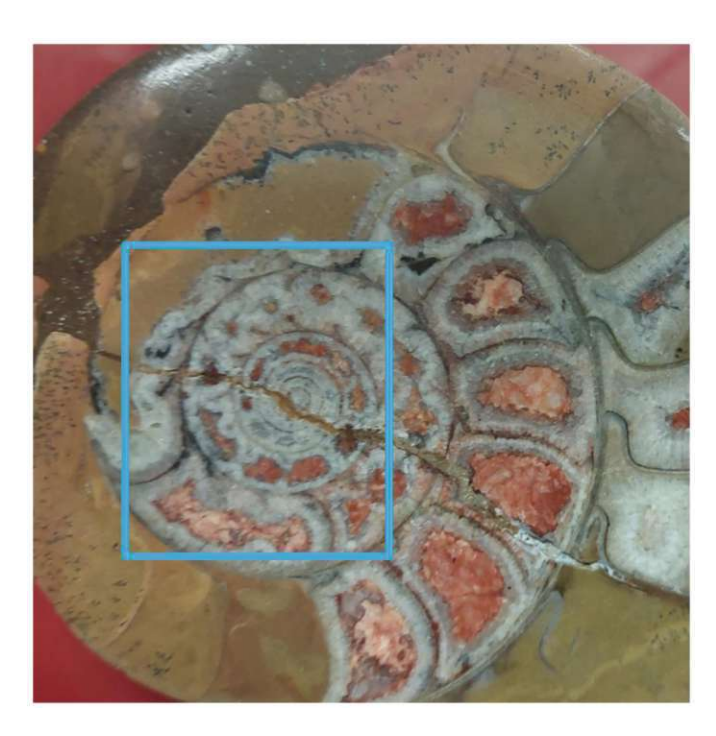


Figure 8.8: A picture of the ammonite. The measured area is located within the blue box.

The captured spectra were mapped using the in-house developed software XRFMapsCore. Since most of the structures are in the mm range it is to be expected that the majority of the features will be resolved. The elemental maps are displayed for Ca, Mn and Fe below in figure 8.9.

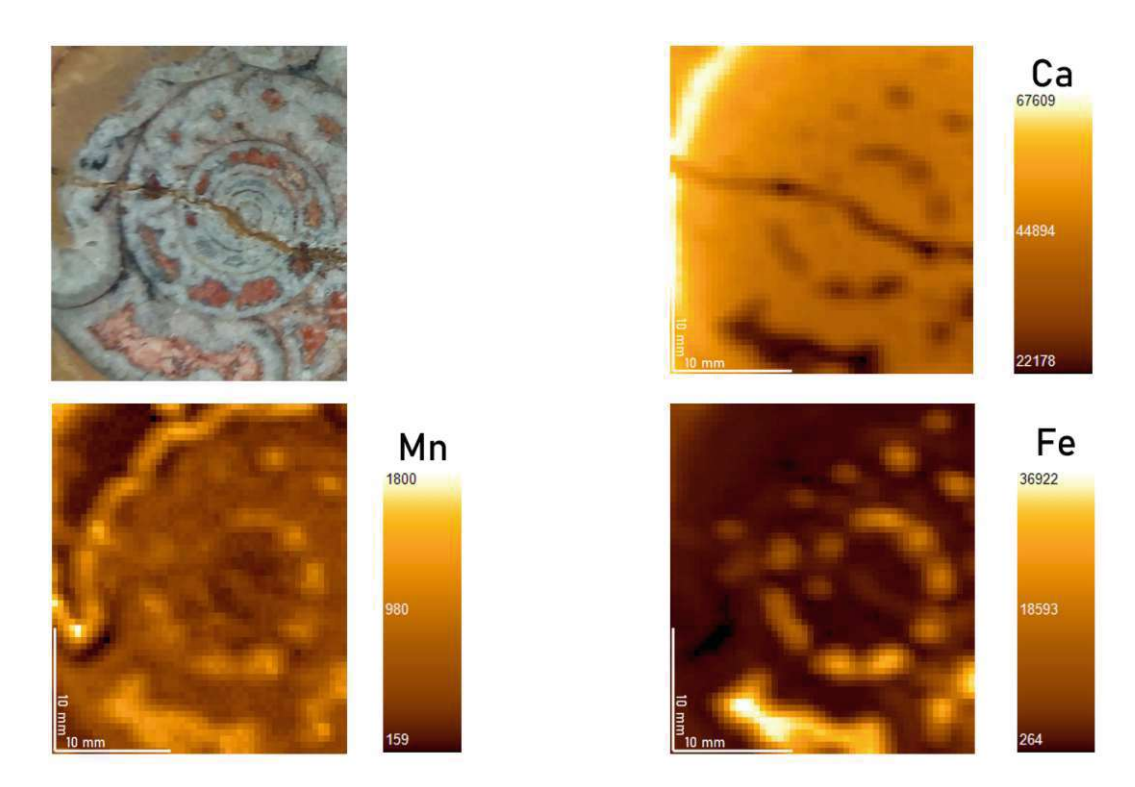


Figure 8.9: Top left: the original picture. Top right: the Ca map shows the crack on the surface of the sample. Bottom left: The Mn map shows that Mn is deposited in the spiral and in the grey area left to the spiral. Bottom right: Fe is primarily contained in the spiral.

When comparing these maps to the original picture it can be seen that even small structure, like the smallest red dot in the spiral, can be resolved (see Fe map).

#### 8.6 Analysis of a Painting

The second sample was a painting on a canvas. A set of only three different colours has been used, thus, making it relatively easy to correlate the measured intensity to the specific paint. The measurements settings were the following:

- V=40kV
- I=50µA
- Range: 55mm\*50mm
- Step size: 1mm

• Measurement time per point: 10sec

• Total measurement time: roughly 6h

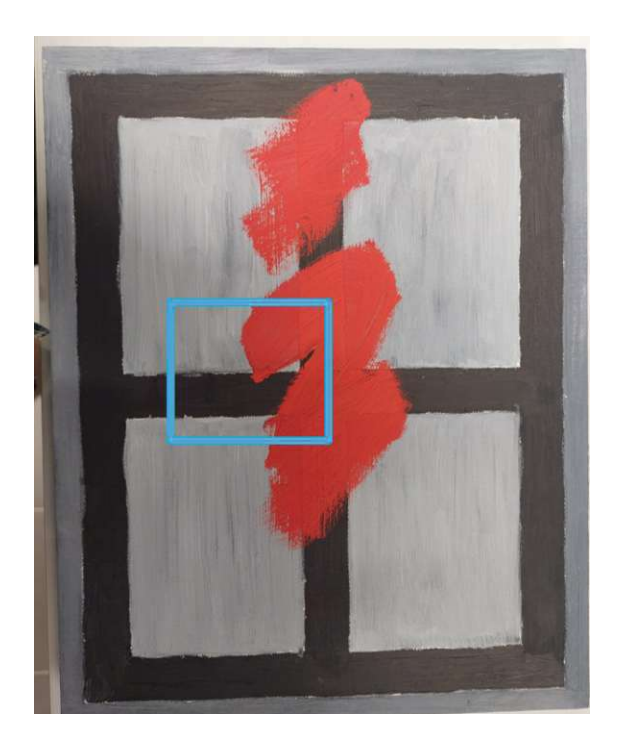


Figure 8.10: A picture of the measured painting. The scanned area has been indicated using the blue boundaries.

Similar to the previous measurement, the captured spectra were converted to a map using the program XRFMapsCore. The resulting maps are shown below for Fe, K, Zn and Ba in figure 8.11.

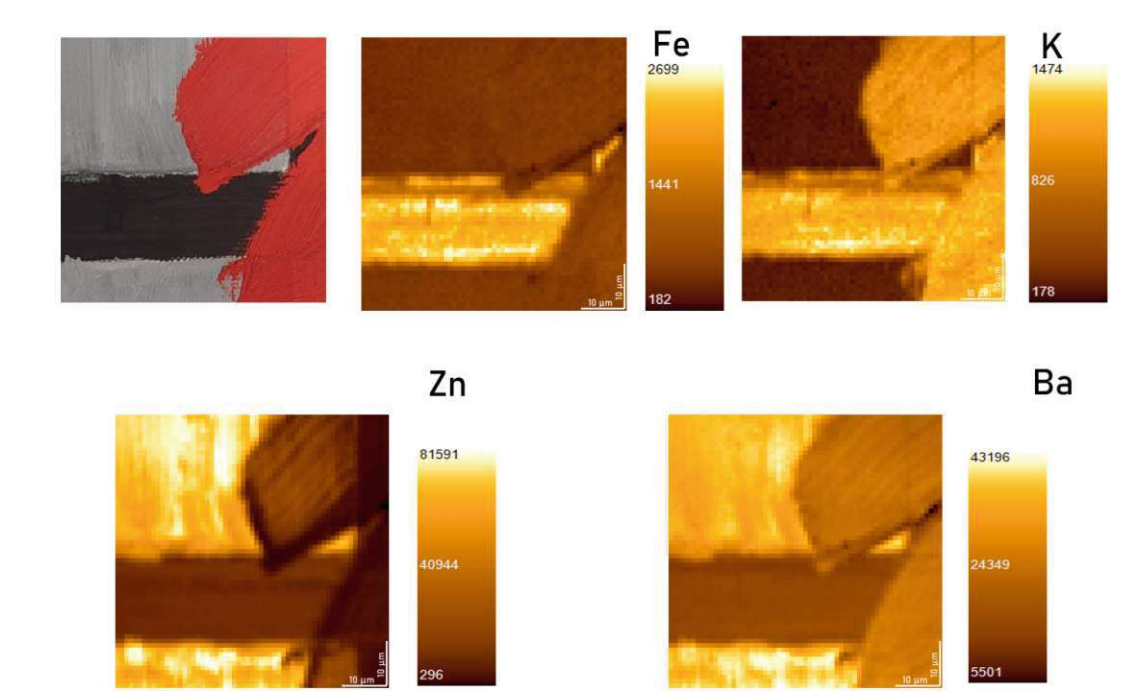


Figure 8.11: Top left: the original picture. Top center: the Fe map shows that the black paint contains more Fe than the other paints. Top right: the K map correlates with both red and black. Bottom left: The Zn map shows that Zn is mostly deposited grey painted area. Bottom right: Ba is contained in every paint to some degree.

#### 8.7 Mapping a Pattern in Cu

Three sets of lines have been milled in a epoxy board covered in a thin layer of Cu. Each set consists of four lines vertically and horizontally milled. The left lines are 0.5mm thick, the lines in the centre are 1mm thick and the lines on the right are 2mm thick.

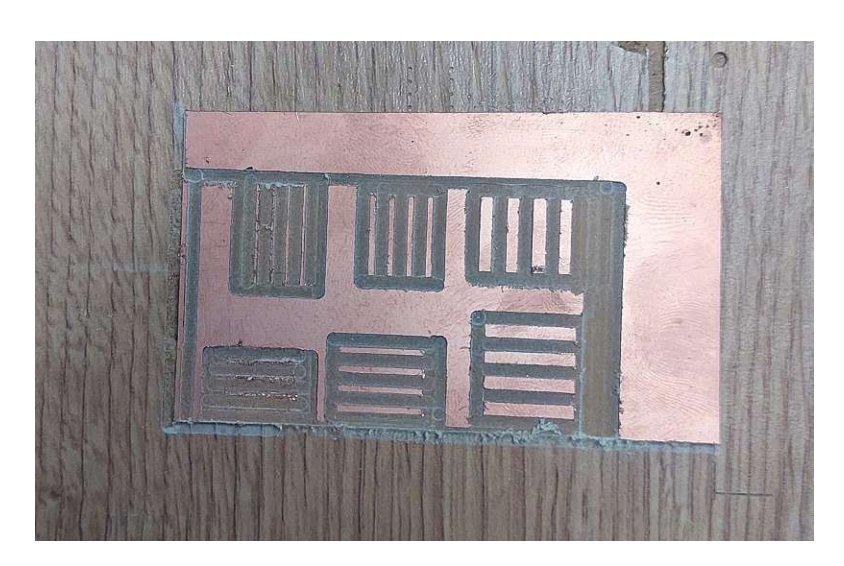


Figure 8.12: A picture of the pattern milled in the epoxy board.

The following measurement settings were used:

- V=40kV
- I=50μA
- Range: 45mm\*80mm
- Step size: 1mm
- Measurement time per point: 5sec
- Total measurement time: roughly 11h

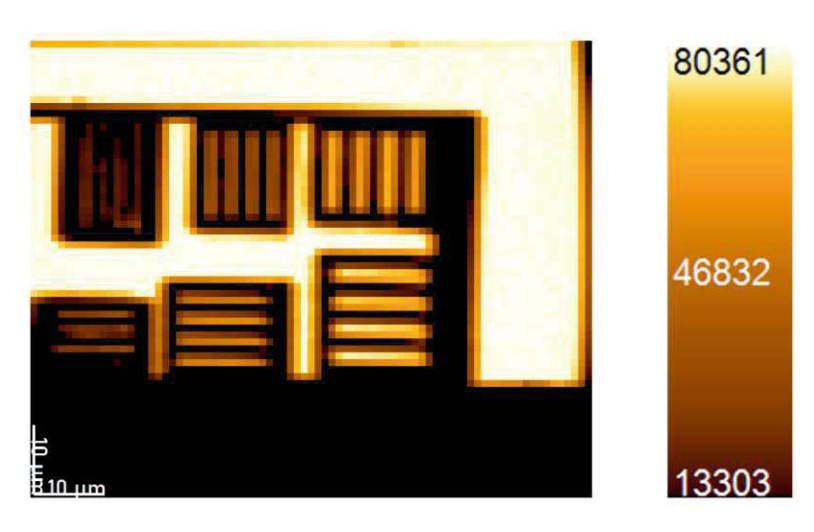


Figure 8.13: The resulting map showing the counts for the Cu Klpha ROI. XRFmapsCore was used for visualization.

The 1mm lines are still well resolved. The 0.5mm lines however, cannot be easily distinguished anymore. Due to the different spot sizes (see section 8.1) the horizontal lines are slightly better resolved.

# 8.8 Determination of Resolution of the Z Optimization

The accuracy of the trained AI (see section 6) partly relies on the minimal deviation from the optimal position that can be detected. In other words, how far the two laser pointers have to be in order to be distinguished by the AI. The following measurements have been performed on different sample surfaces (white carton, aluminium, pertinax, black fabric) and repeated three times for each surface. Firstly, the laser intensities have been adjusted to be roughly equal. Secondly, the z position has been changed to the point where the lasers cross. Then, the position has been changed in 0.1mm steps until the AI was able to recognize two separated laser points in the captured picture. The following four figures display the minimal distance for different surfaces. None of these distances exceed the required minimum distance of 0.5mm.

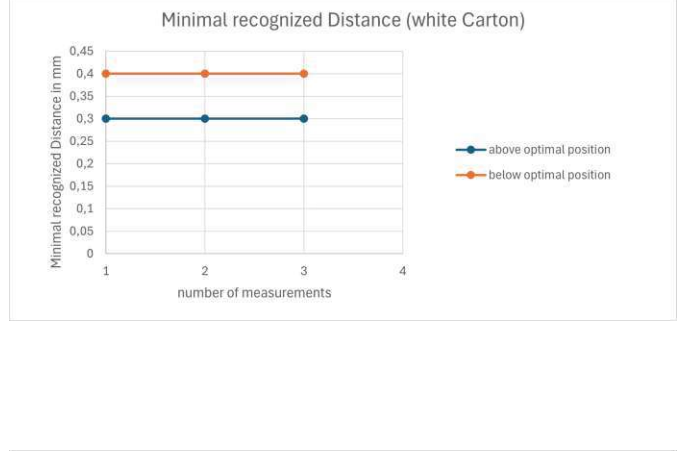


Figure 8.14

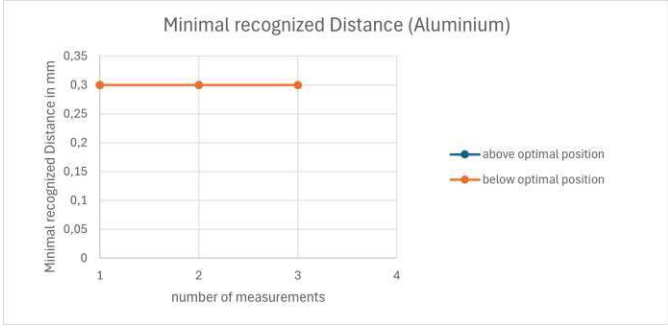


Figure 8.15

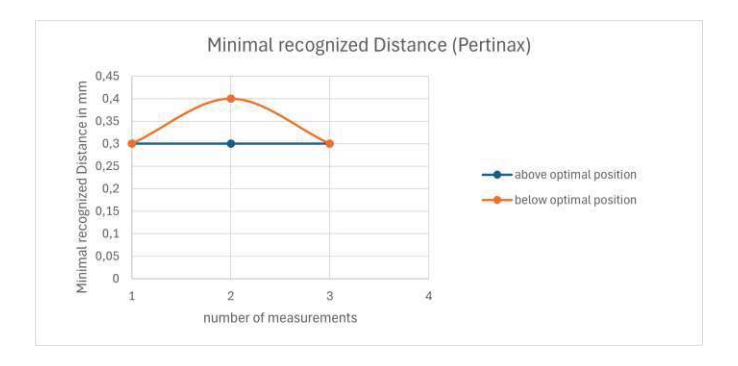


Figure 8.16



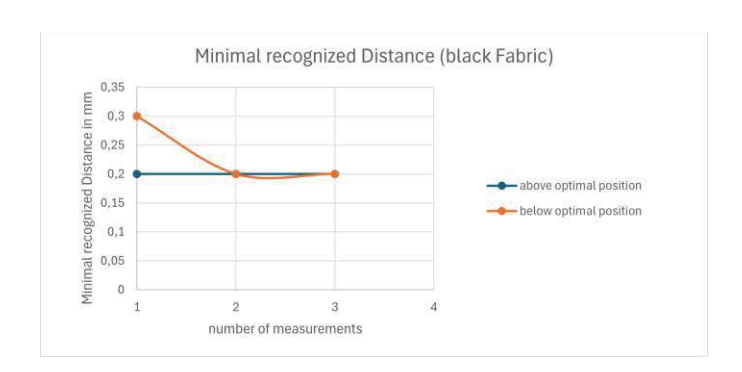


Figure 8.17

# 8.9 Z Scan on Gd Screen

The fluorescence screen was used as a sample and measurements were done in different z positions. A range of +/- 1.5mm around the optimal position was scanned in 0.5 mm steps.

Gross Counts of the L $\alpha$ ROI
254341
363887
370662
374473
351585
306180
243604

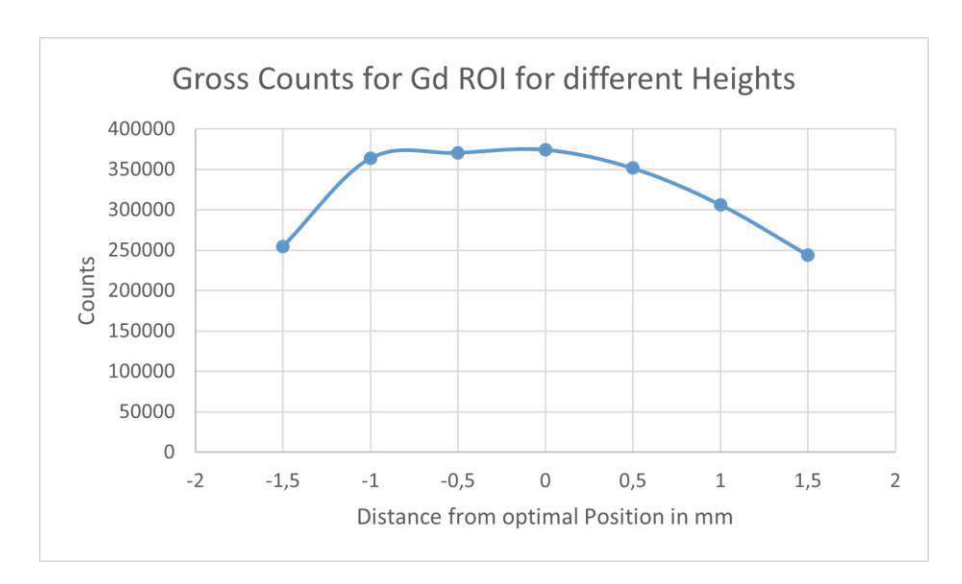


Figure 8.18: The counts for Gd plotted in a diagram. The stronger descent of the curve at positions above the optimal z coordinate is most likely caused by the restricted and angled view of the detector.

### 8.10 Reproducibility of Z Optimization

The correct position should be found by the AI in any case, despite varying initial distances between the sample and the measuring head. To verify this, a fluorescence screen containing Gd was used at a constant x/y coordinate, however, with different starting z coordinates.

- V=40kV
- I=50µA
- Measurement time per point: 100sec

The following table shows the acquired gross and net counts for Gd as well as the starting position relative to the optimal position.

Measurement	Gross Counts	Net Counts	Starting Position relative to Optimum
1	363966	352734	10 mm too high
2	367486	356434	5 mm too high
3	367487	354959	2 mm too low
4	365632	354544	3 mm too low
5	367891	354967	3 mm too high
6	368144	356768	4 mm too high
7	367433	354545	1 mm too low
8	367193	355241	1 mm too high
9	366490	353926	6 mm too high
10	365958	353538	7 mm too high

The measurements above show that the measured counts yield consistent results.

### 8.11 Characterization of Light Barrier

In order to change either the tube or the detector, the light barrier must be removed from the triangular frame. After placing the light barrier back on the frame, the distance, at which the light barrier triggers, should be within 0.5mm of the previous position. The light barrier has been removed from and placed on the frame ten times. Each time, starting from the optimal position (found using the AI) and adjusting the angle, the distance between the sample and the measuring head was decreased in 0.1mm steps until an obstruction has been detected.

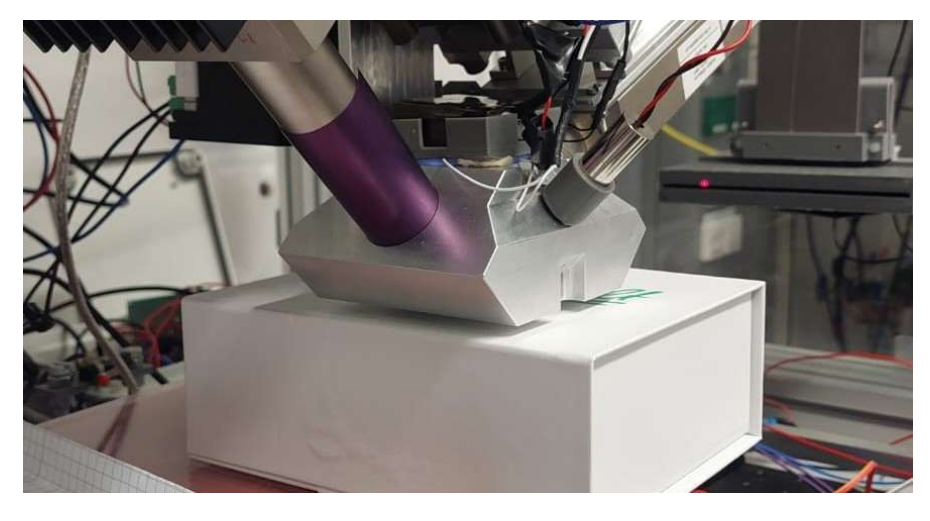


Figure 8.19: The setup for this measurement. The distance between the sample (white carton) and the measuring head is reduced until the laser beam is sufficiently obstructed.

The results of this measurement are listed below.

Number of Measurement	Distance from optimal Position in mm
1	2.6
2	2.5
3	2.3
4	2.5
5	2.7
6	2.7
7	2.6
8	2.5
9	2.7
10	2.7

These measurements show that the trigger occurs with a tolerance of 0.4mm.

# 8.12 Collision Prevention in y Direction with Light Barrier

The second function of the light barrier is to check if a collision between the sample and the measuring head is imminent when the sample stage moves along the y axis. For this test, a piece of carton was prepared as the colliding object and moved at an unsafe distance towards the measuring head (see figure 8.20). This test has been repeated five times for each side.

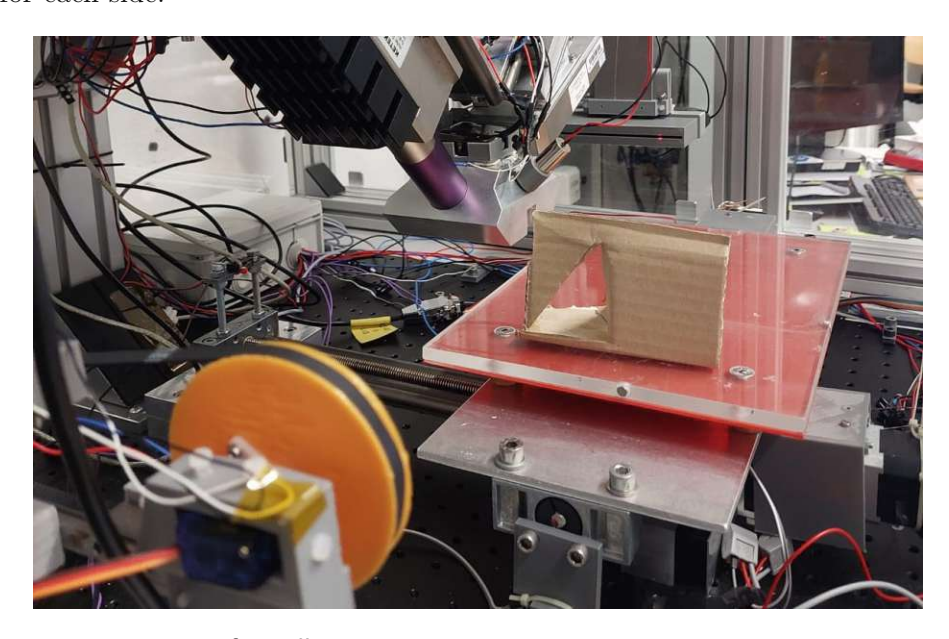


Figure 8.20: Test setup for collision prevention test.

the sample.

Each time, the setup was able to stop the motor movement roughly 6mm away from

#### 9 Conclusion and Outlook

#### 9.1 Conclusion

The findings of this thesis definitely highlight suitable use cases for the MAXI. Firstly, the new design allows for better repeatability, of measurements, since the new mechanical parts strongly reduce uncertainties.

Secondly, the z position optimization allows for a wider range of samples that can be scanned automatically. This saves a great amount of time for area scans, especially, since the manual adjustment at a single position takes noticeably longer.

Furthermore, due to the spot size, the MAXI serves as an excellent option to area scan many pictures or other artifacts with features bigger than a mm.

#### 9.2 Outlook

Collimators with a diameter of less than 1mm will be tested in the future to find a compromise between intensity and resolution. Another possible future improvement could focus on a more compact electronic design that makes it easier to transport the whole setup.

As is to be expected from the inclusion of new features, specifically the safety features, the overall measurement can be slowed down, and thus, could be subject to further optimizations in the future. Another consideration for future work, would be a new pair of motors for the x/y stage. The current motors can no longer be purchased, thus making it difficult to find replacements.

# 10 Appendix

# 10.1 Programs

```
# -*- coding: utf-8 -*-
 Created on Tue Oct 1 07:49:05 2024
 @author: Kraus P.
import numpy as np
import math
import matplotlib.pyplot as plt
import matplotlib.pyplot as plt_ang
y=np.zeros(30001)
k_arr=np.zeros(30001)
x_max=30
x_min=0.001
dx=0.001
n1=1
n2=1.8
alpha=0
x=np.linspace(x_min,x_max,30001)
arr_k=np.zeros(50)
y0=35
y[0]=y0
deg=0.00001
j=0
for i in range(0,30000):
n=0
         n=0
k=y[i]/x[i]
k_b=k+0.0001
           while (k_b>=k and n<100):
    beta=math.asin((n1/n2)*math.sin(alpha+n*deg))
    k_b=math.tan(3.141592/2+beta-alpha-n*deg)</pre>
         alpha=alpha+n*deg
y[i+1]=y[i]-math.tan(alpha)*dx
k_arr[i]=(alpha)*180/3.14159
# if i%2000==0:
# arr_k[j]=math.tan(3.14159
# arr_k[j]=math.tan(3.14159/2-alpha)
# j=j+1
plt.axis('equal')
plt.axis([0, 30, 0, 60])
 plt.plot(x,y)
plt.show()
plt_ang.plot(x,k_arr)
 plt_ang.show()
```

Figure 10.1: Code for determining the shape of the focusing lens.

```
#include <Servo.h>
Servo myservo;
int servopin = 7;
          int y_min = 8;
int y_max = 9;
//int z_stop = 10;
int stop;
int aPin=0;
int zecan(int min_laser_pos,int max_laser_pos,int aPin);
int set_y(int y_stop,int aPin, int y_pos);
void setup() {
    // put your setup code here, to run once:
    myservo.attach(servopin);
    myservo.write(90); // set servo to mid-point
pinMode(y_min, OUTPUT);
pinMode(y_max, OUTPUT);
//pinMode(Cpin, INPUT);
               Serial.begin(9600);
Serial.setTimeout(10);
              \label{eq:myservo.write(4); // set servo to end position delay(1000); stop=0;} $$
          void loop() {
   // put your main code here, to run repeatedly:
               //myservo.write(4); // set servo to mid-point
              int i;
int sel;
int firstrun;
int end=1;
//int stop=1;
int min_laser_pos=2;
int max_laser_pos=180;
              String str ="";
while (Serial.available ()==0){}
/*if (firstrun!=1)
/*/
/*if (firstrun!=1)
              stop=0;
               firstrun=1;*/
               if (Serial.available() > 0) {//wait for command
   String str = Serial.readString();
   str.trim();
   Serial.println(str);
             //sel=str;
Serial.println(sel);
if((str.indexOf("zscan") > 0) )
                   stop=zscan(min_laser_pos,max_laser_pos,aPin);
                else if((str.indexOf("status") > 0))
                   if(stop==1)
                    {
Serial.println("stop");
```

Figure 10.2: Code for controlling the light barrier. Page 1/3.

```
70
71
72
73
74
75
76
77
78
80
81
82
83
84
85
86
87
88
89
90
91
92
93
                     Serial.println("ok");
              }
else if((str.indexOf("set_ymin") > 0))
                 stop=set_y(y_min, aPin, min_laser_pos);
               else if((str.indexOf("set_ymax") > 0))
                 stop=set_y(y_max, aPin, max_laser_pos);
              else if((str.indexOf("reset") > 0))
                 stop=0;
digitalWrite(y_min, LOW);
digitalWrite(y_max, LOW);
           int zscan(int min laser_pos,int max_laser_pos,int aPin){    //moves laser between min and max position and sets variable "stop" to 1 if obstruction has been detected int i,an_val, end=0, stop=0;
             Serial.print("Start Intervall");
Serial.print('\n');
for(i=min_laser_pos;i<=max_laser_pos;i=i+2);</pre>
             {
  myservo.write(i);
delay(25);
an_val=analogRead(aPin);
Serial.print(analogRead(an_val));
Serial.print('\n');
             if(an_val>200)
                 Serial.print("STOP");
Serial.print('\n');
//digitalWrite(z_stop,1);
end=1;
                 stop=1;
              }
if(Serial.available()>0)
.
              for(i=max_laser_pos;i<=min_laser_pos;i=i-2)</pre>
                 myservo.write(i);
            myservo.writering
delay(20);
an_val=analogRead(aPin);
Serial.print(analogRead(an_val));
Serial.print('\n');
if(Serial.available()>0);
              if(an_val>200)
                 Serial.print("STOP");
Serial.print('\n');
//digitalWrite(z_stop,1);
```

Figure 10.3: Code for controlling the light barrier. Page 2/3.

```
set_y(int y_stop,int aPin, int y_pos)//moves laser to one of the end positions, and cks for obstruction until one is found or other command is received
int end=0;
int an val;
int stop=0;
myservo.write(y_pos);
delay(200);
do(
if(Serial.available()>0)
     }
an_val=analogRead(aPin);
Serial.print(analogRead(an_val));
Serial.print(analogRead(an_val));
Serial.print('\n');
if(an_val>200);
           Serial.print("STOP");
Serial.print('\n');
digitalWrite(y_stop,1);
delay(500);
digitalWrite(y_stop,0);
end=1;
stop=1;
              }while(end==0);
```

Figure 10.4: Code for controlling the light barrier. Page 3/3.

#### 10.2 Drawings

In this section, the drawings, of all parts that have been manufactured during this thesis, are listed. The drawings include a small list of information regarding the material and threads.

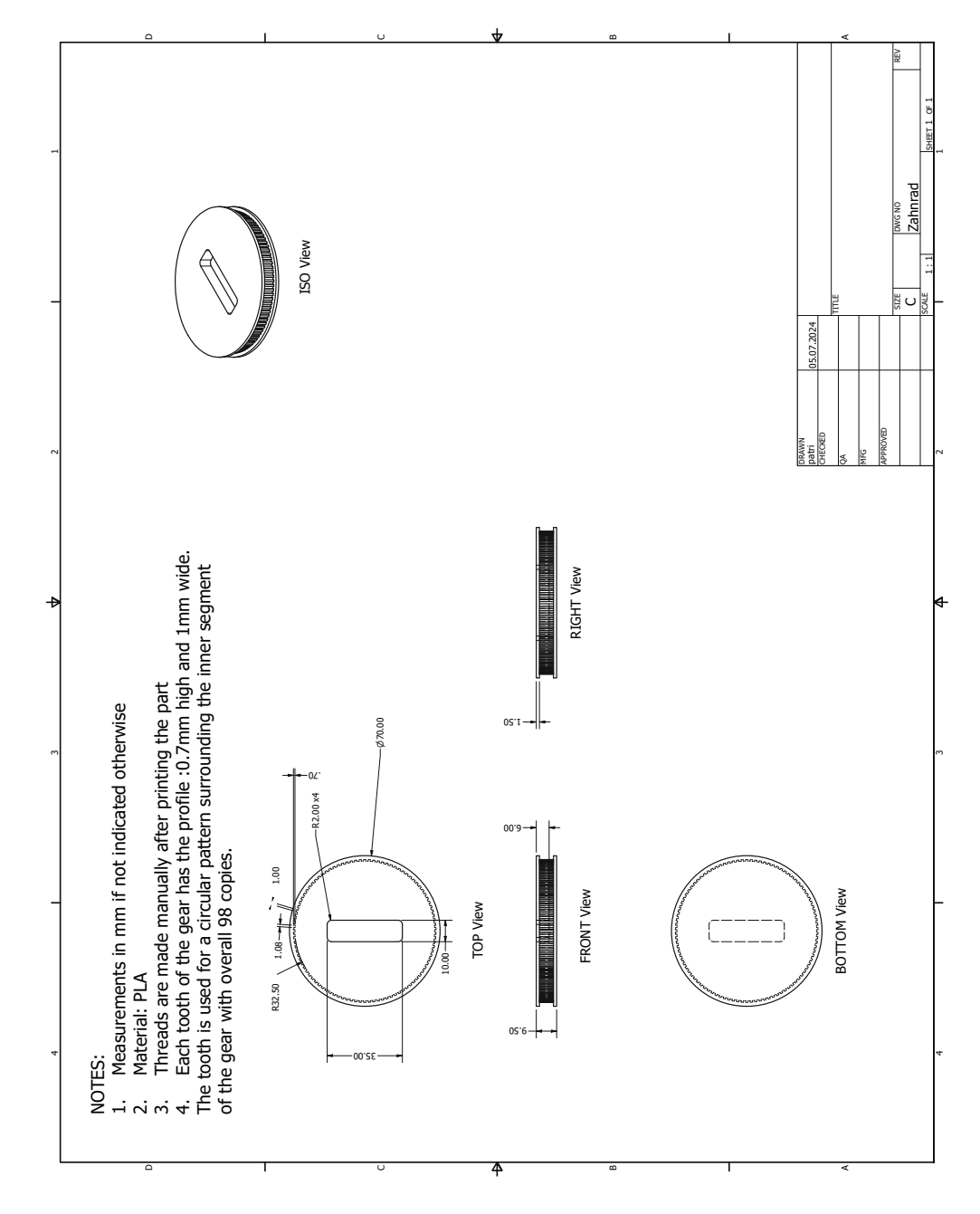


Figure 10.6

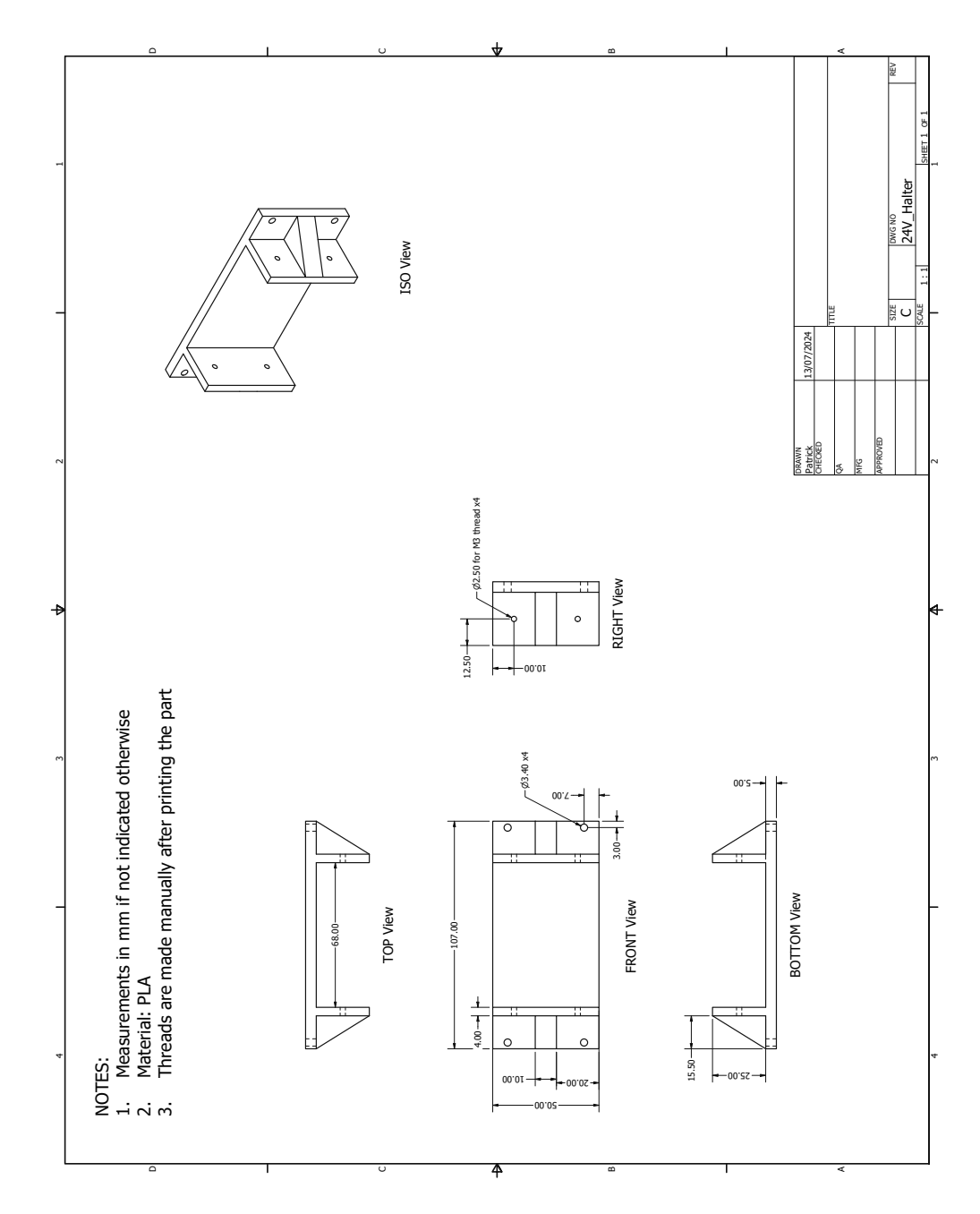


Figure 10.7

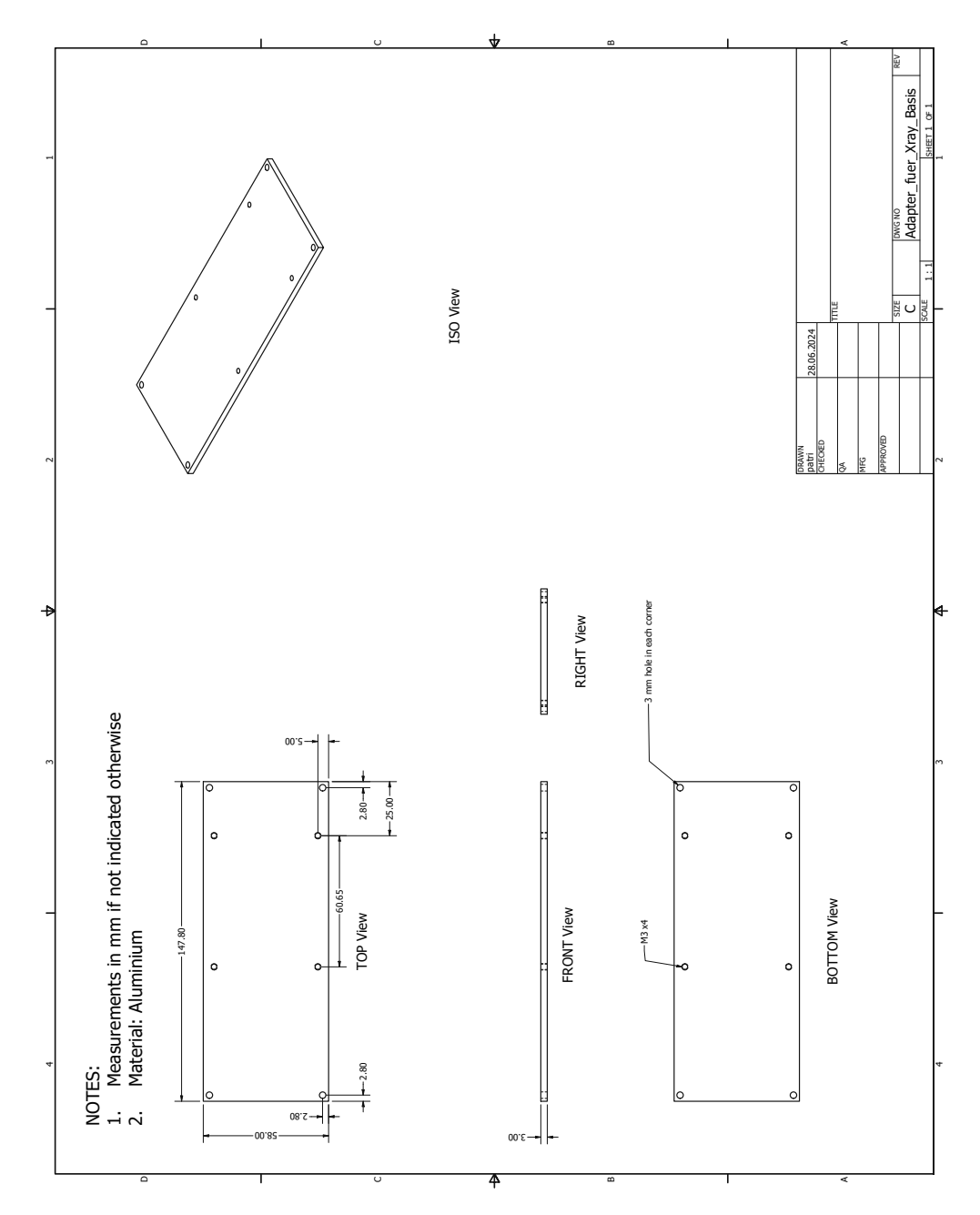


Figure 10.8

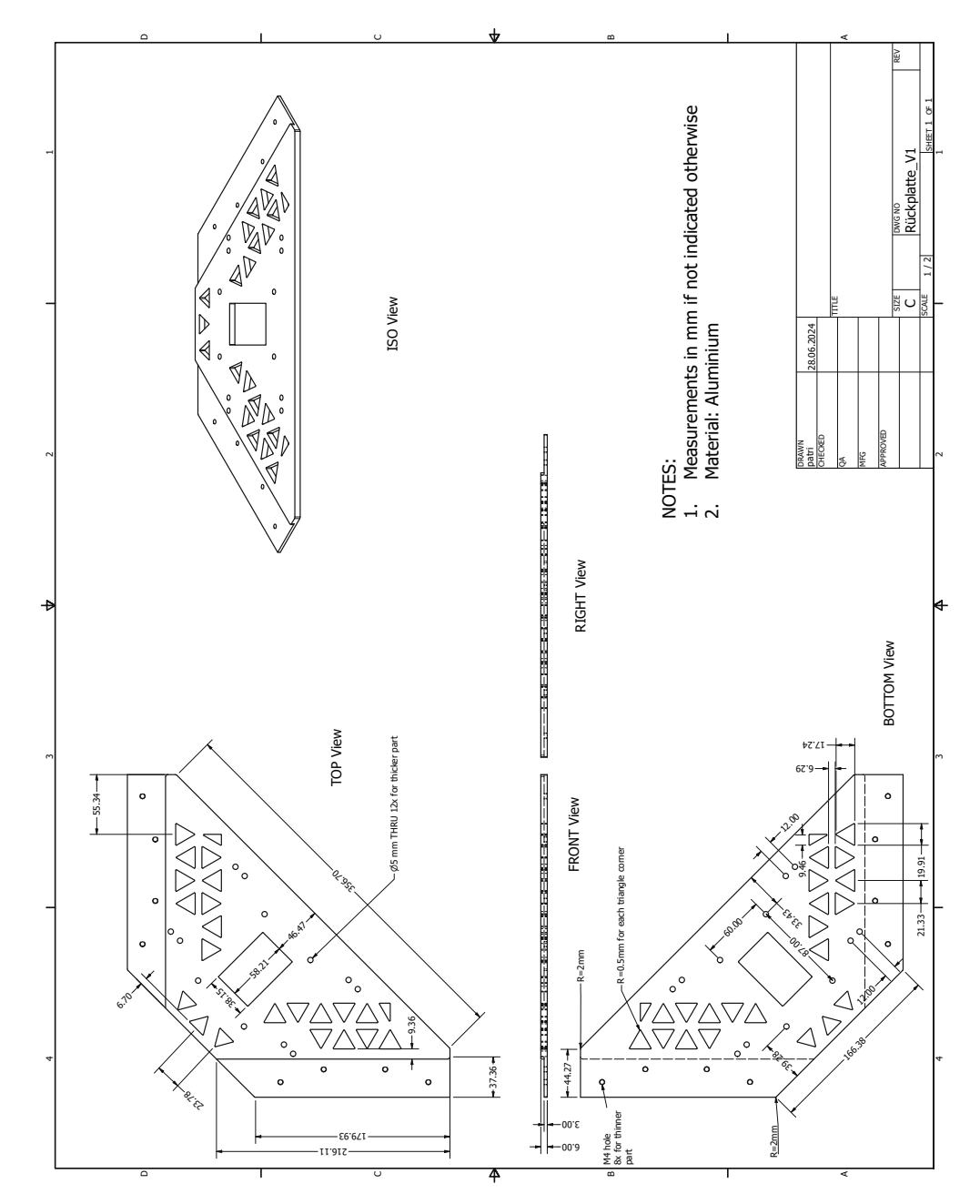


Figure 10.9

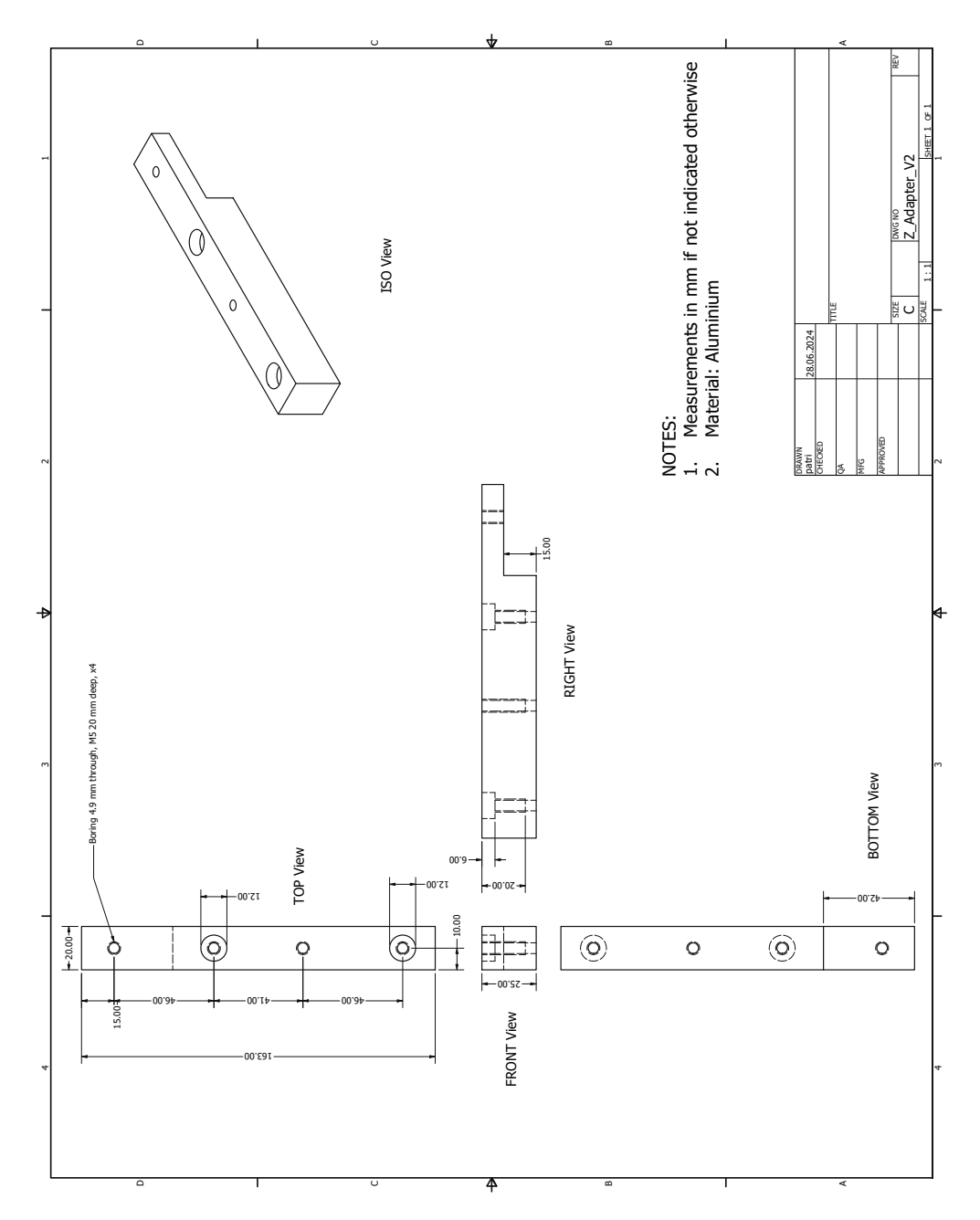


Figure 10.10

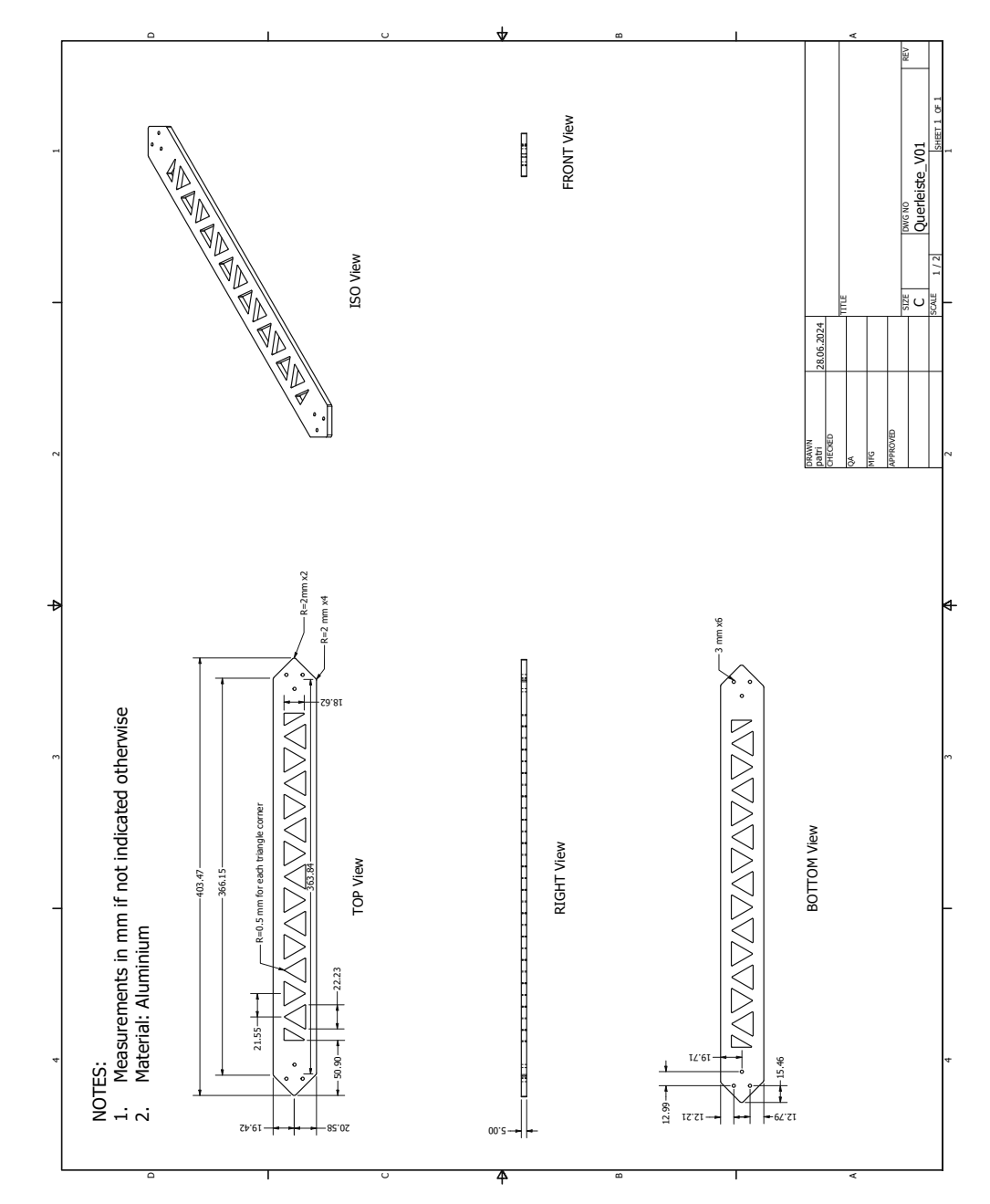


Figure 10.11

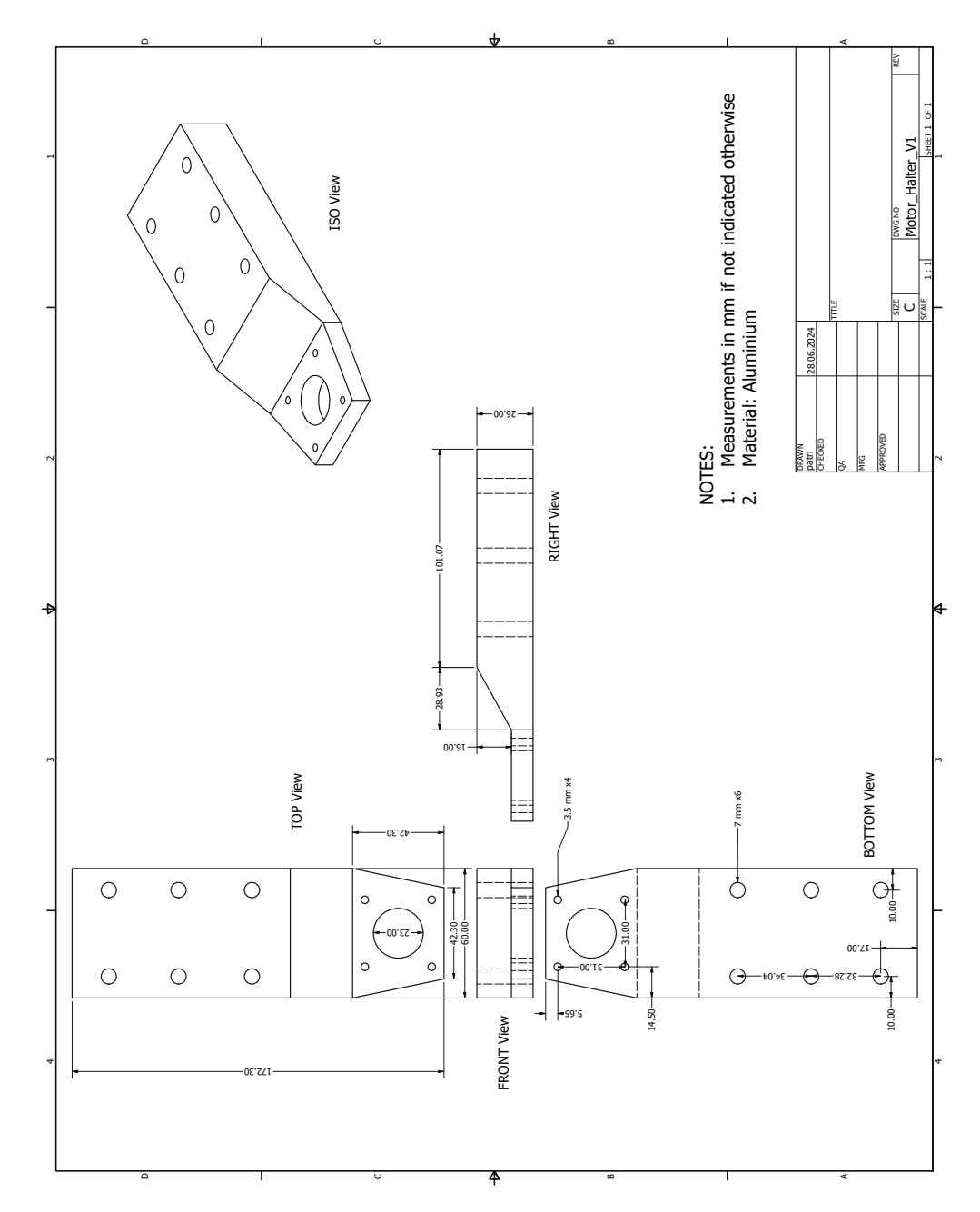


Figure 10.12

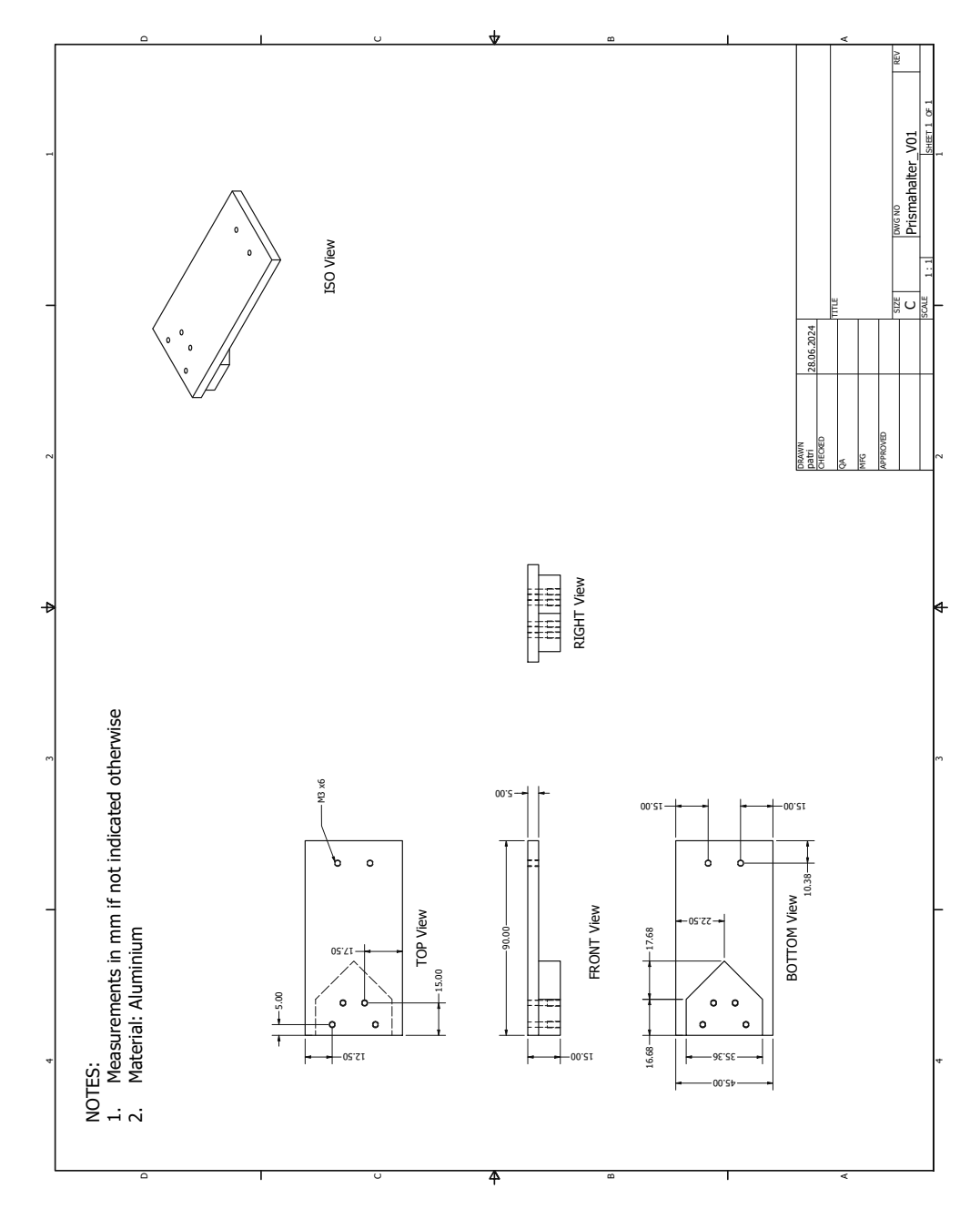


Figure 10.13

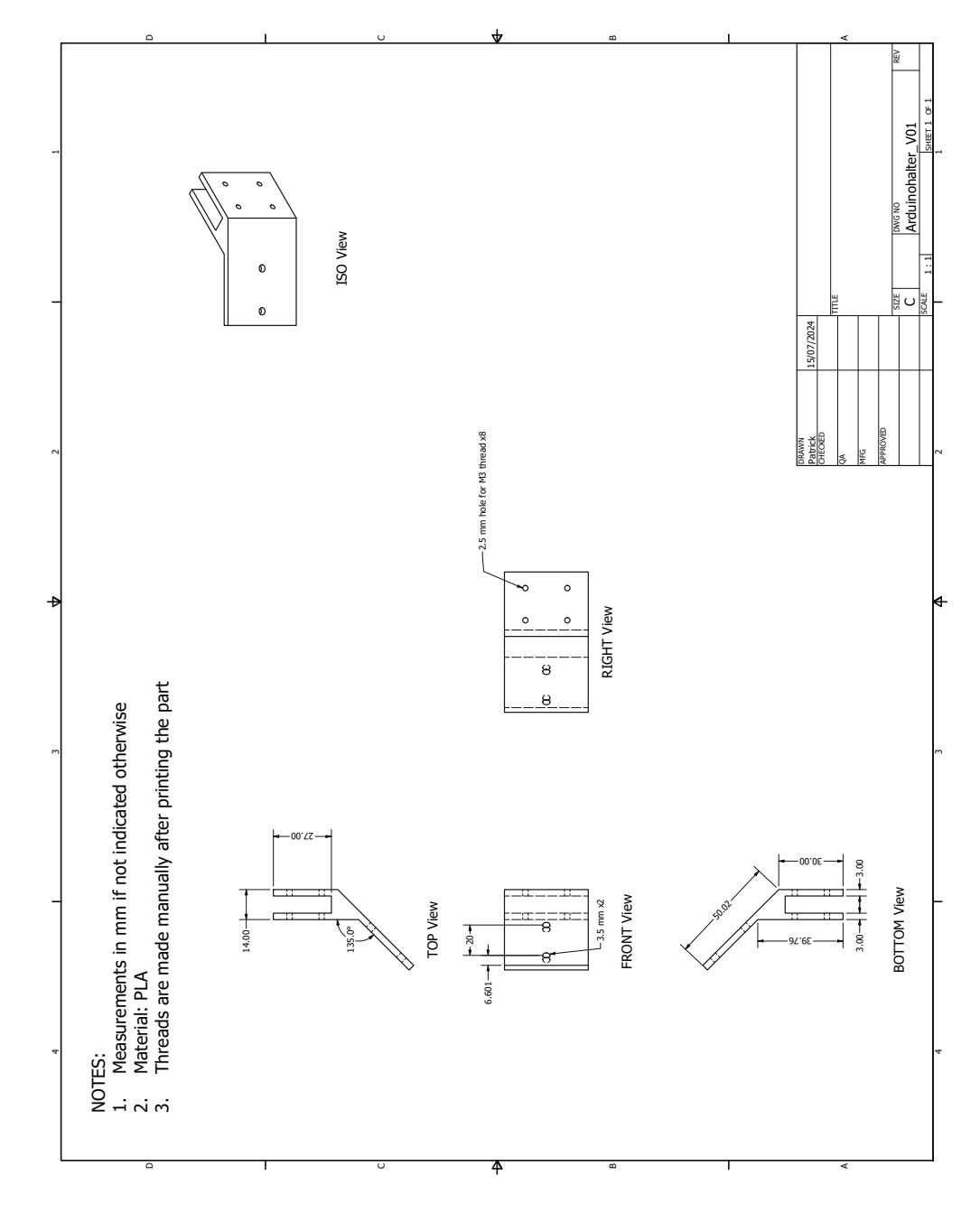


Figure 10.14

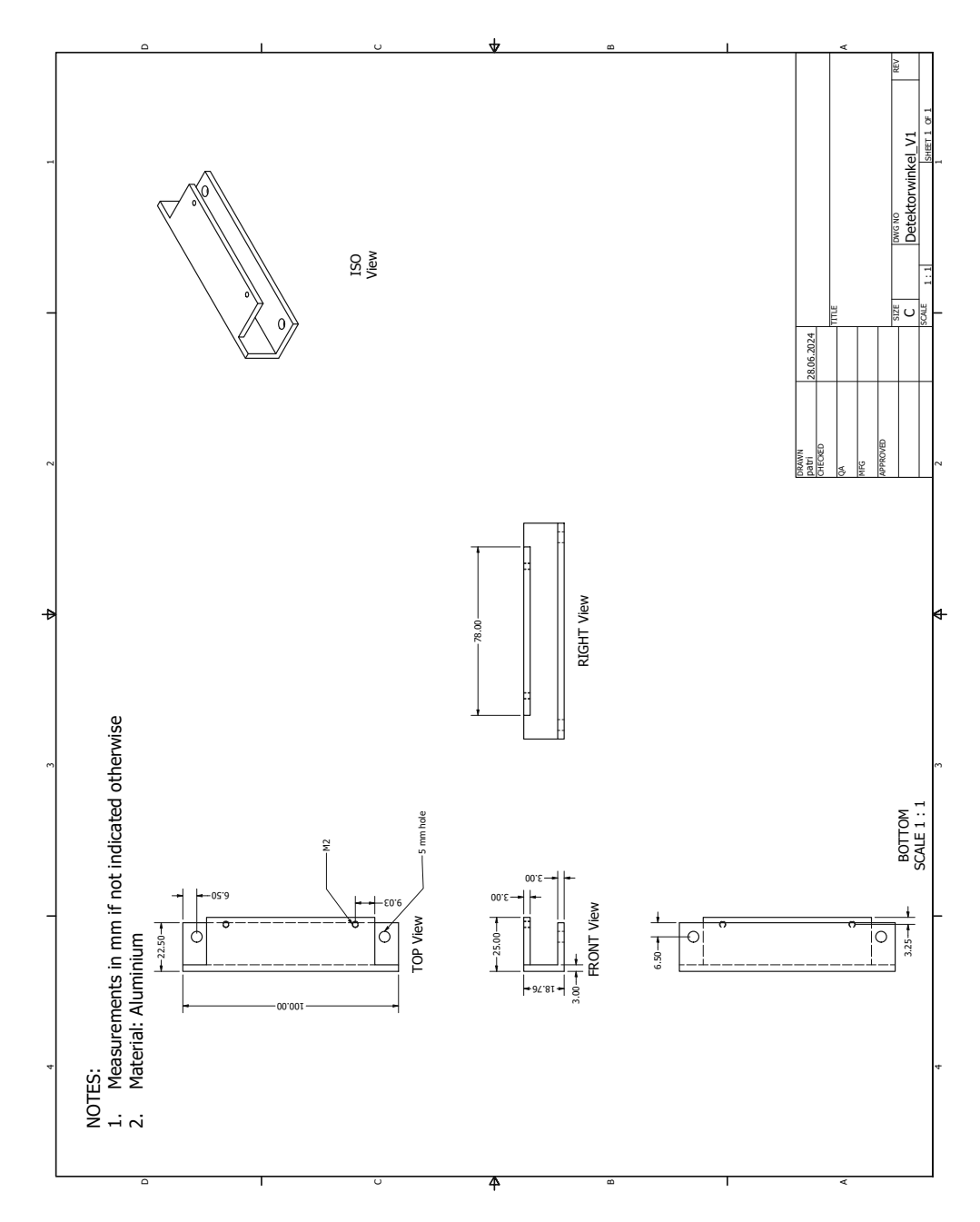


Figure 10.15

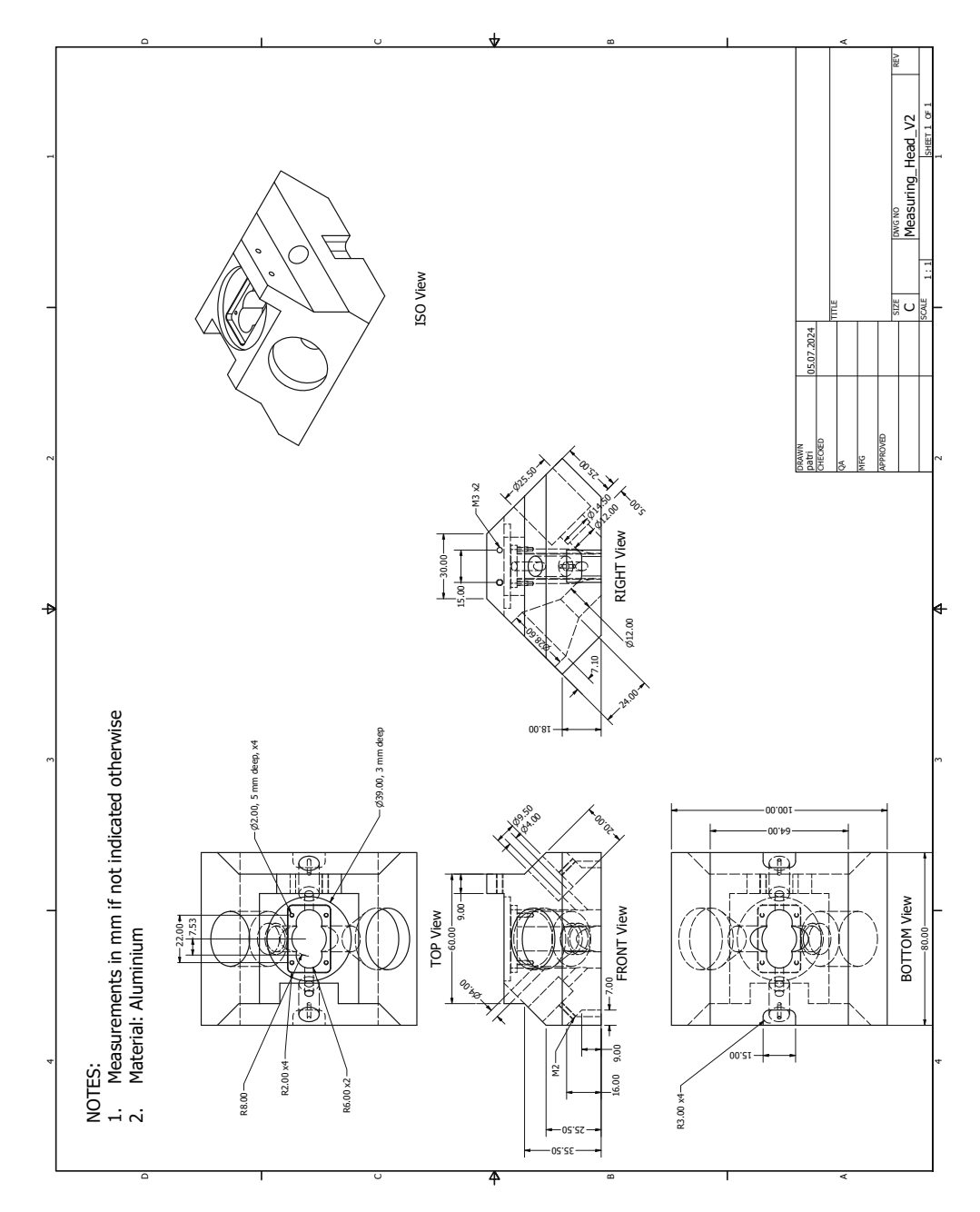


Figure 10.16

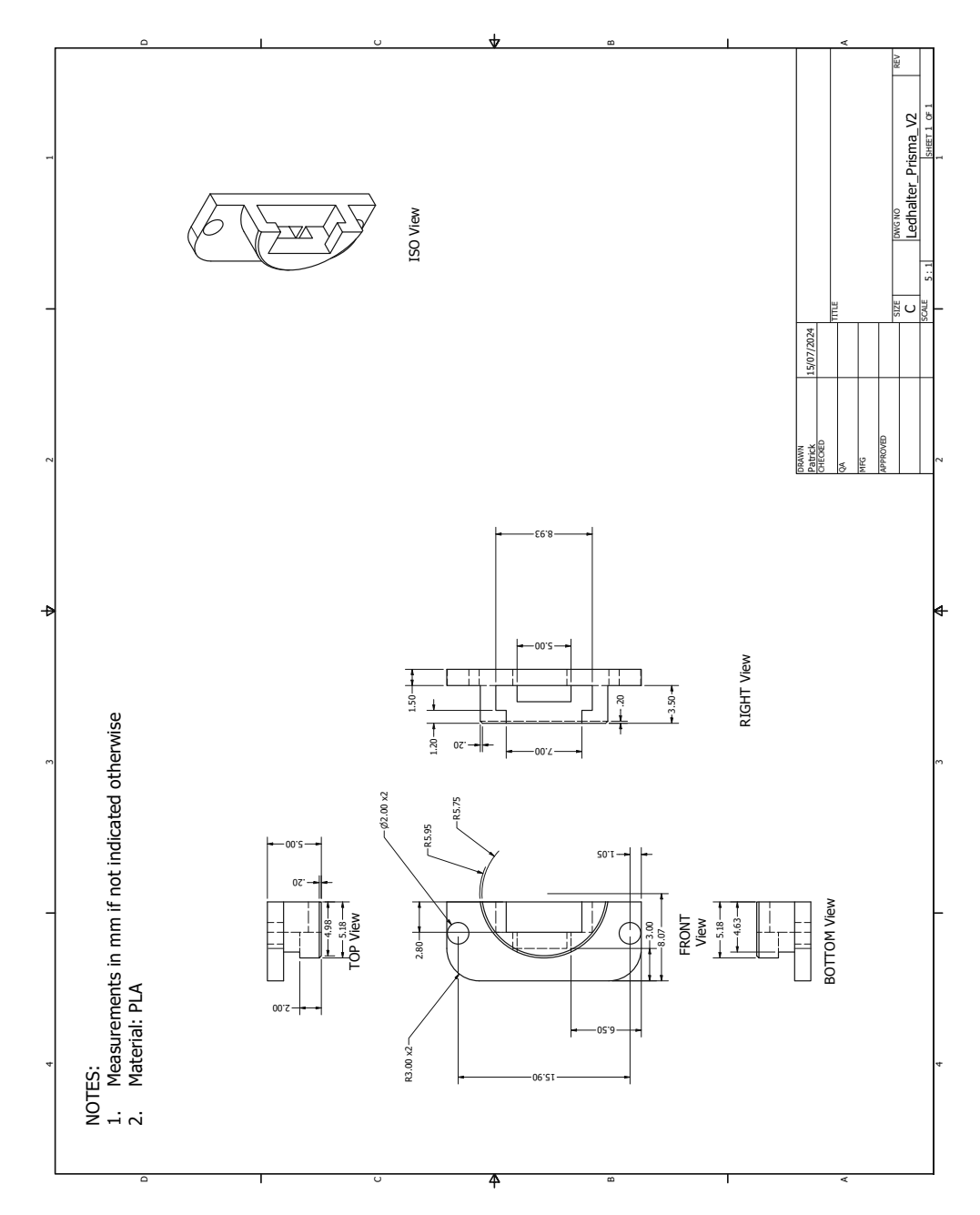


Figure 10.17

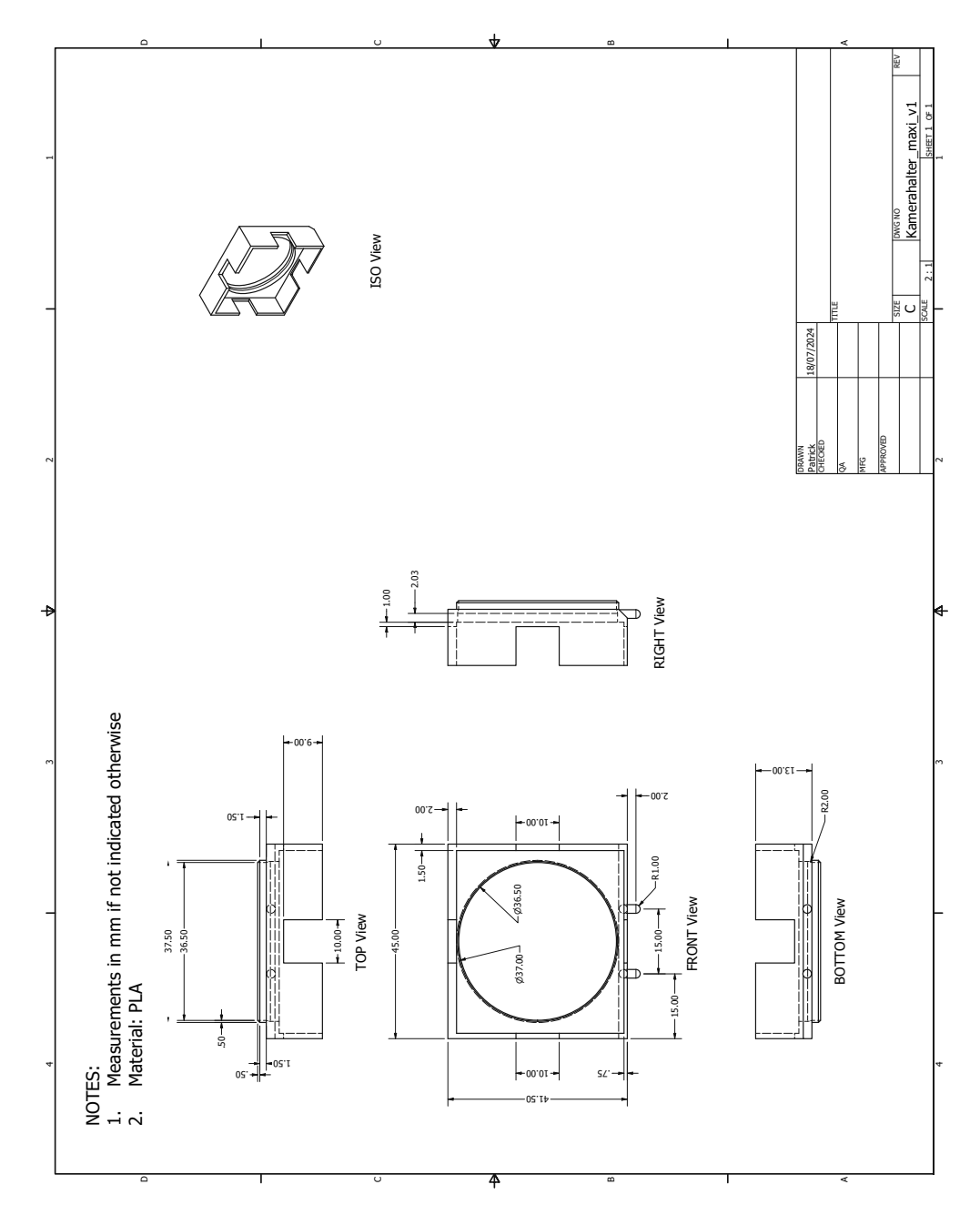


Figure 10.18

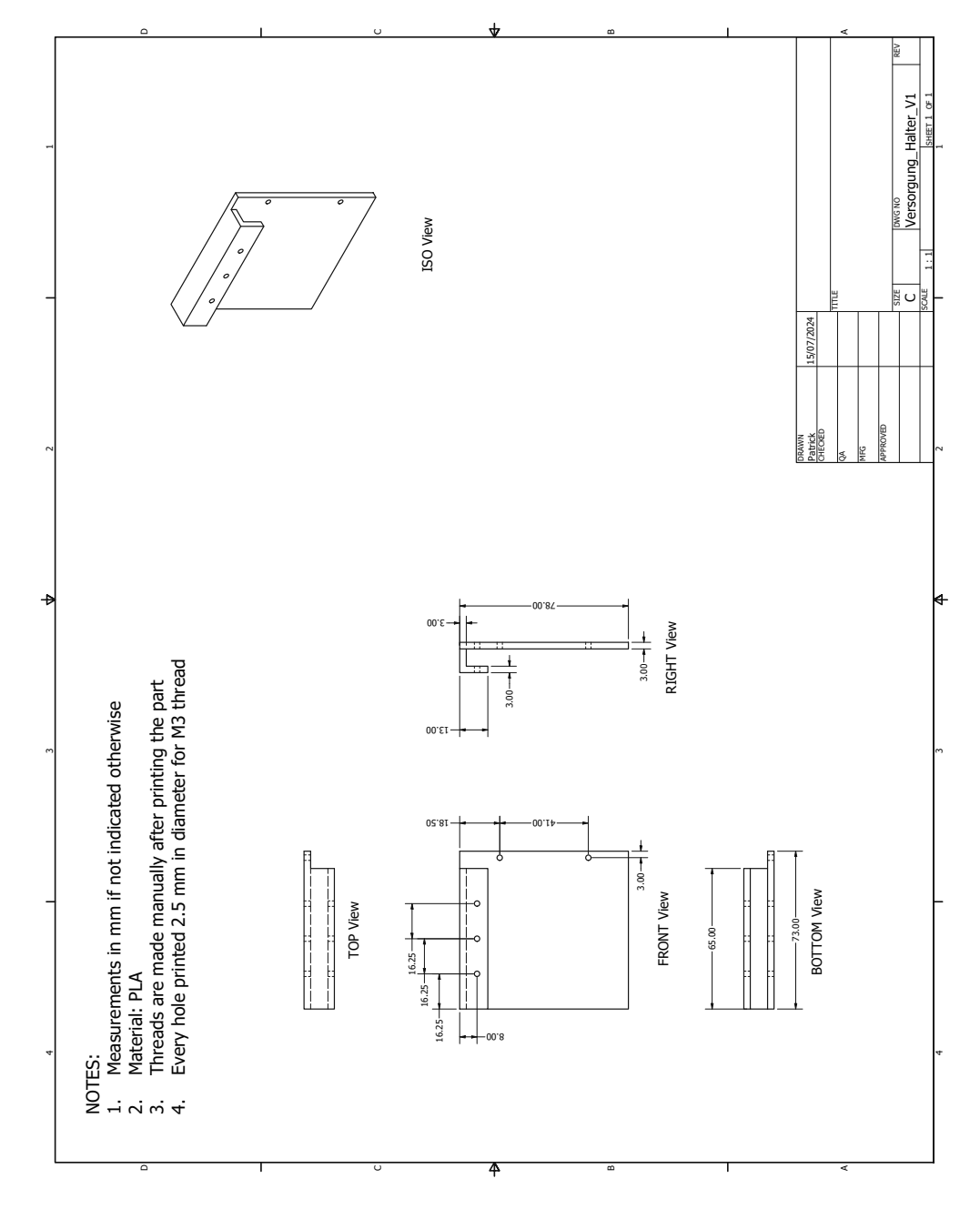


Figure 10.19

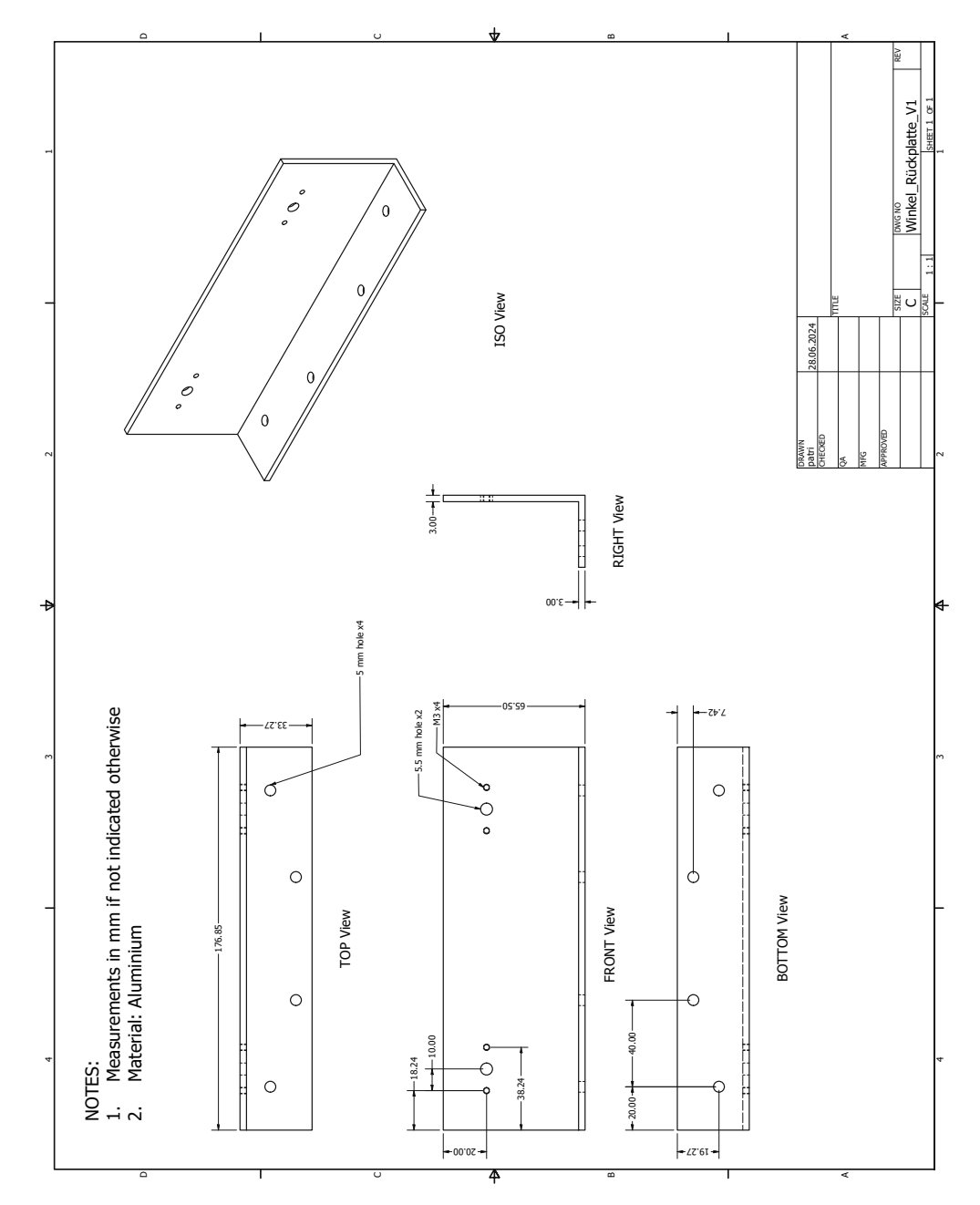


Figure 10.20

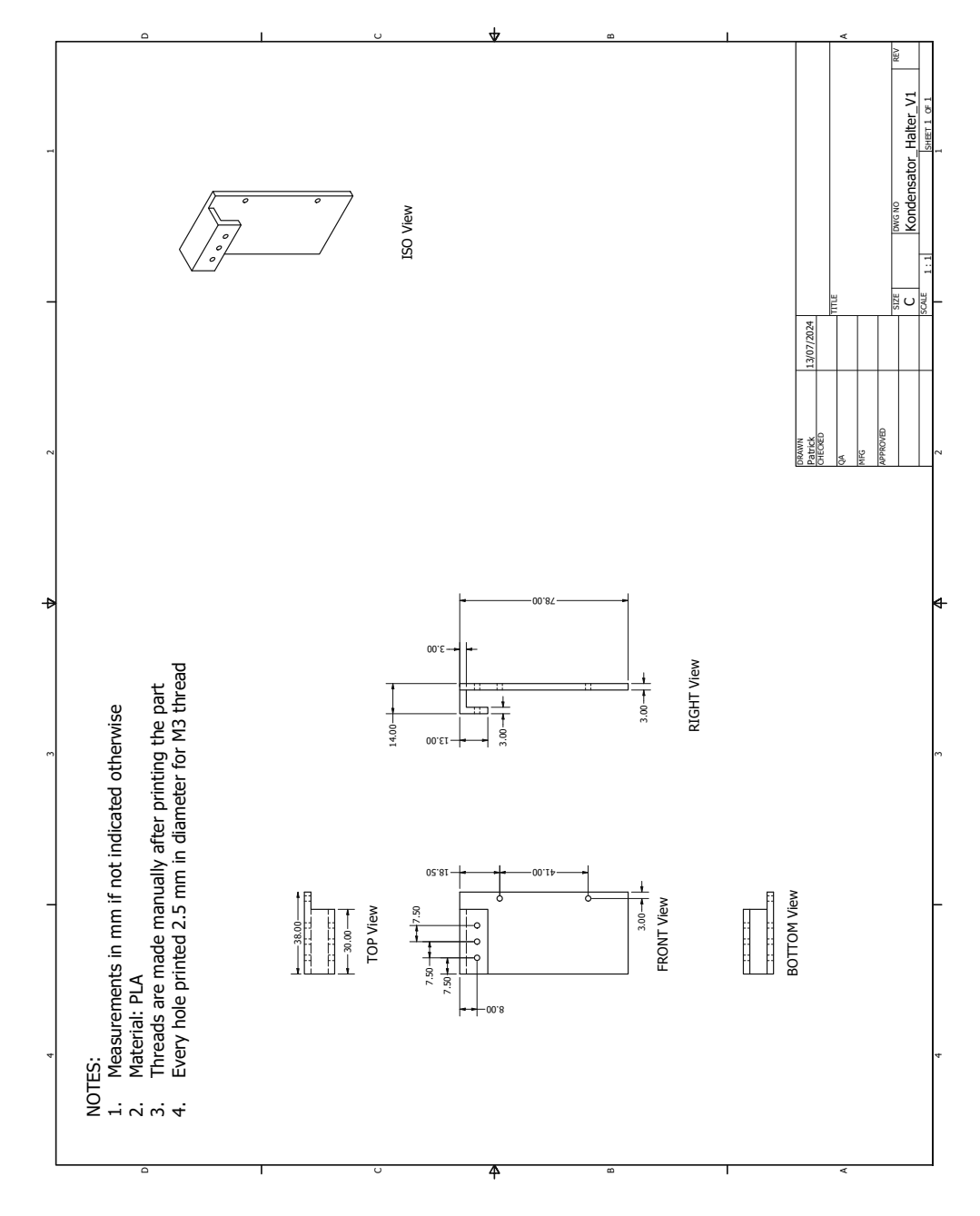


Figure 10.21

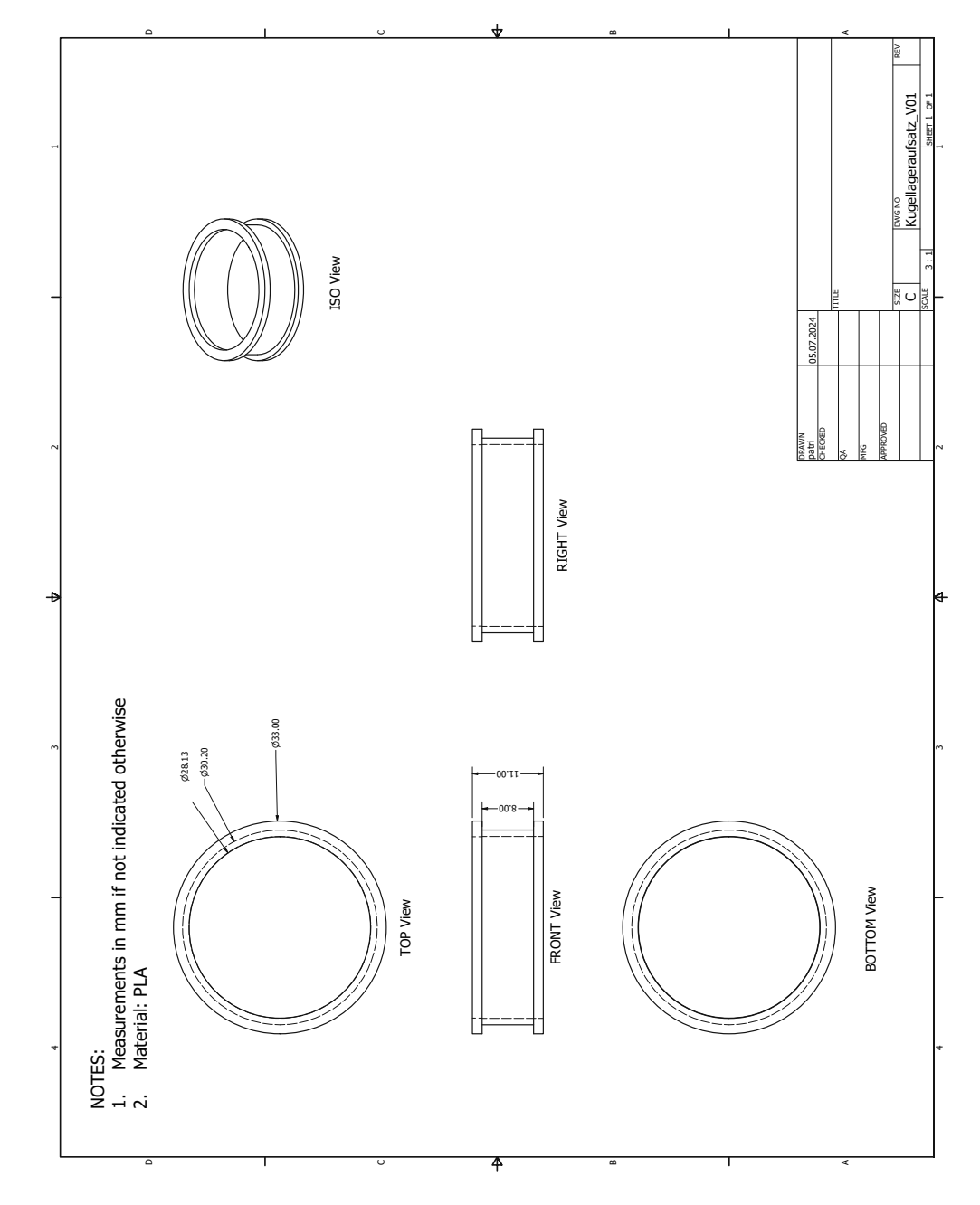


Figure 10.22

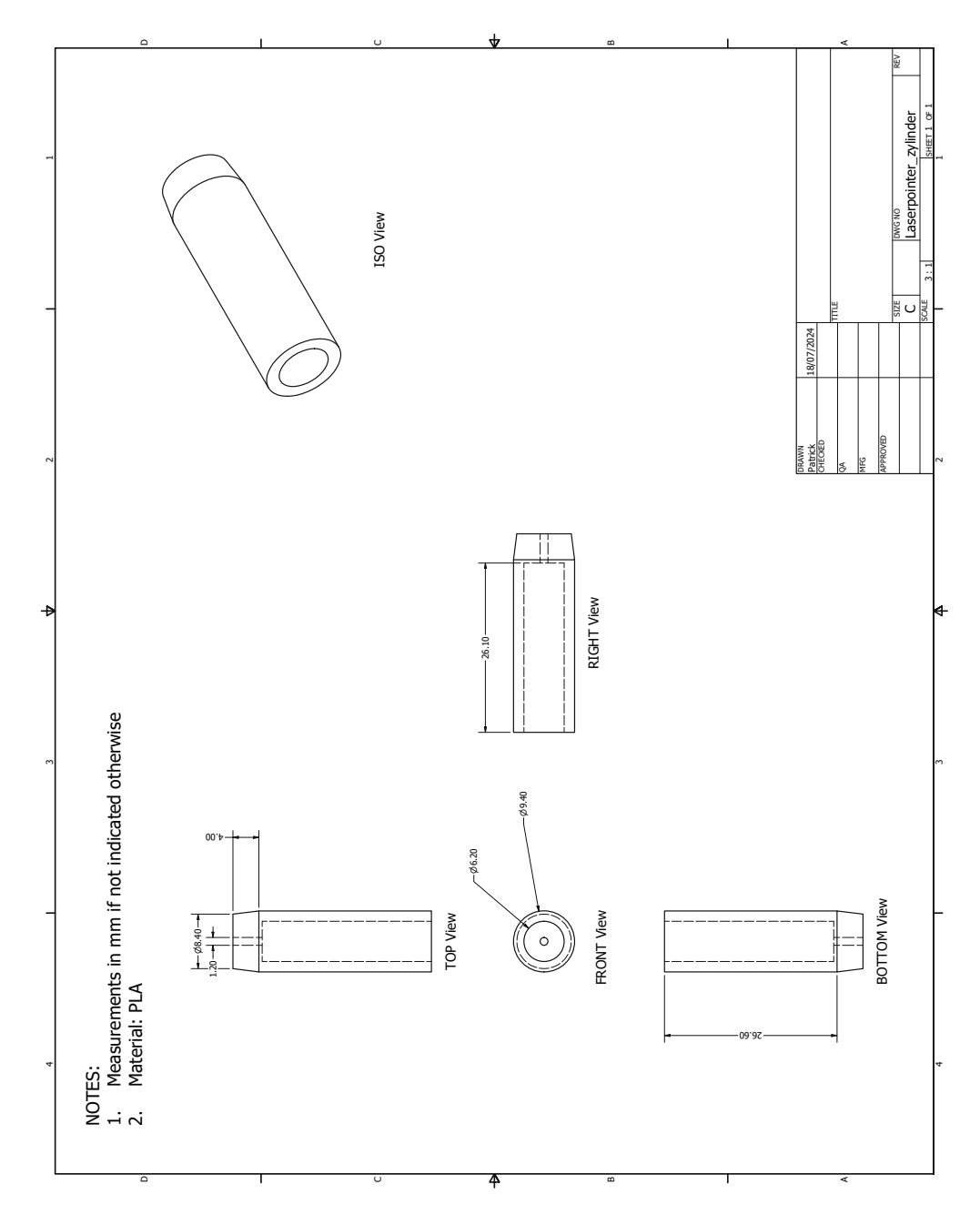


Figure 10.23

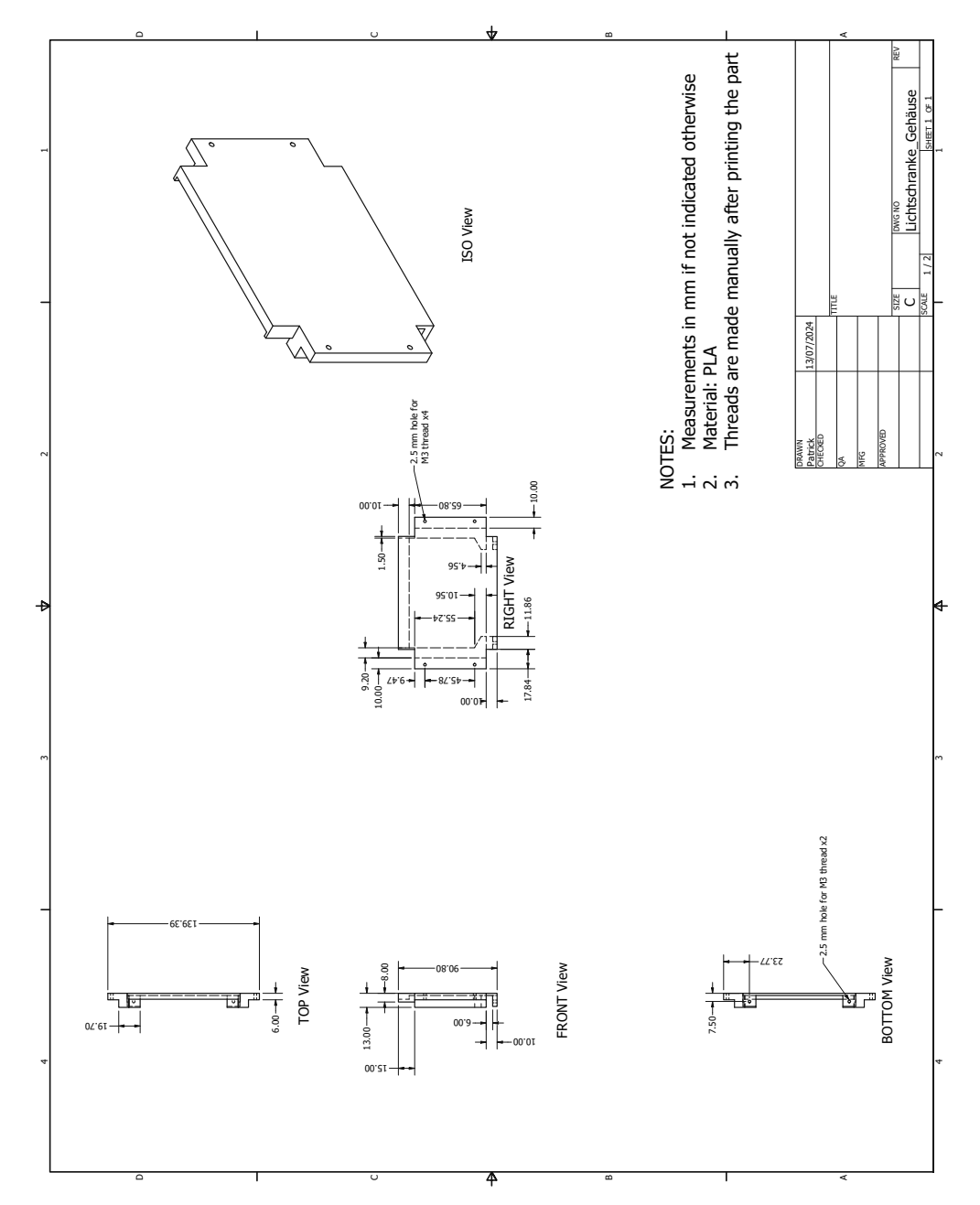


Figure 10.24

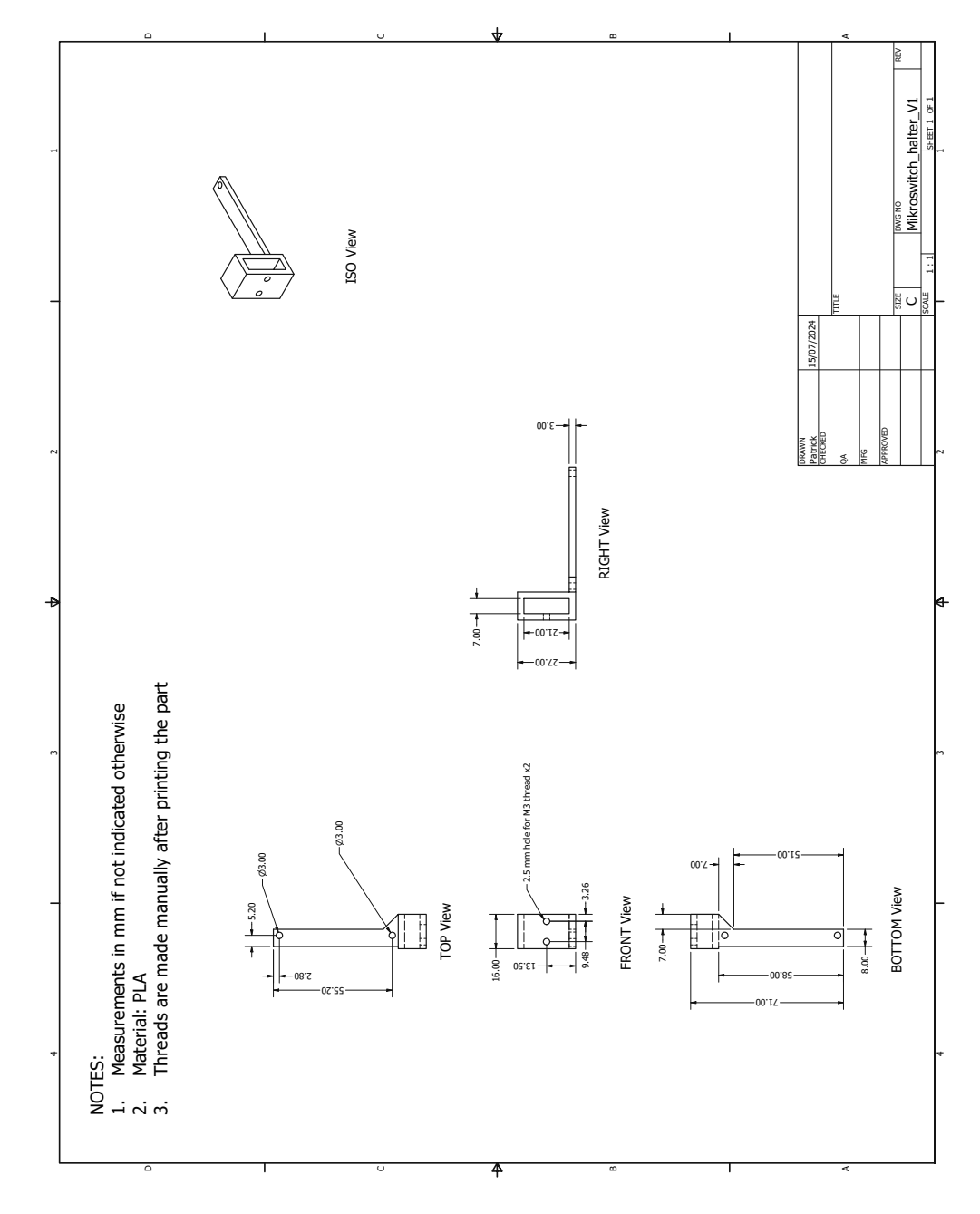


Figure 10.25

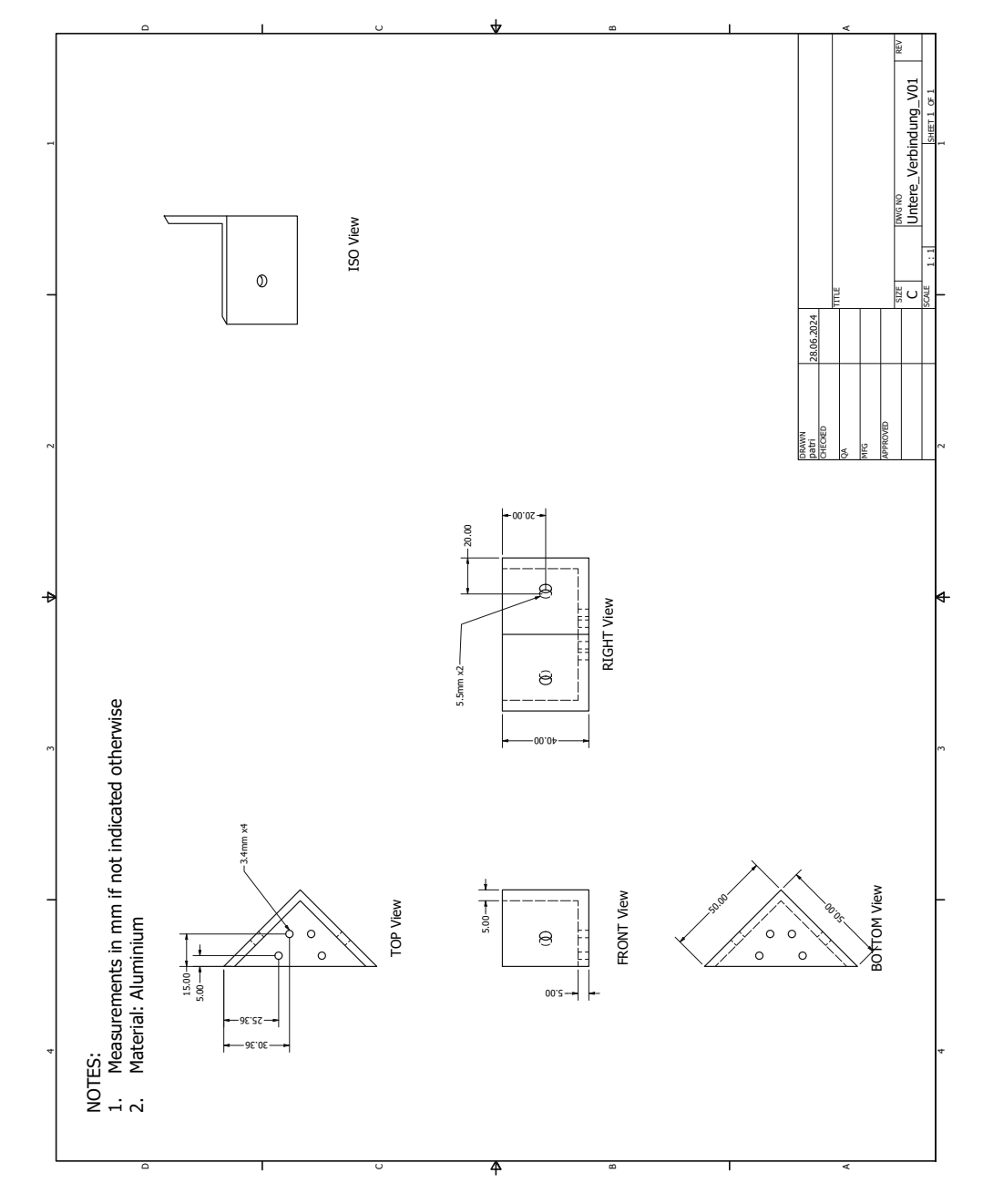


Figure 10.26

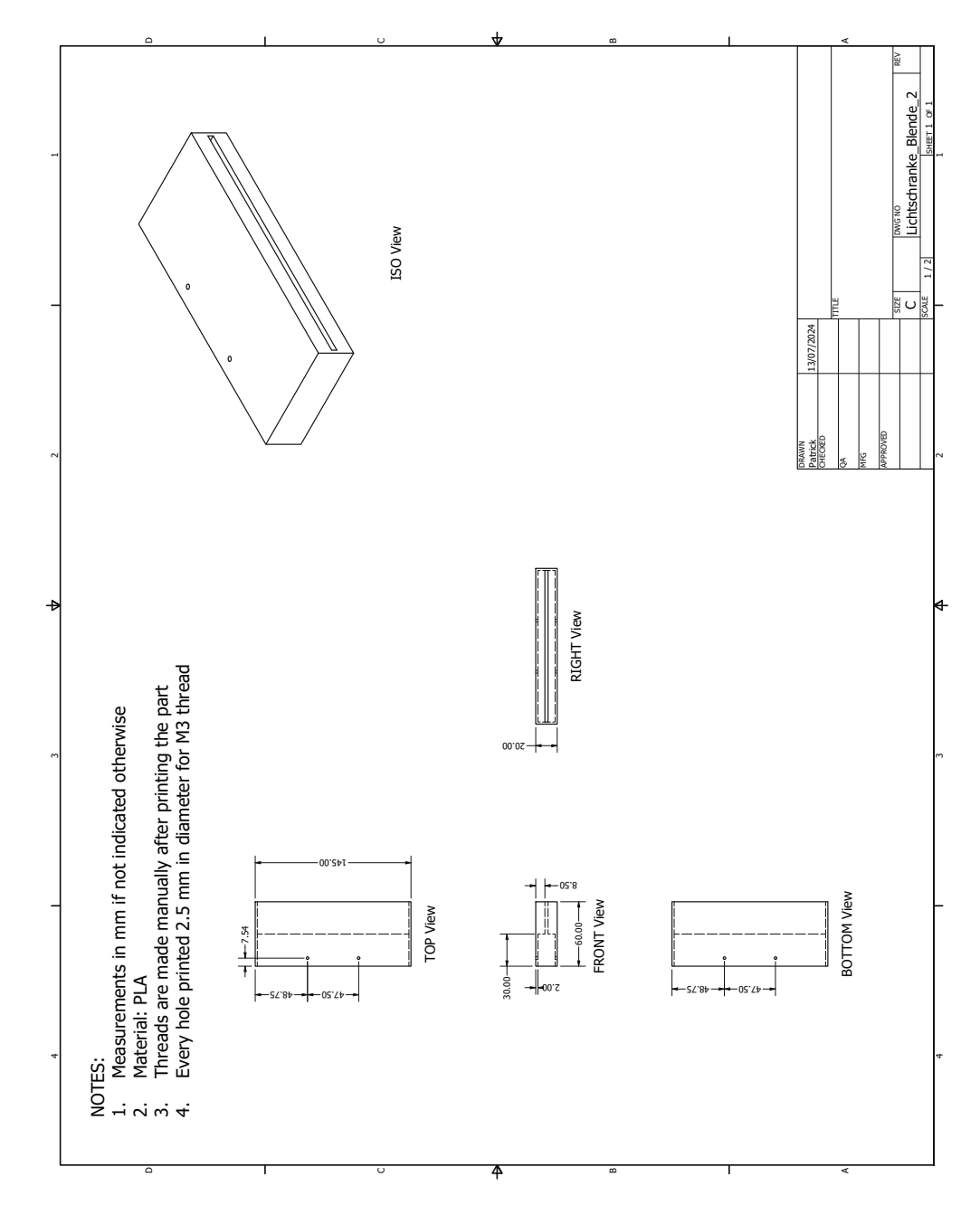


Figure 10.27

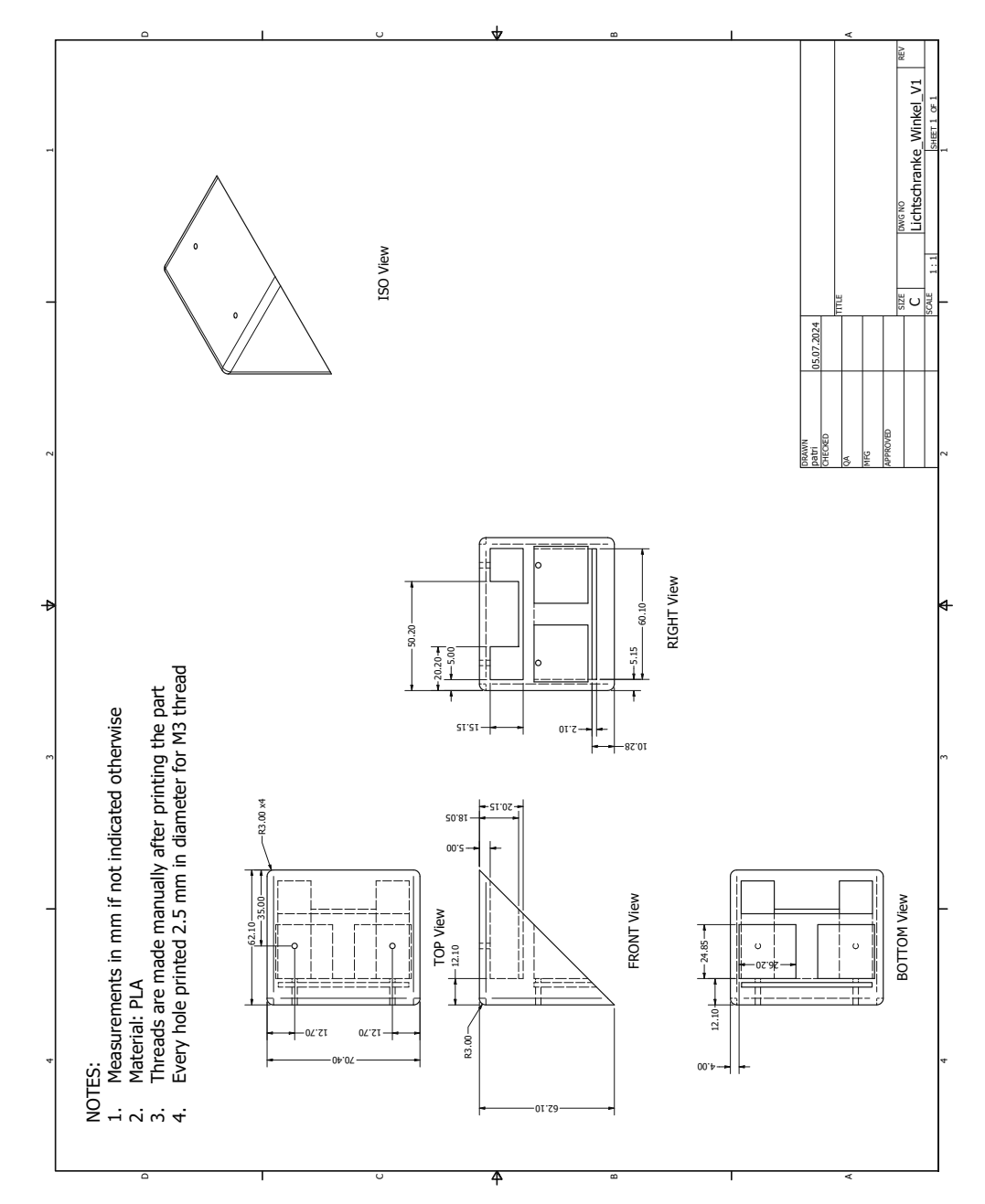


Figure 10.28

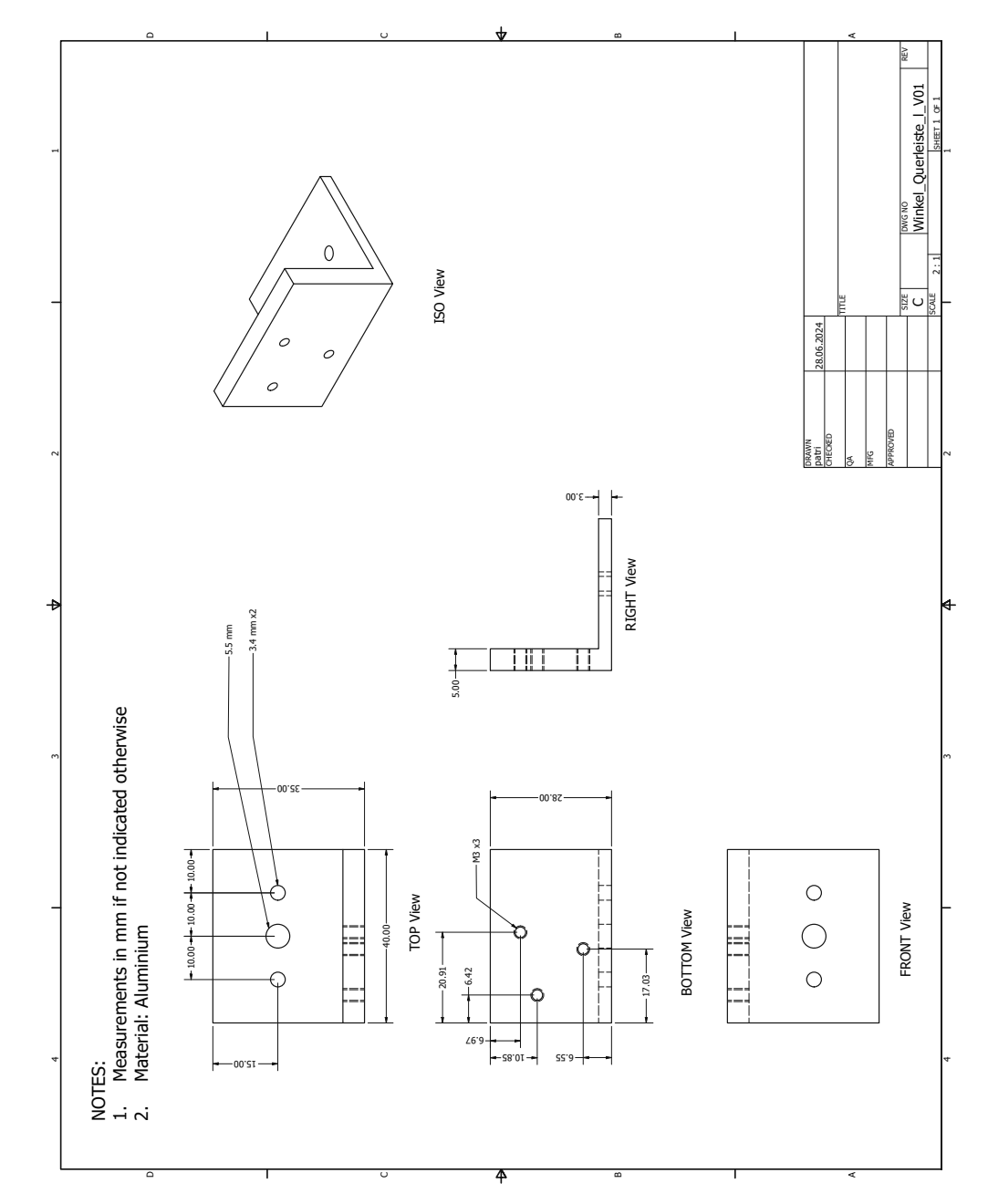


Figure 10.29

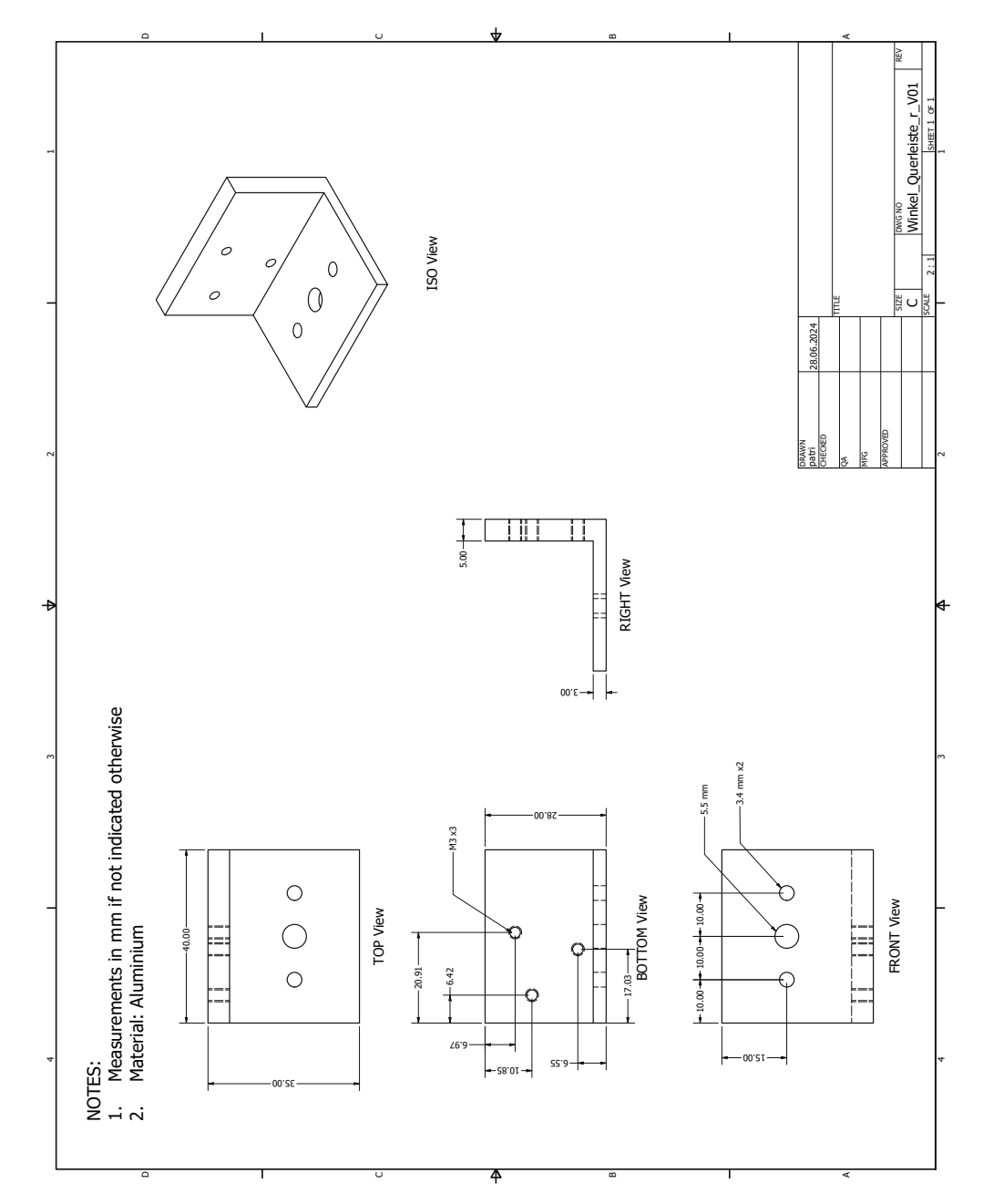


Figure 10.30

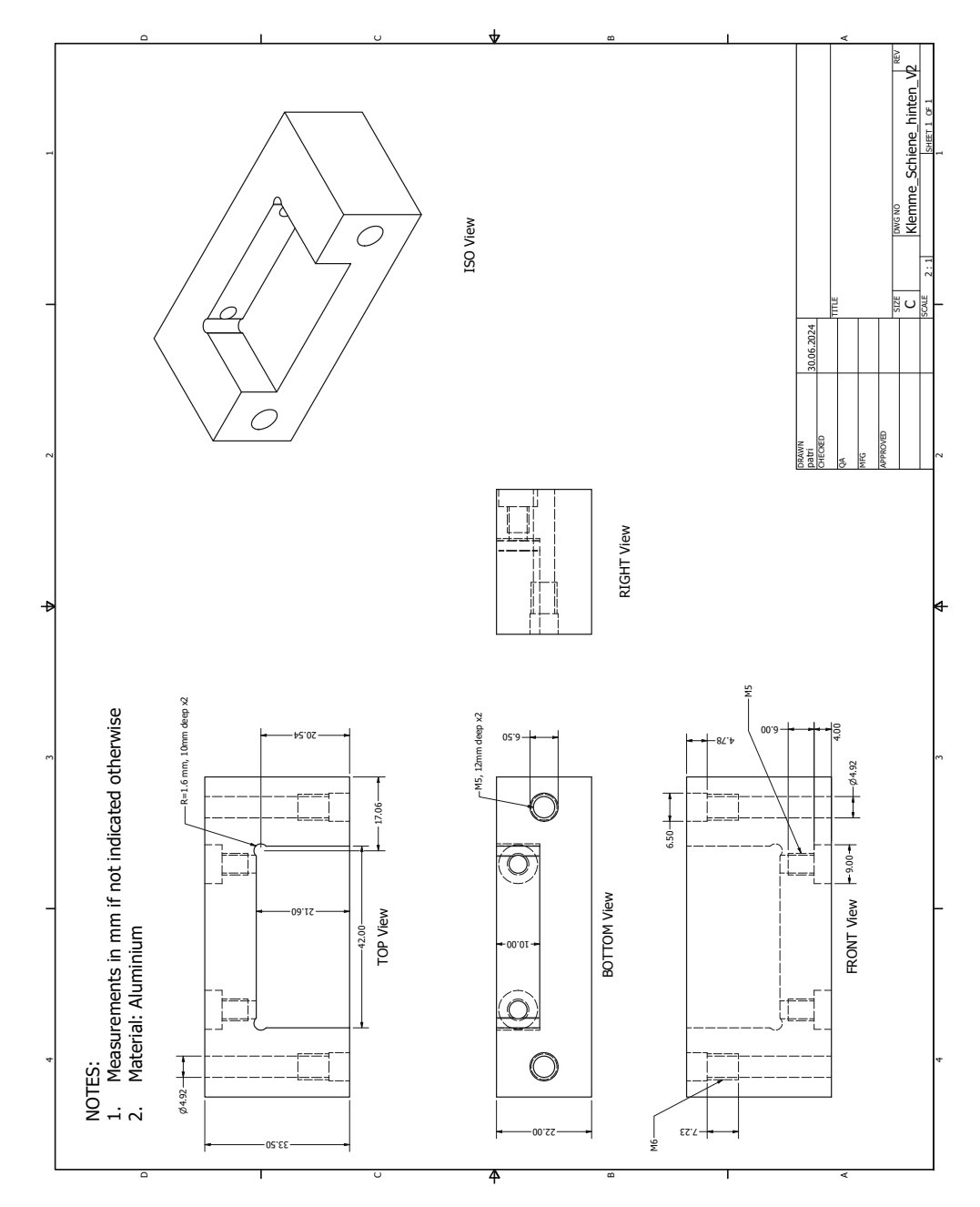


Figure 10.31

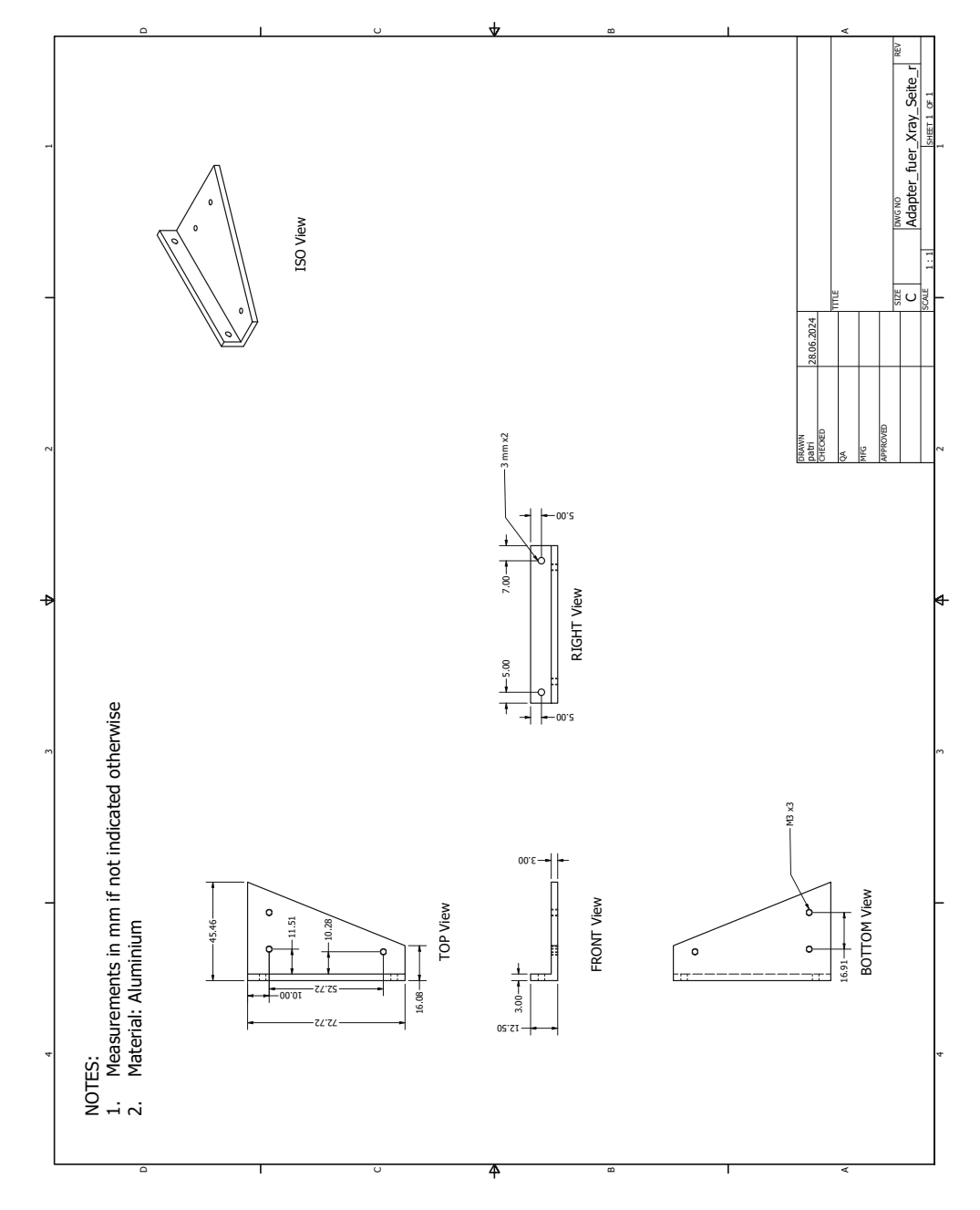


Figure 10.32

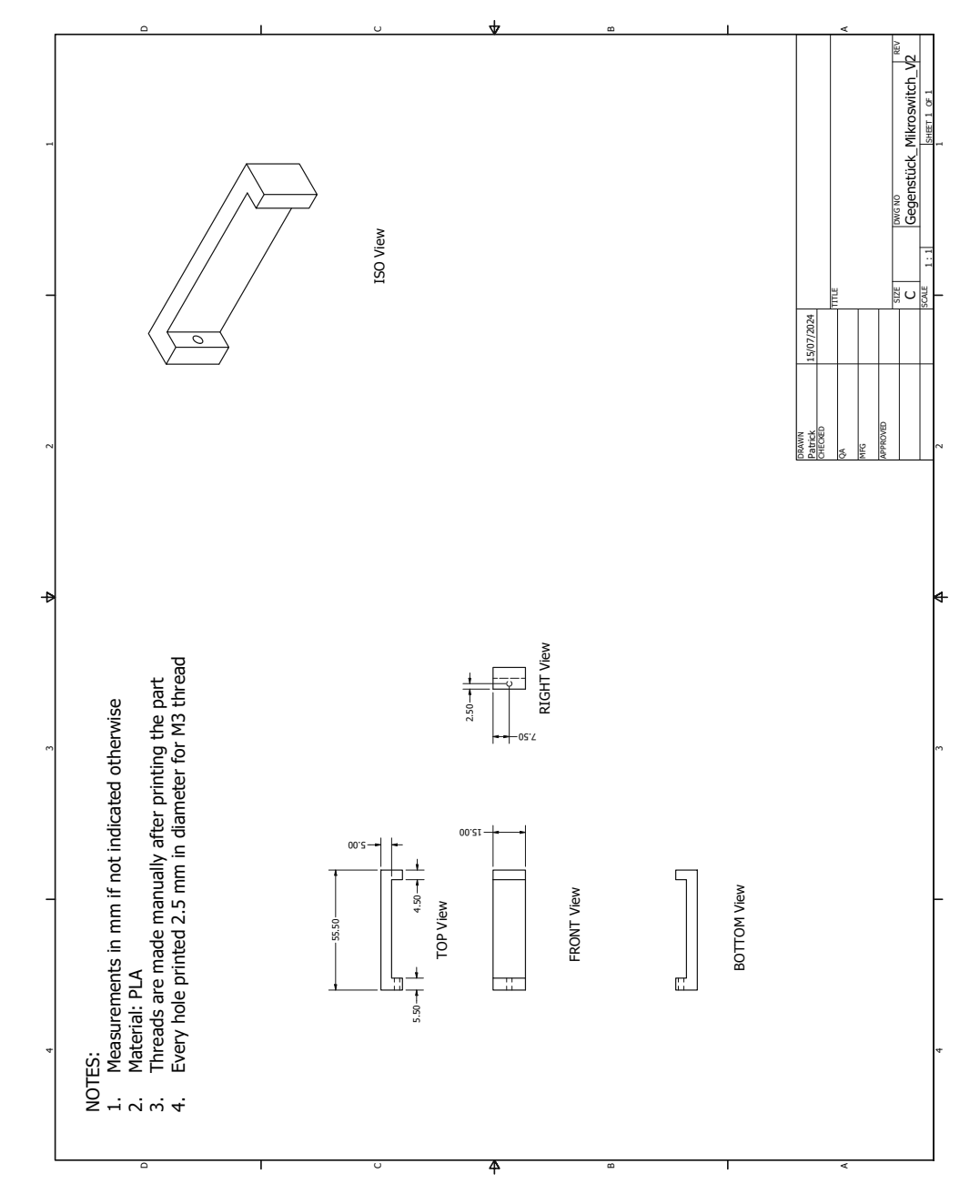


Figure 10.33

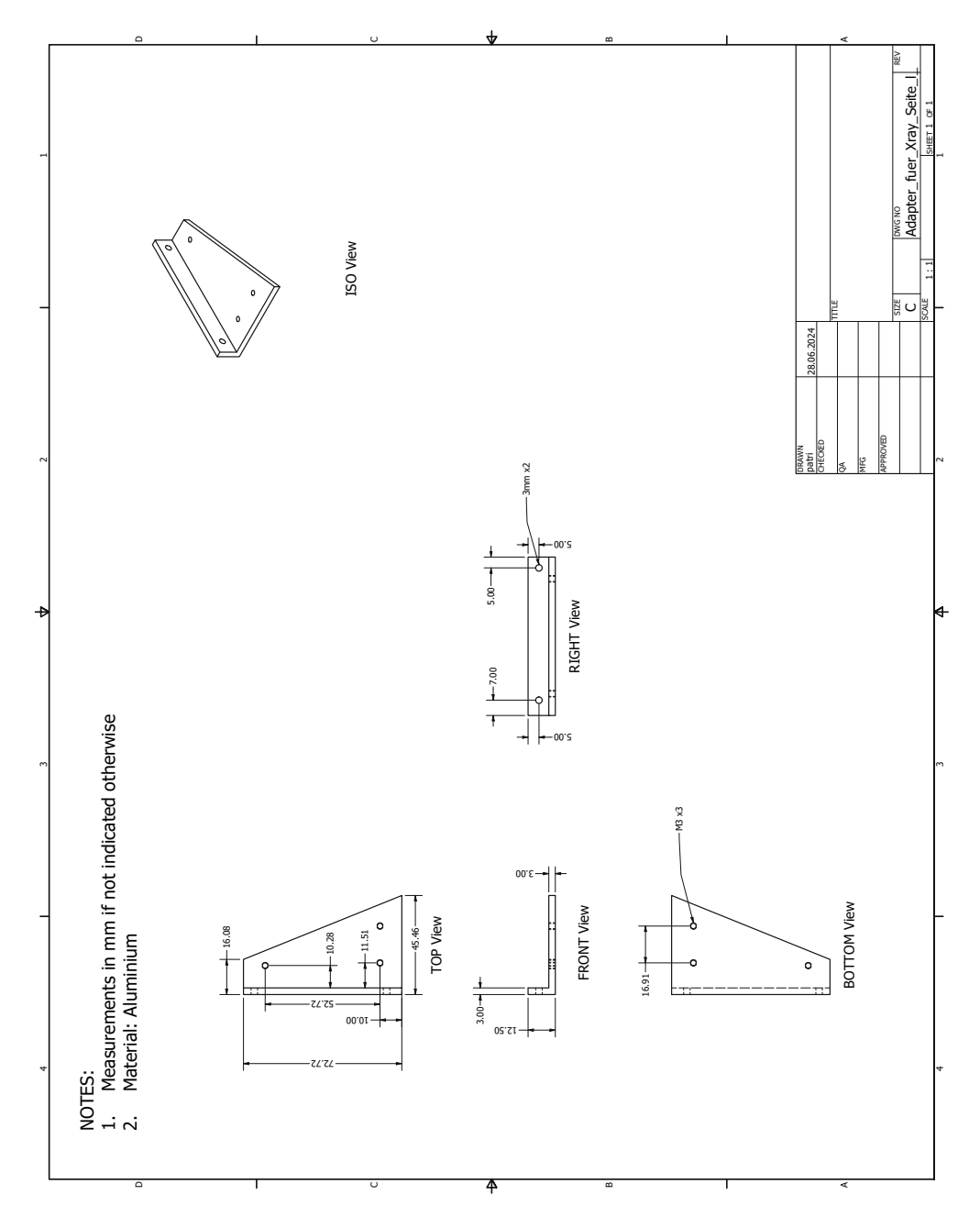


Figure 10.34

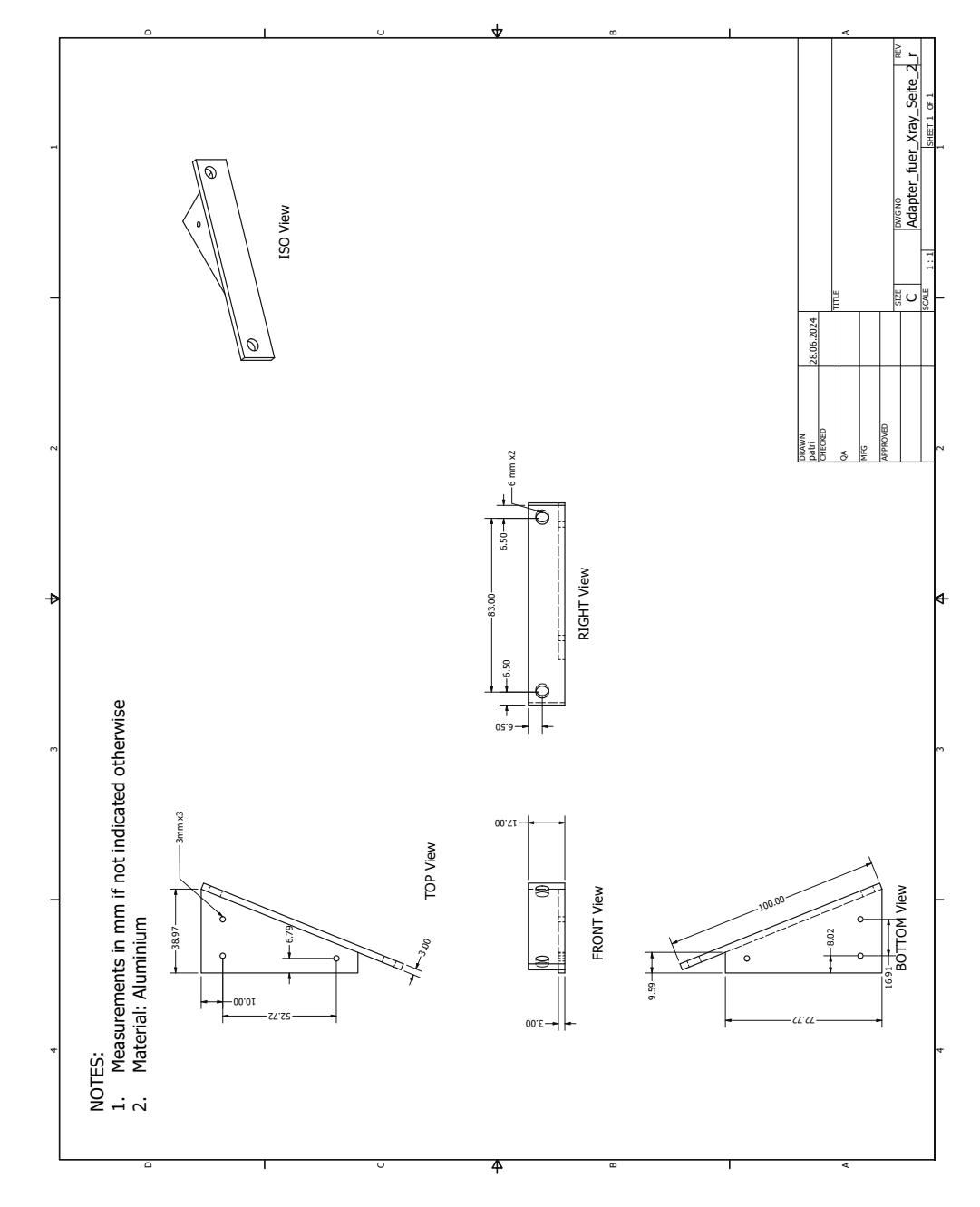


Figure 10.35

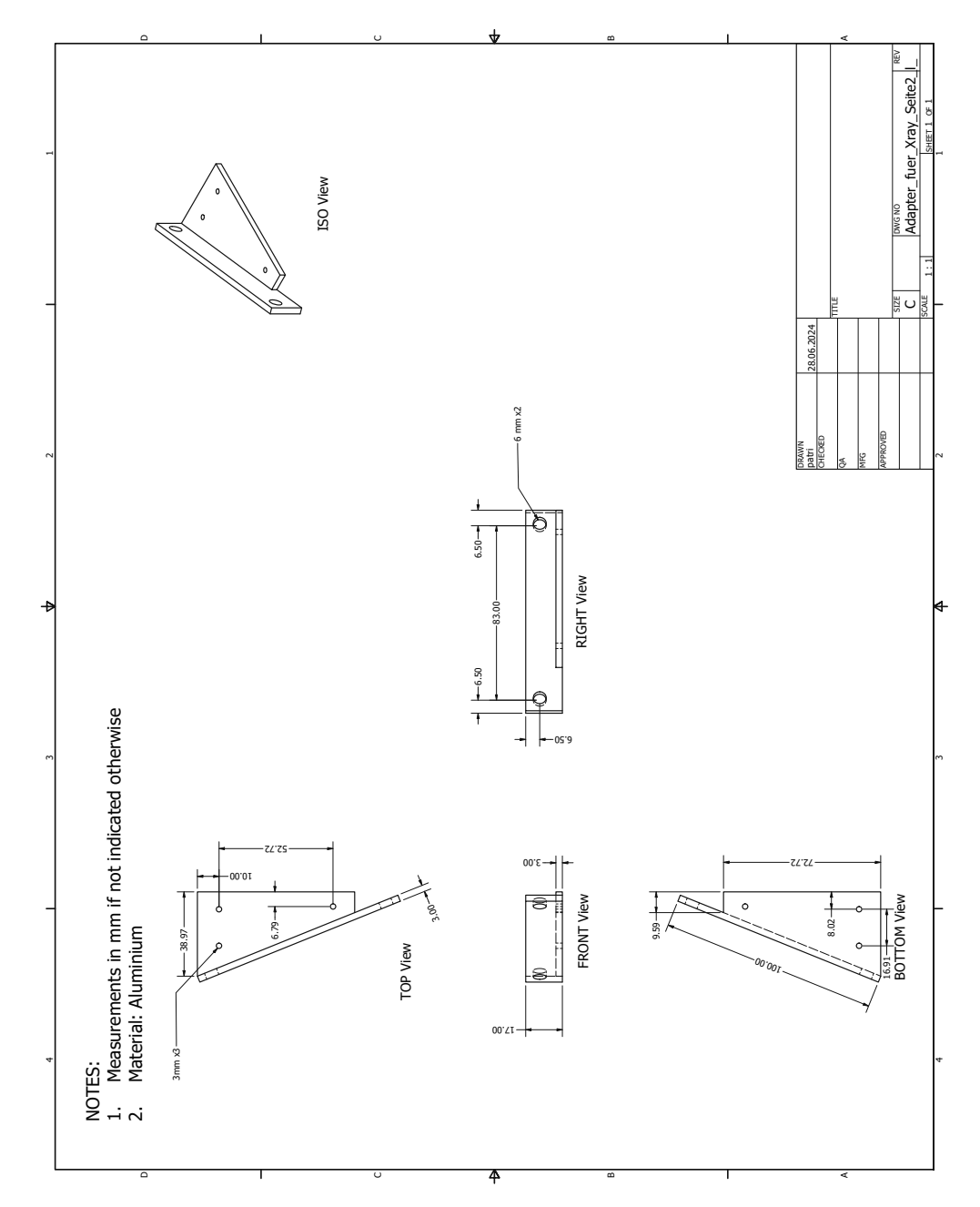


Figure 10.36

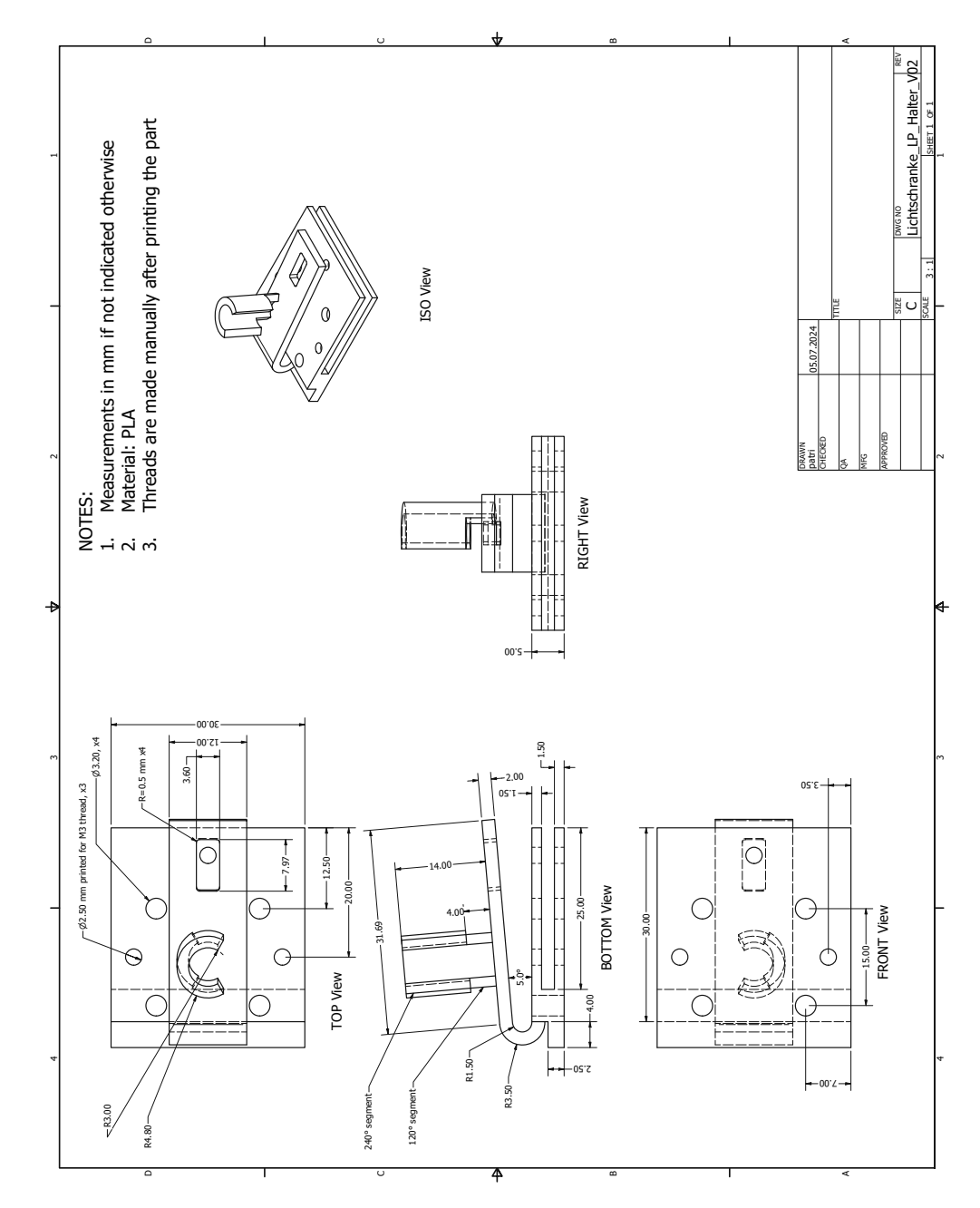


Figure 10.37

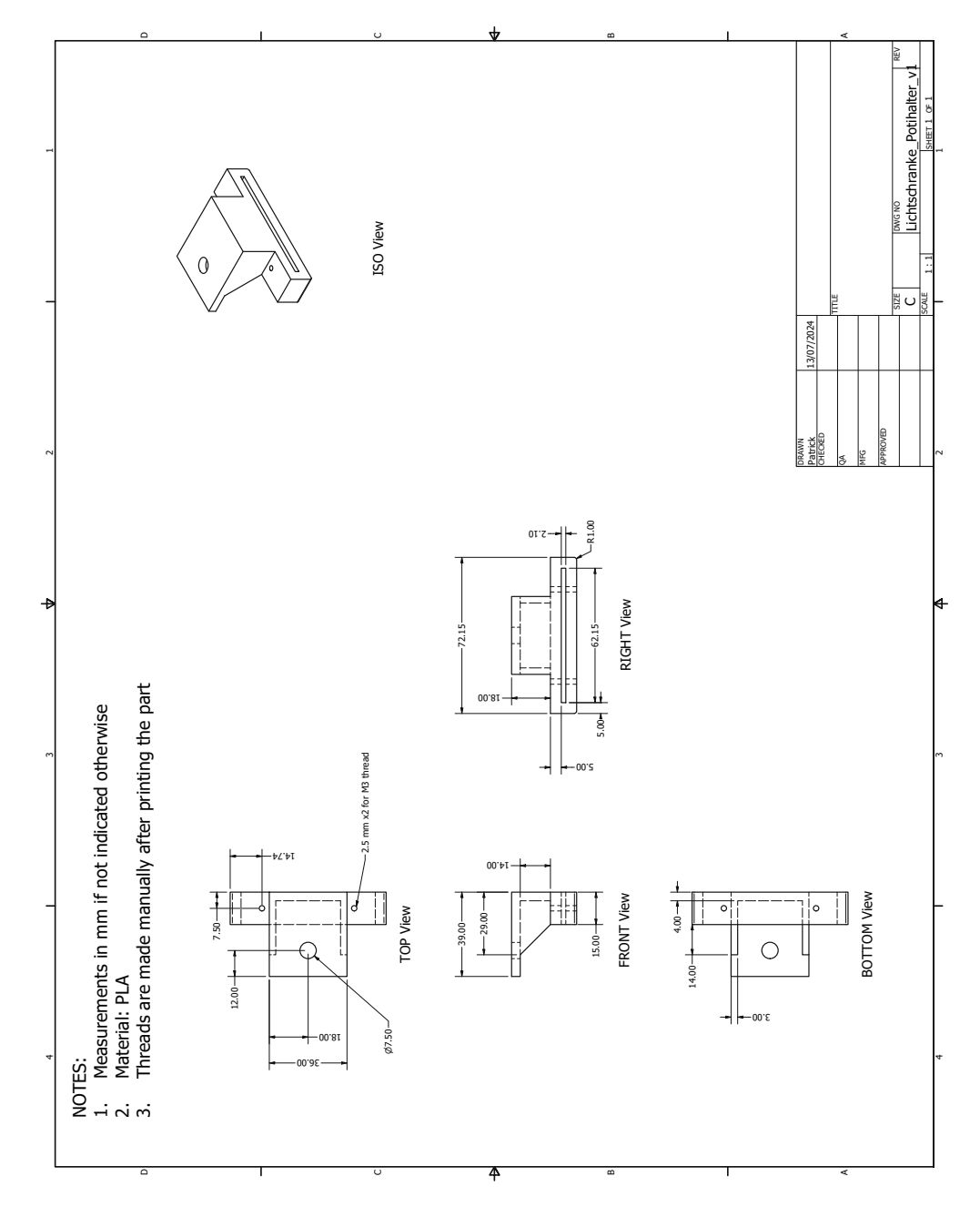


Figure 10.38

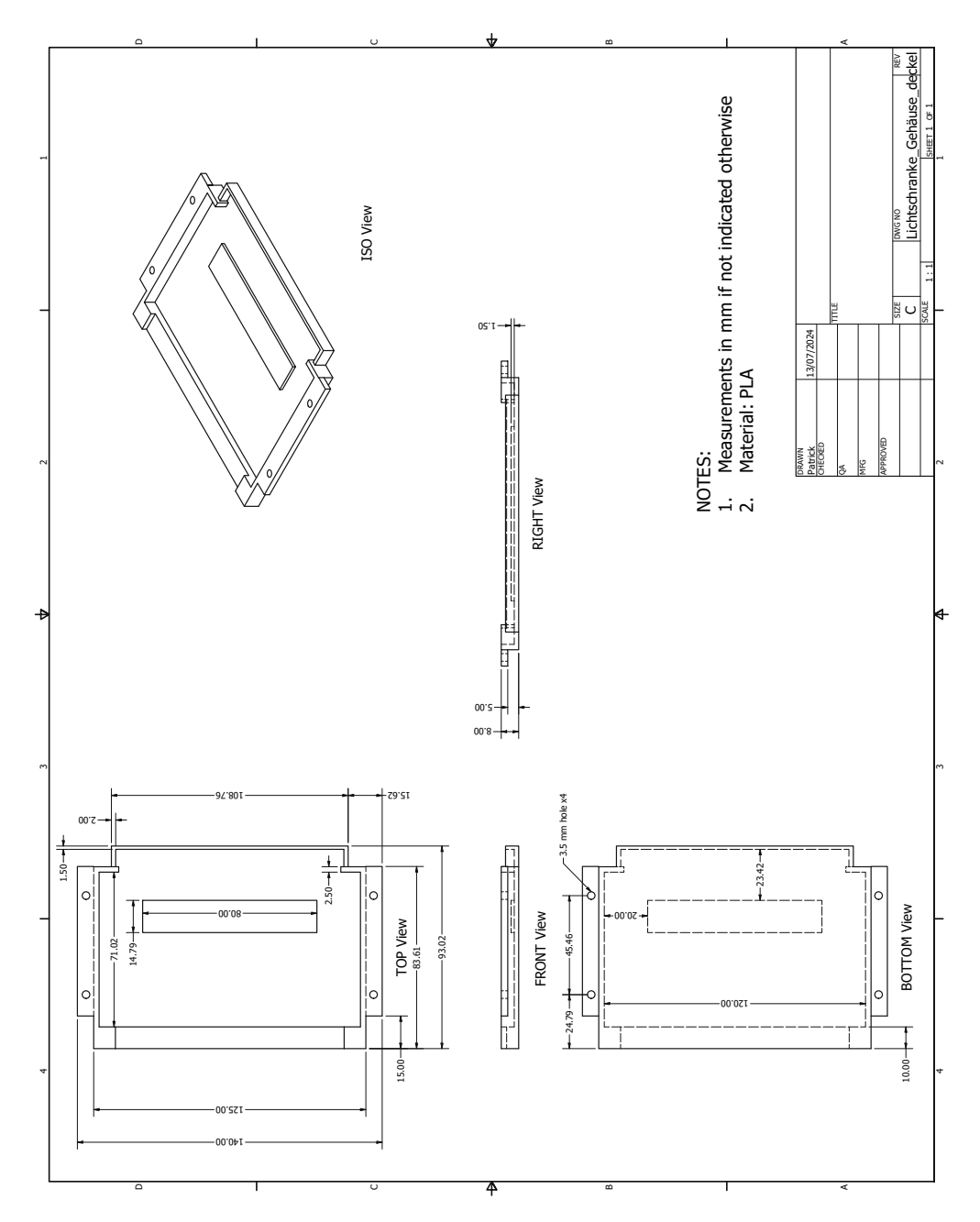


Figure 10.39

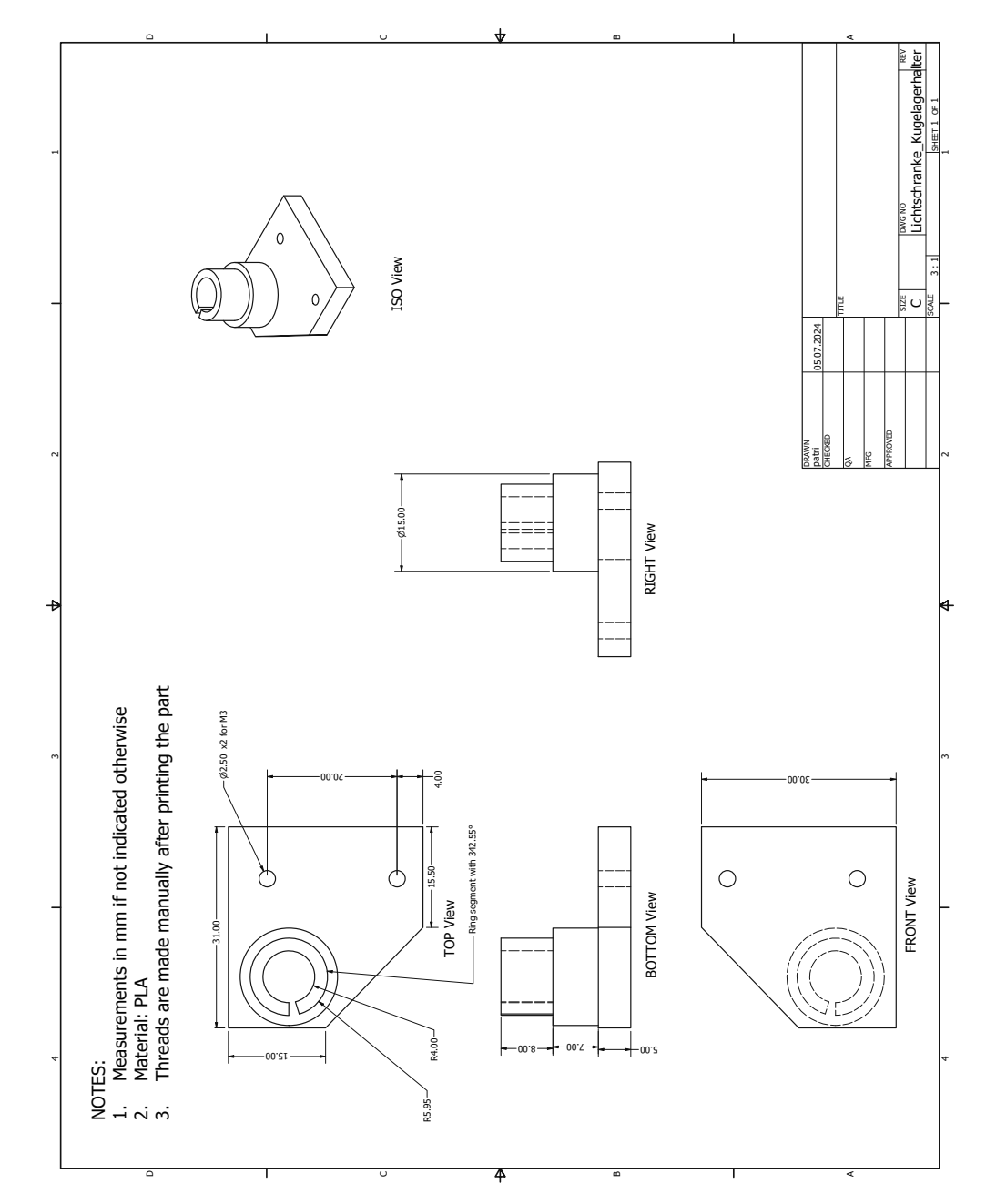


Figure 10.40

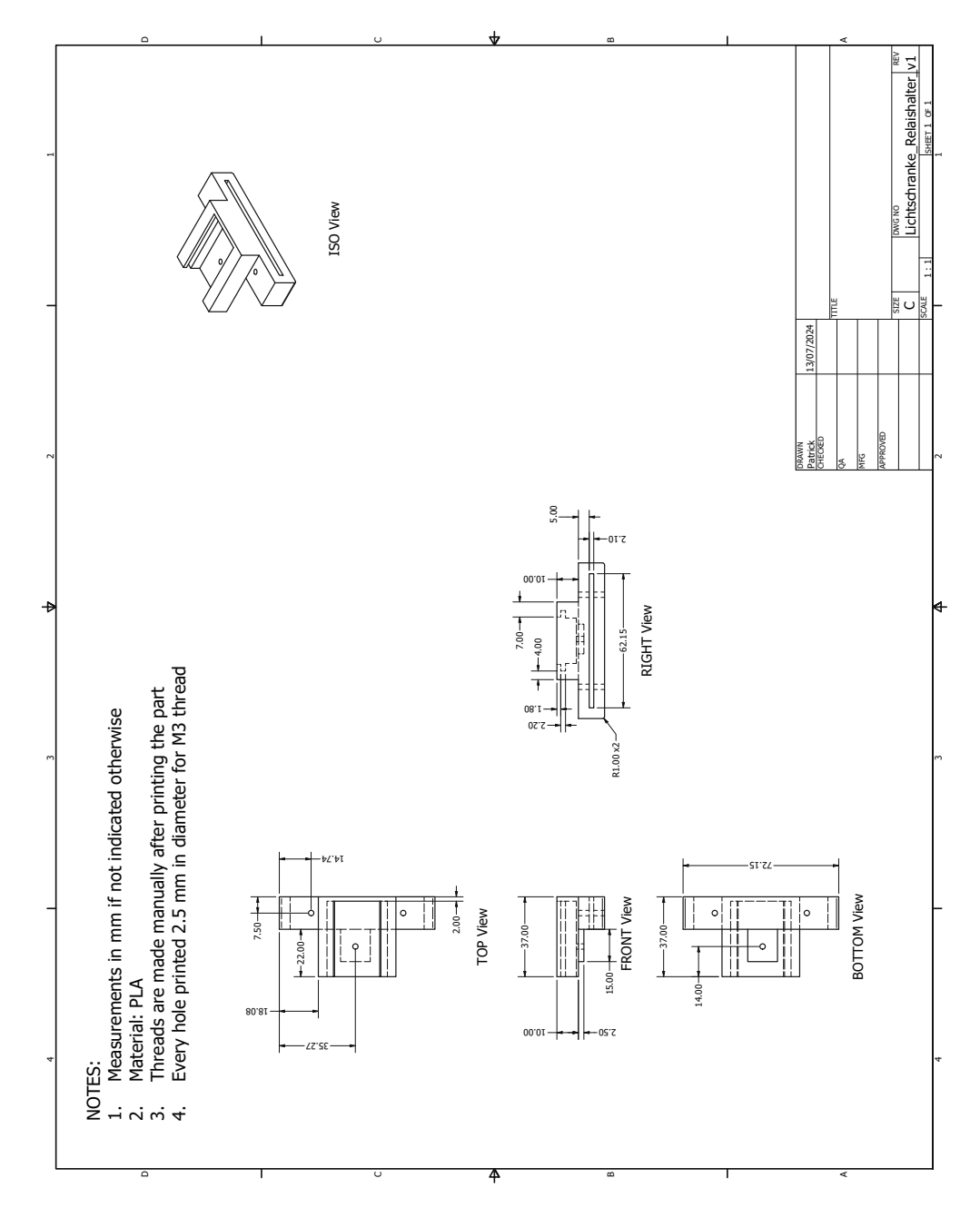


Figure 10.41

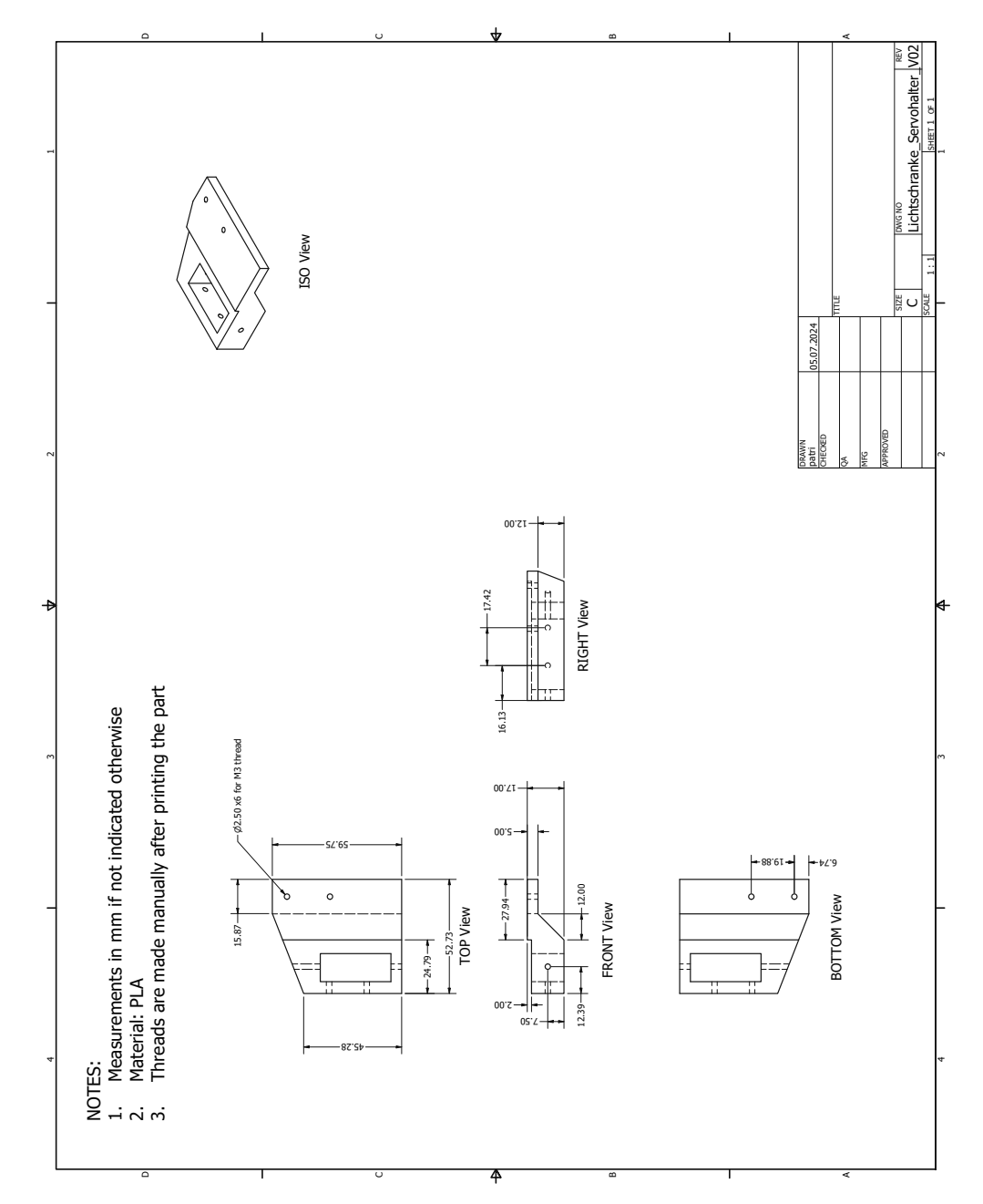


Figure 10.42

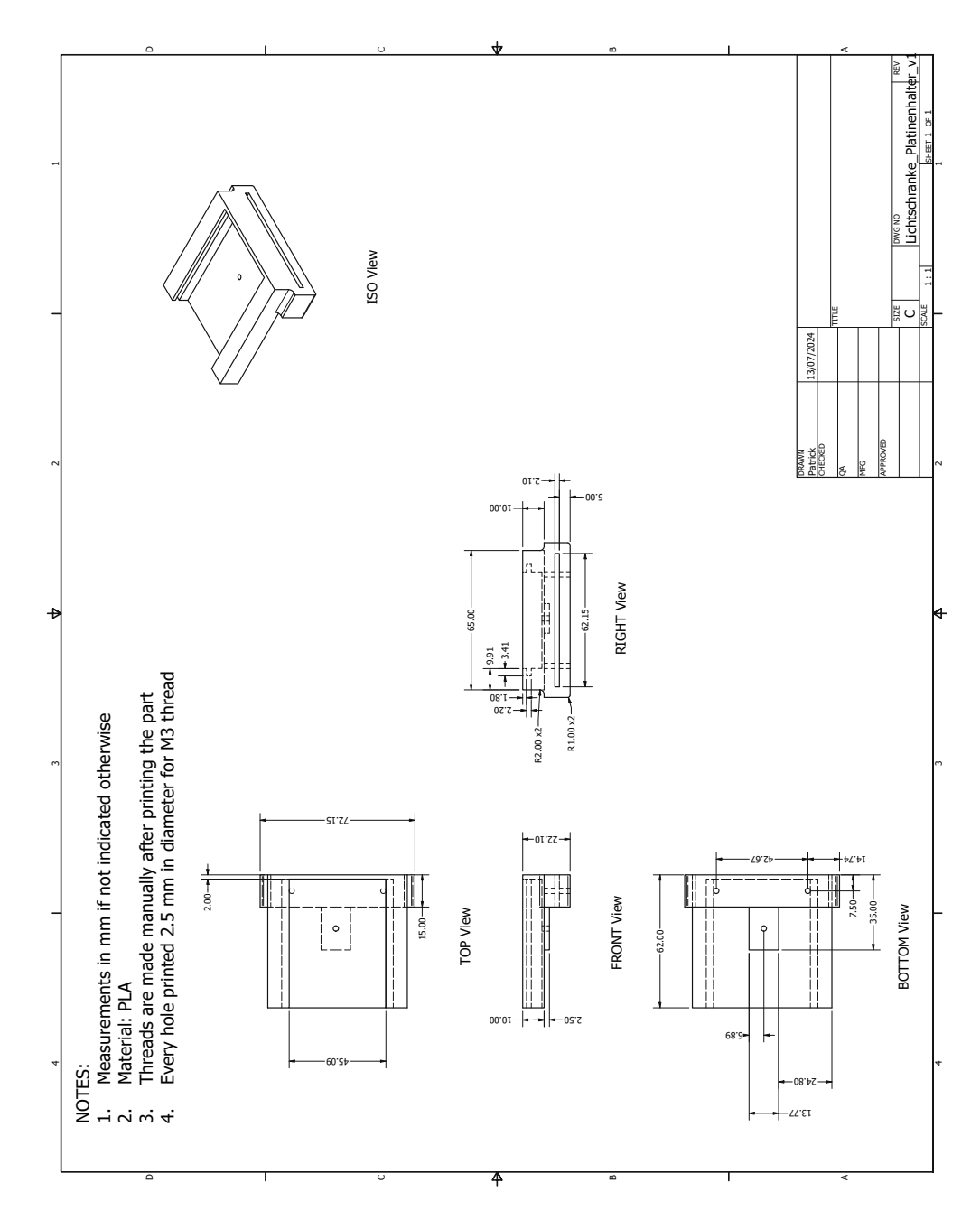


Figure 10.43

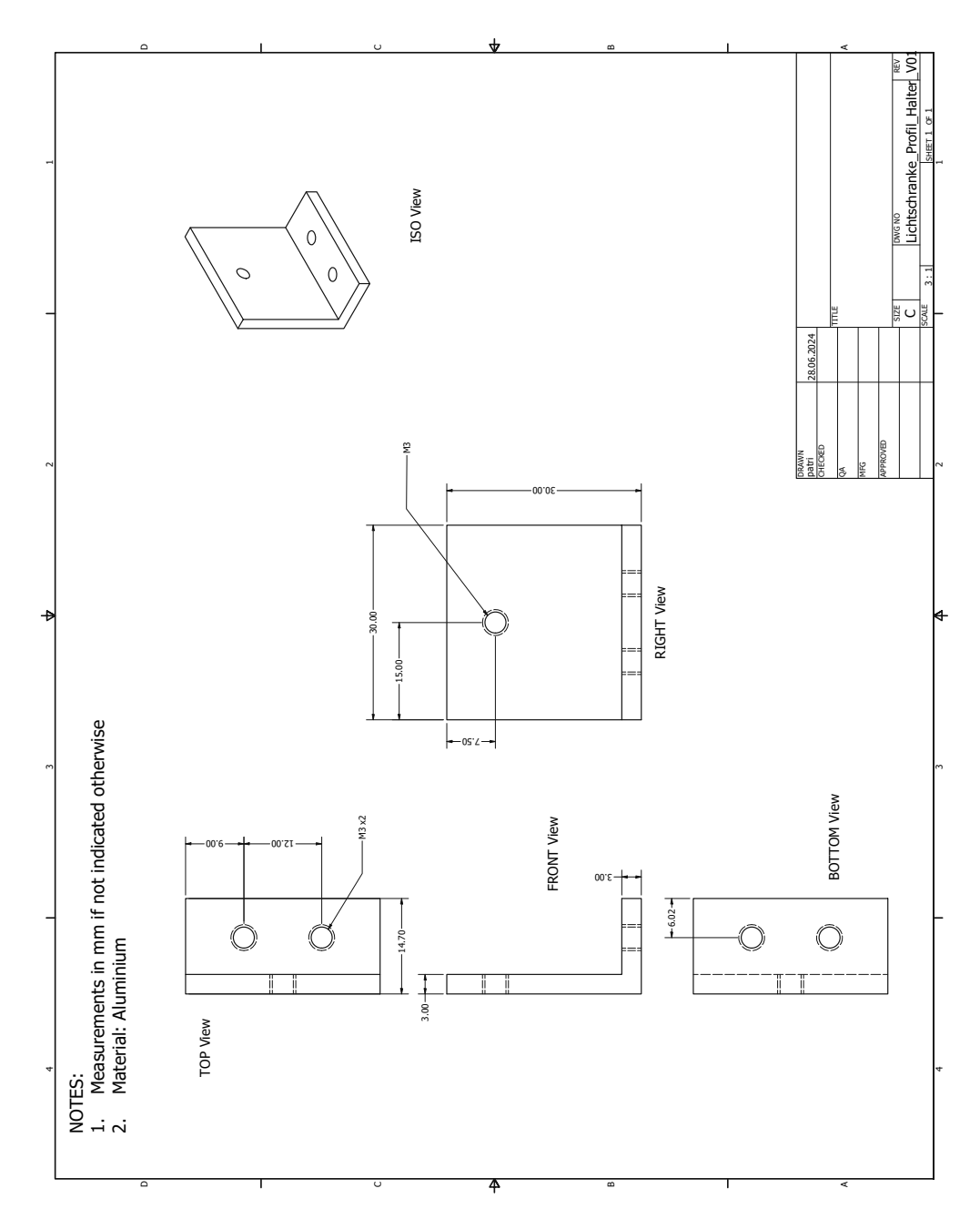


Figure 10.44

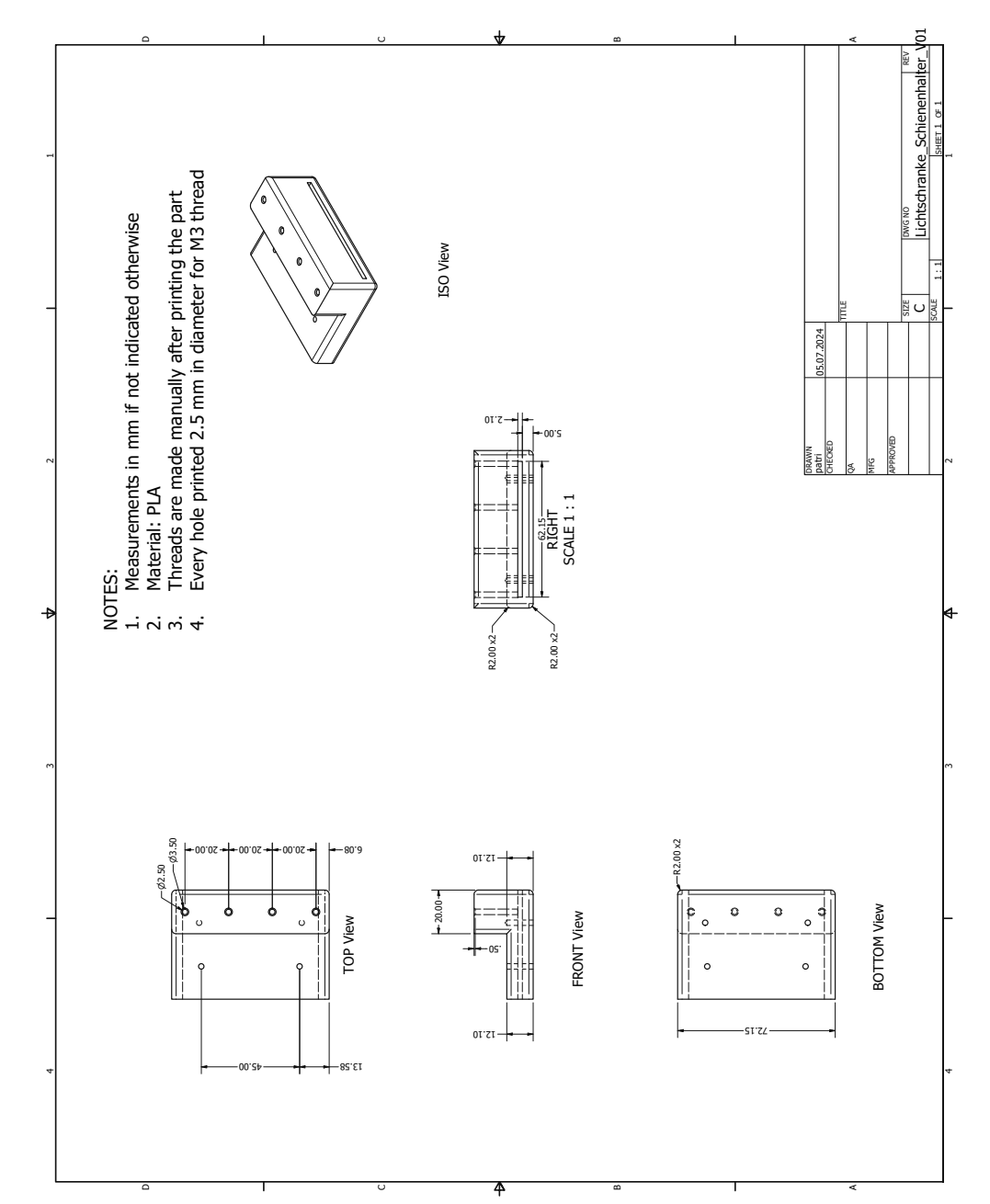


Figure 10.45

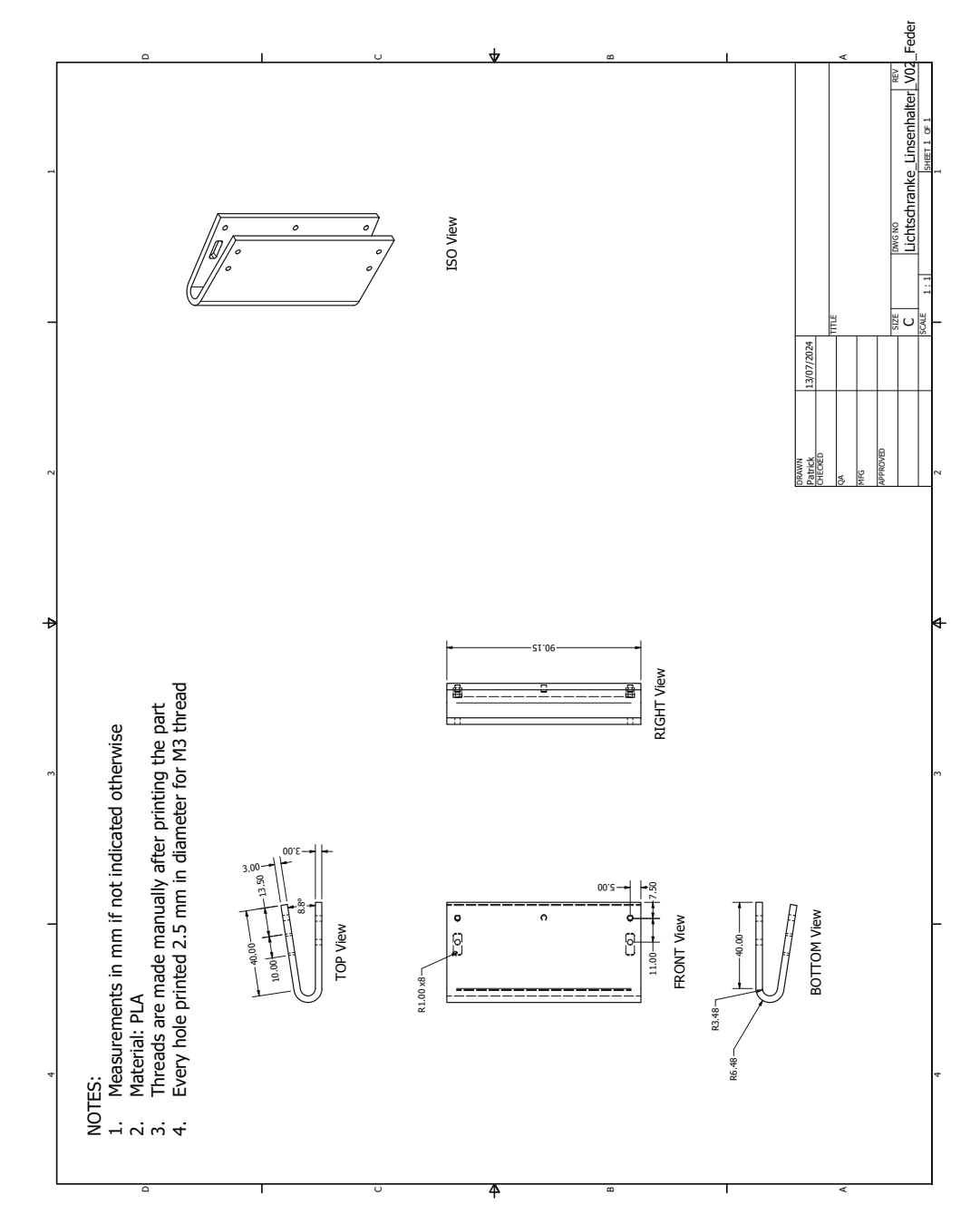


Figure 10.46

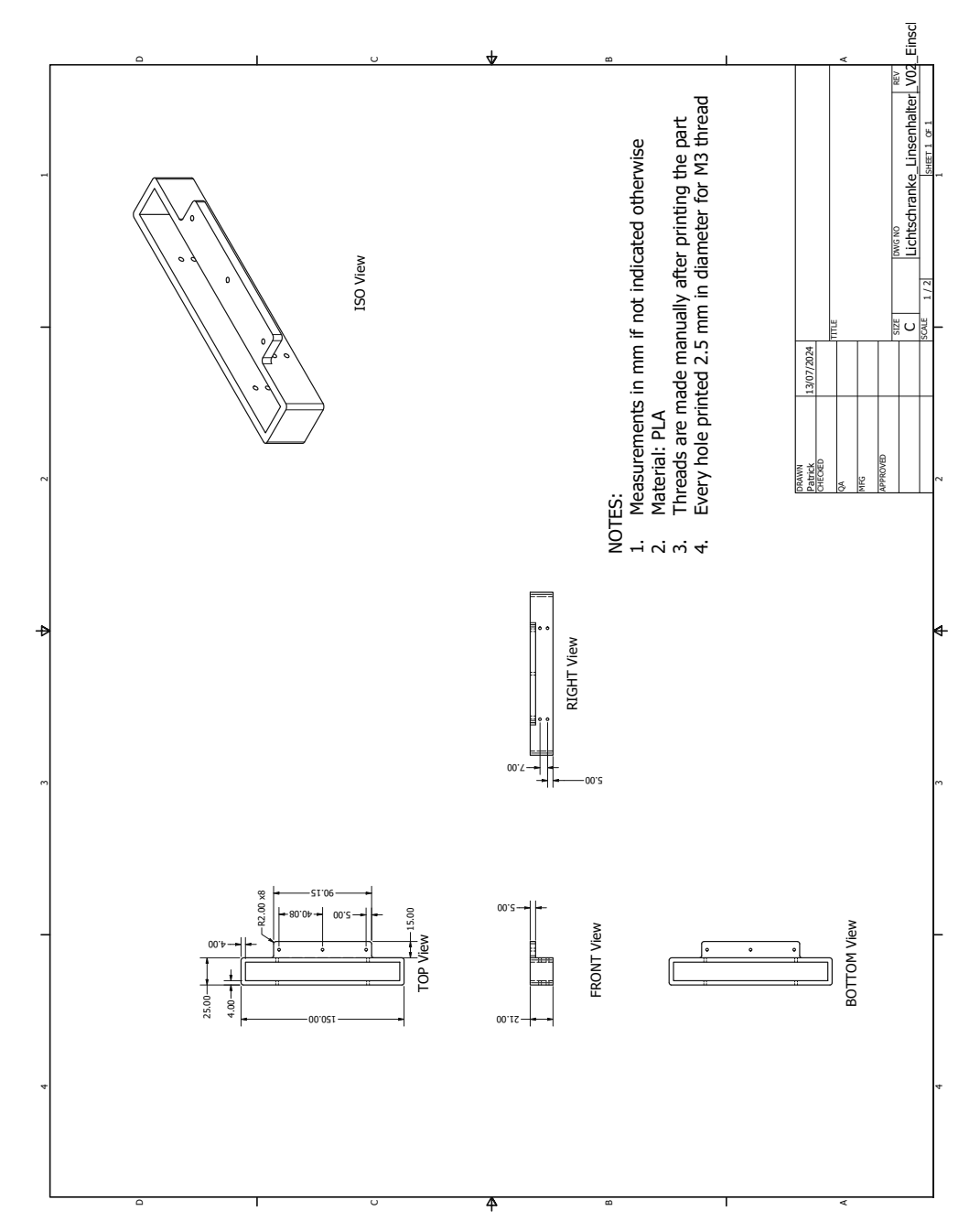


Figure 10.47

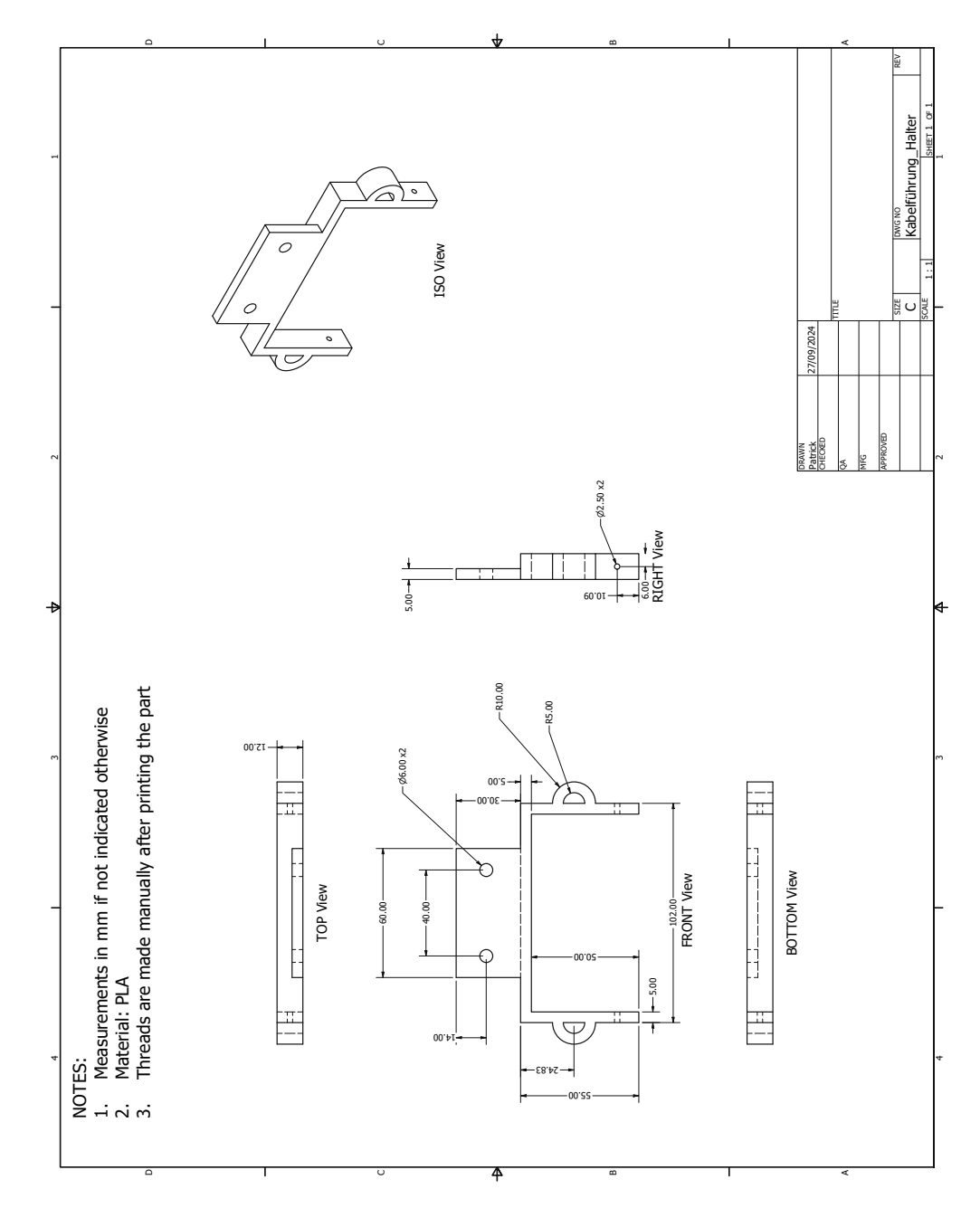


Figure 10.48

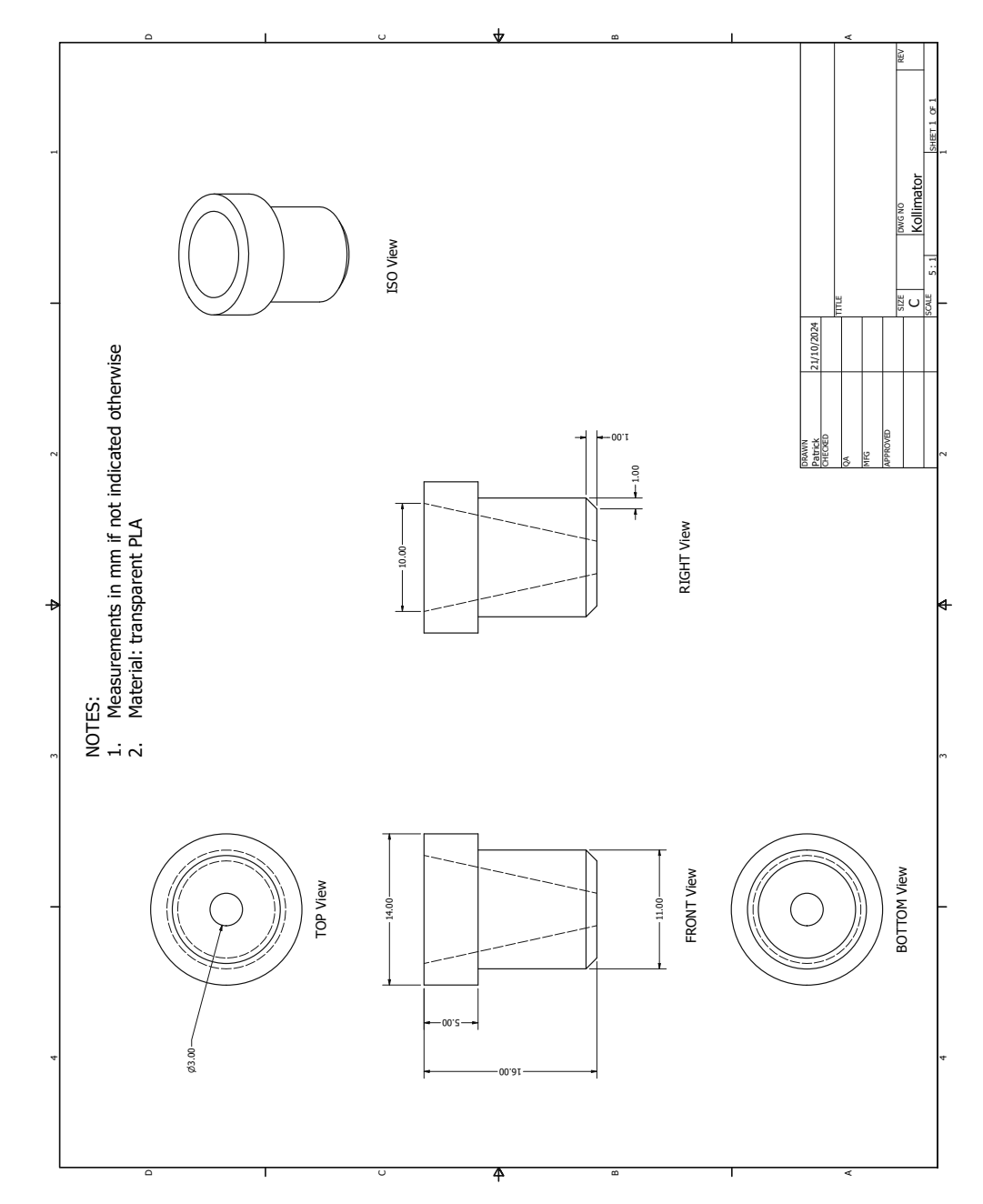


Figure 10.49

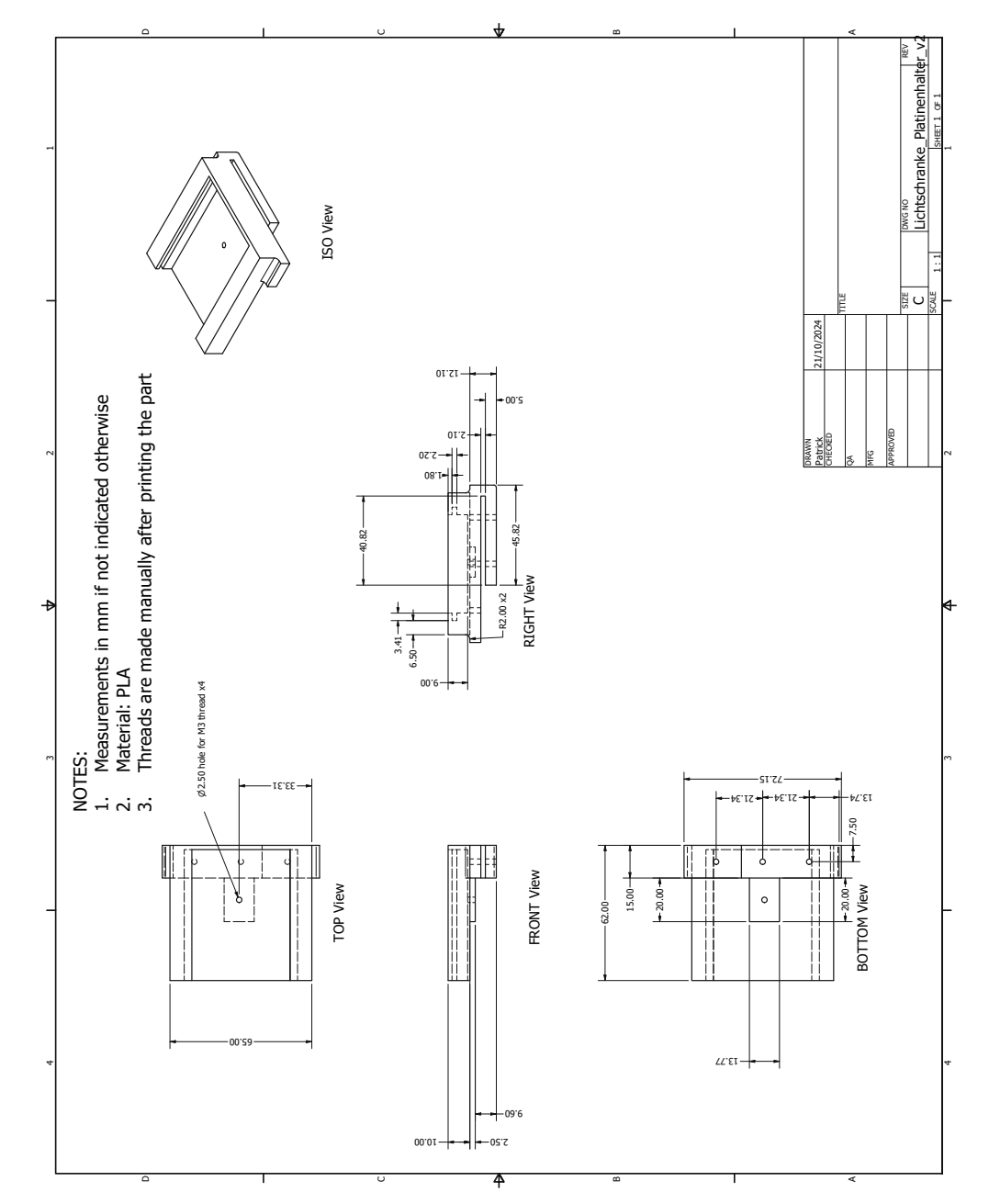


Figure 10.50

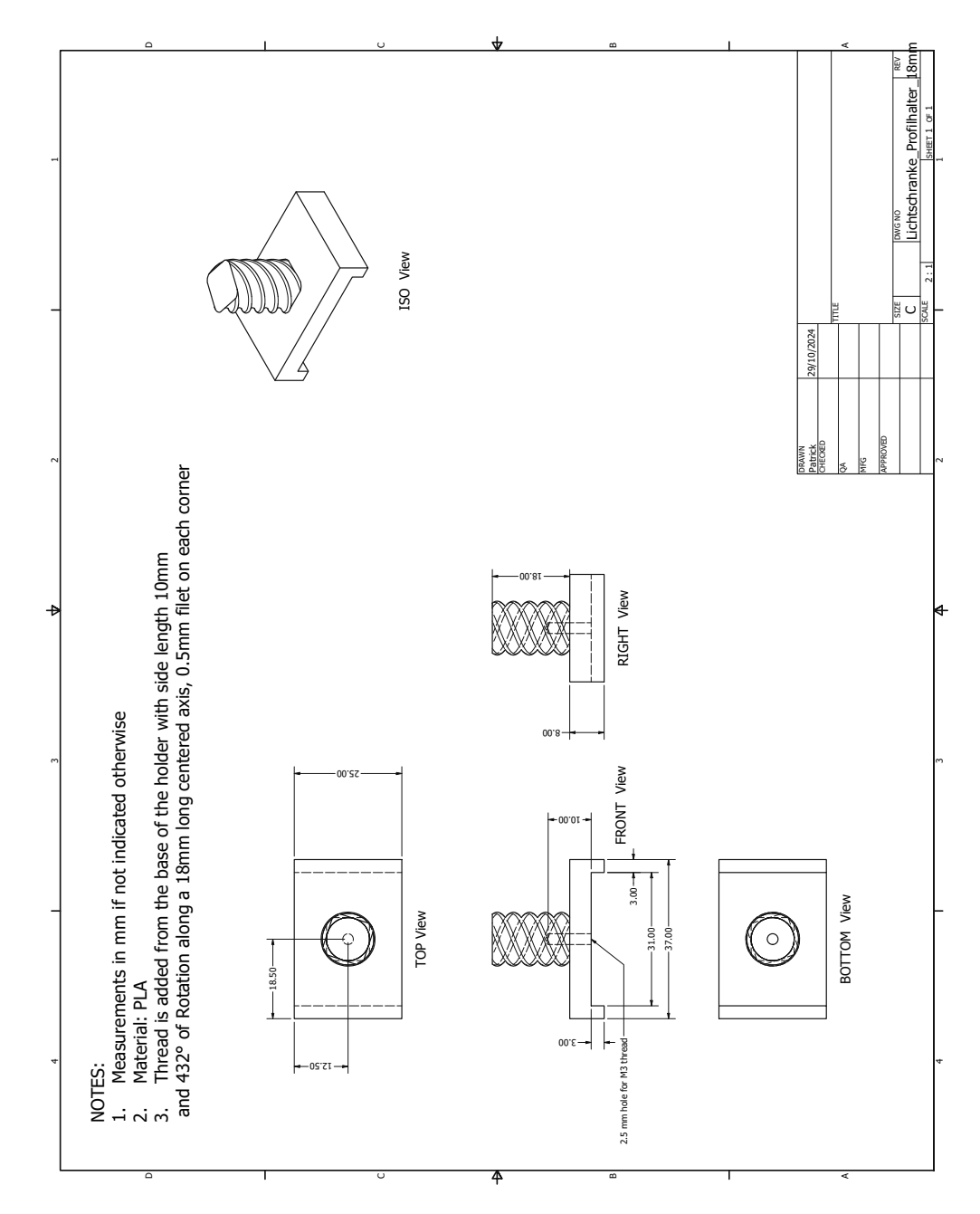


Figure 10.51

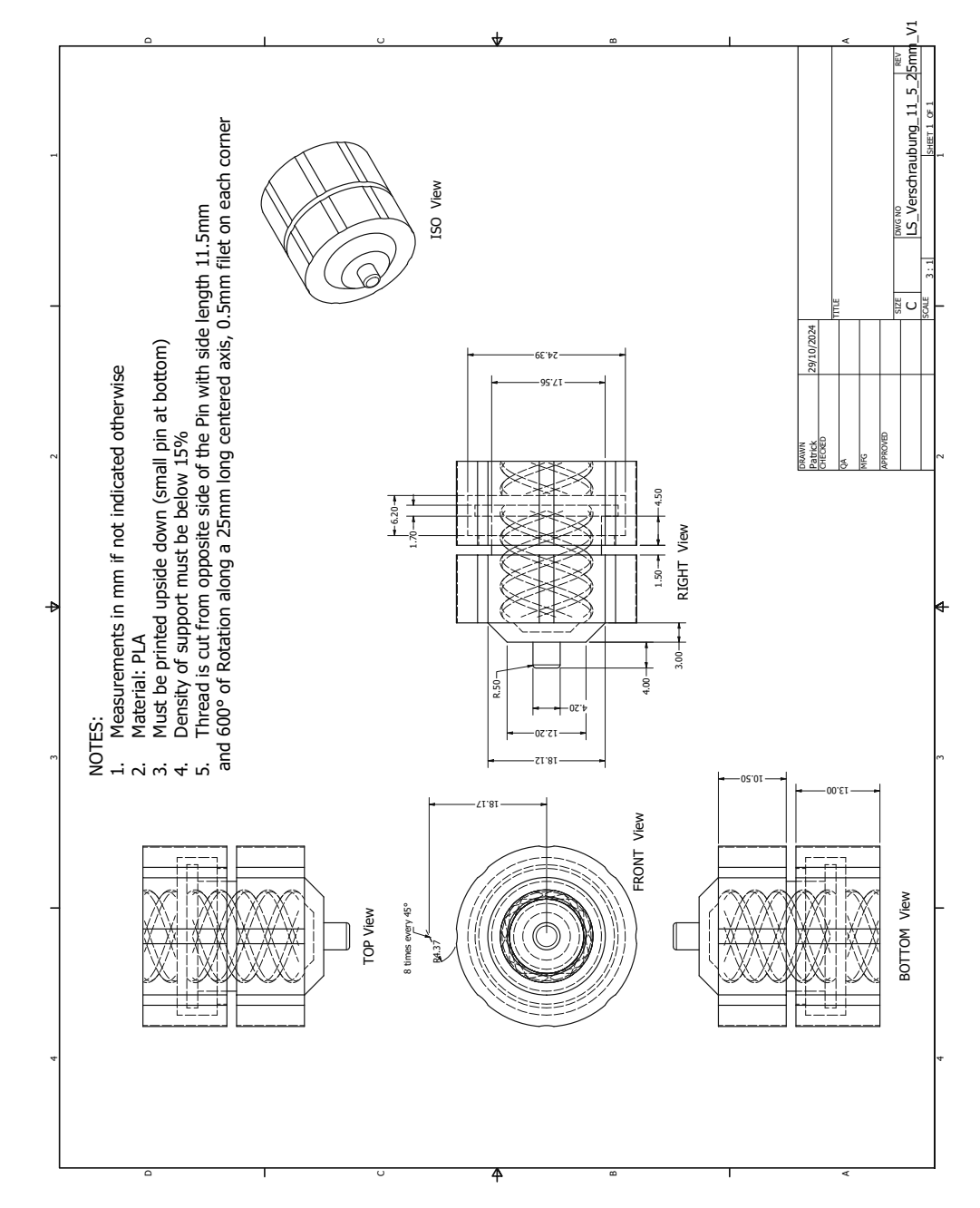


Figure 10.52

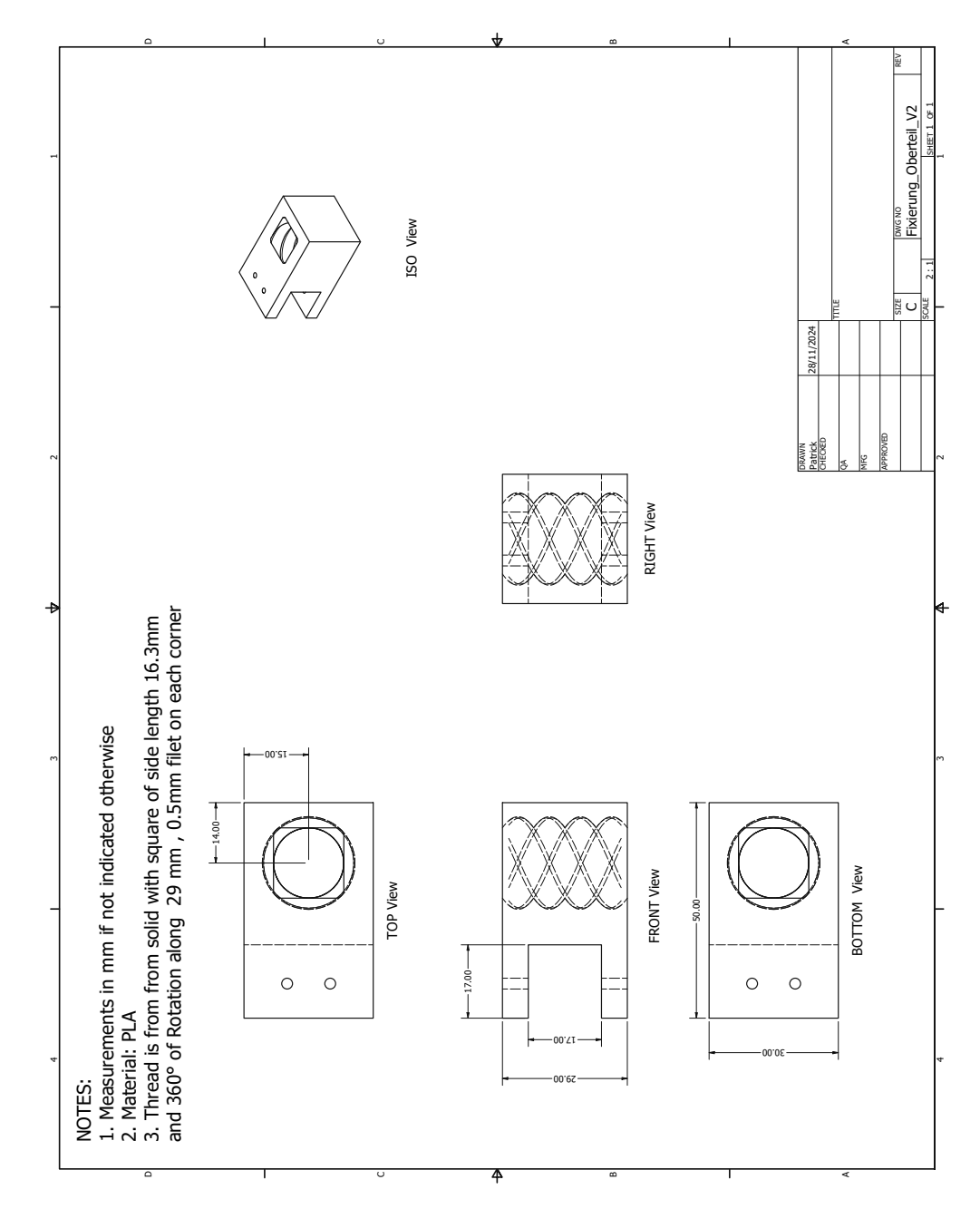


Figure 10.53

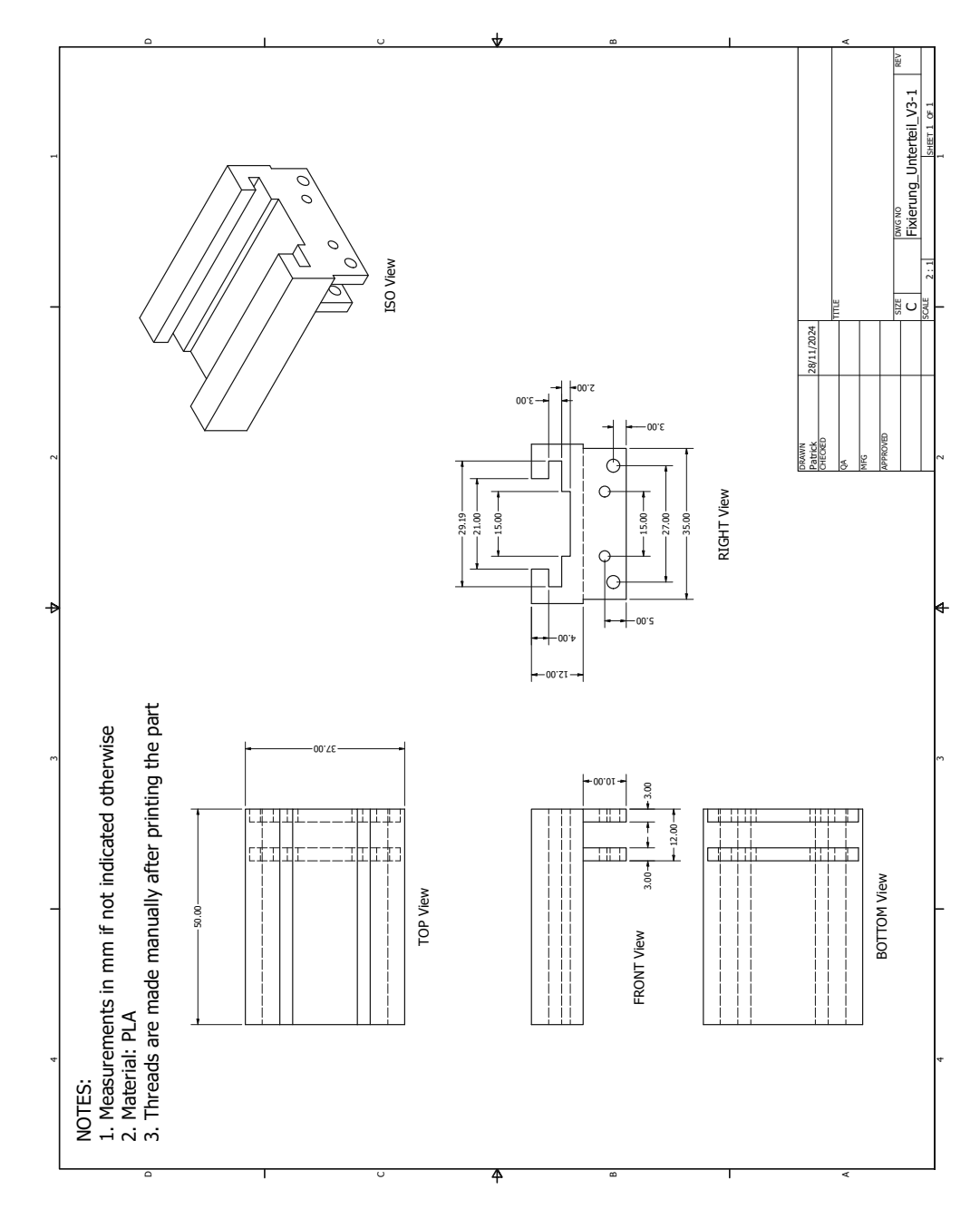


Figure 10.54

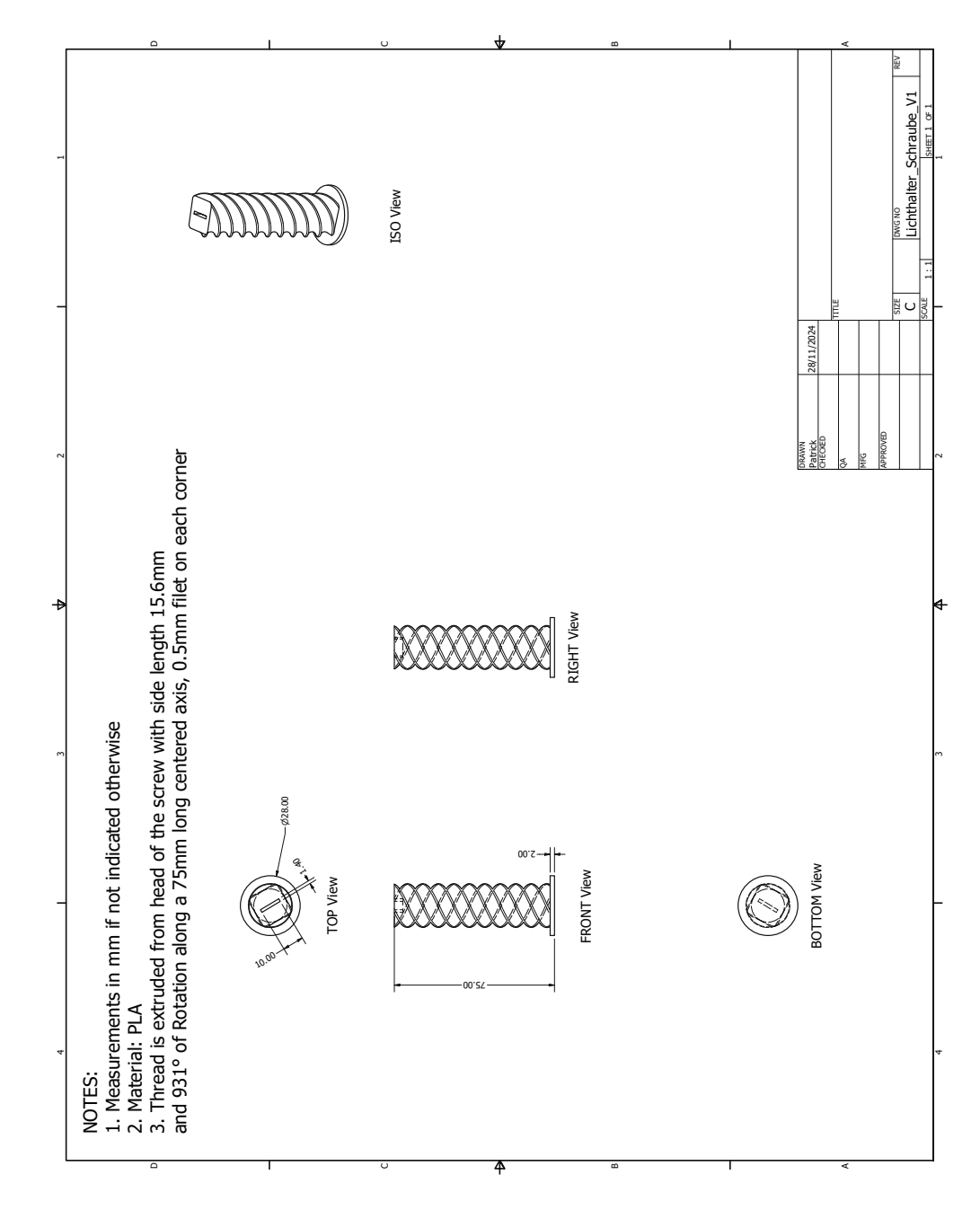


Figure 10.55

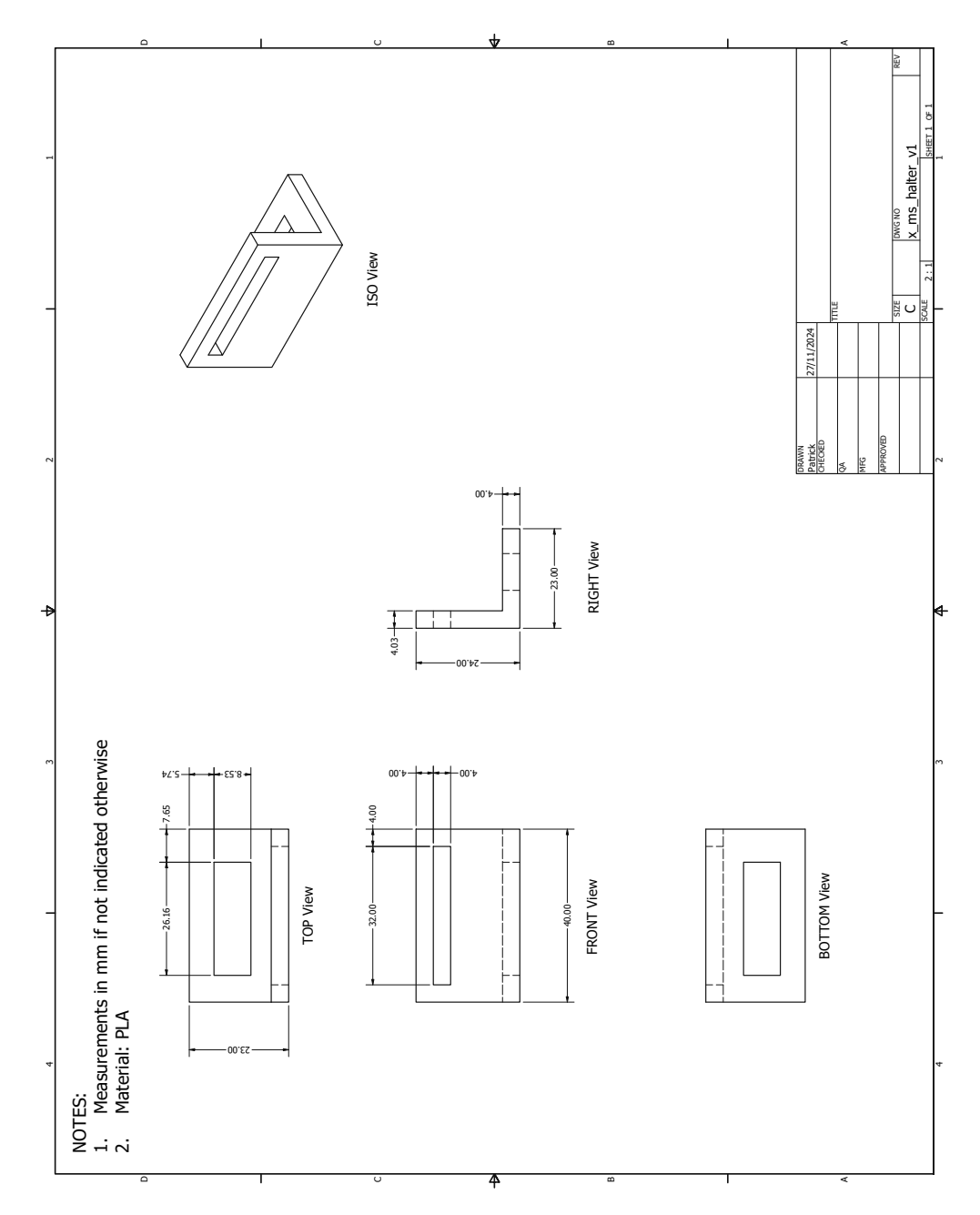


Figure 10.56

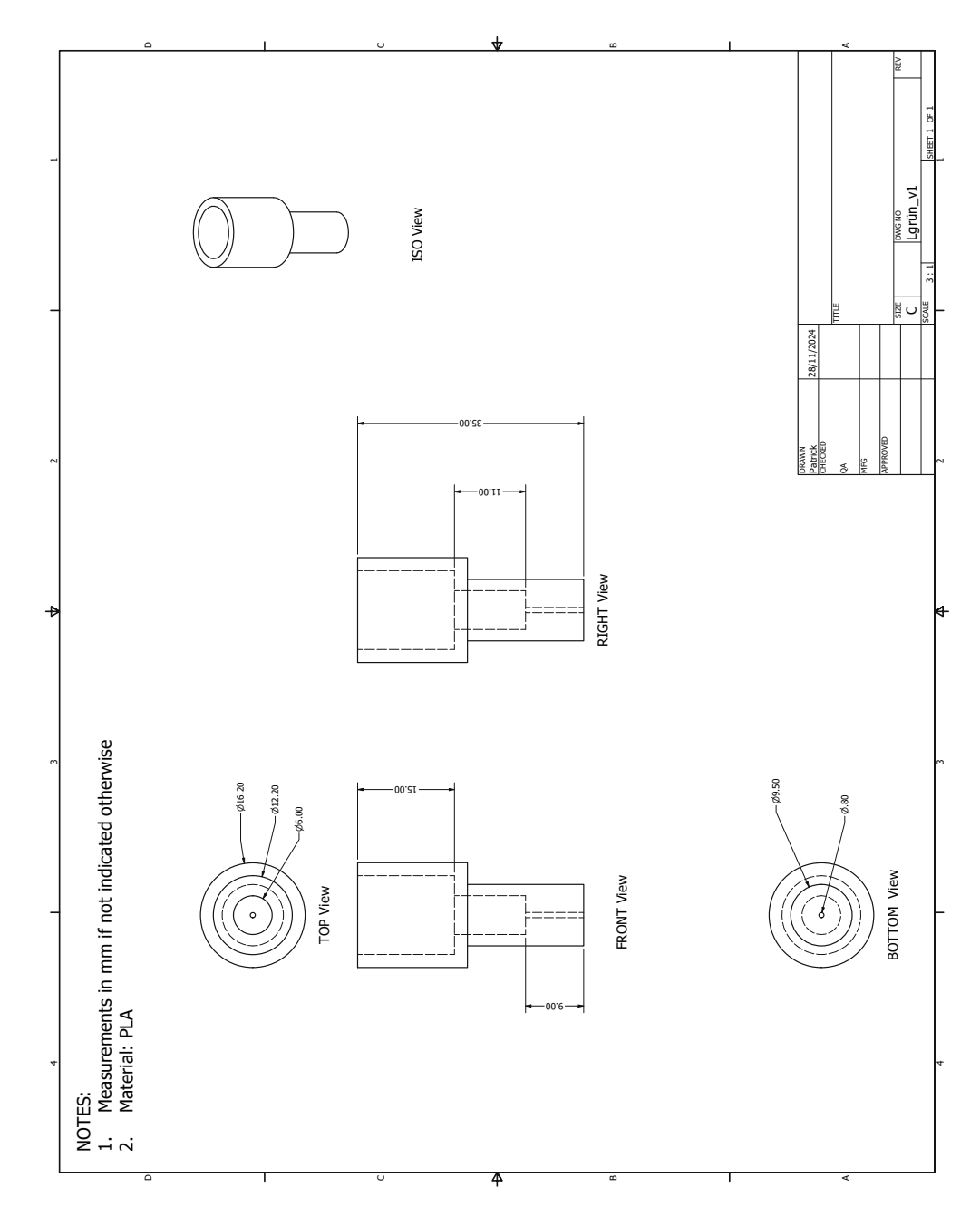


Figure 10.57

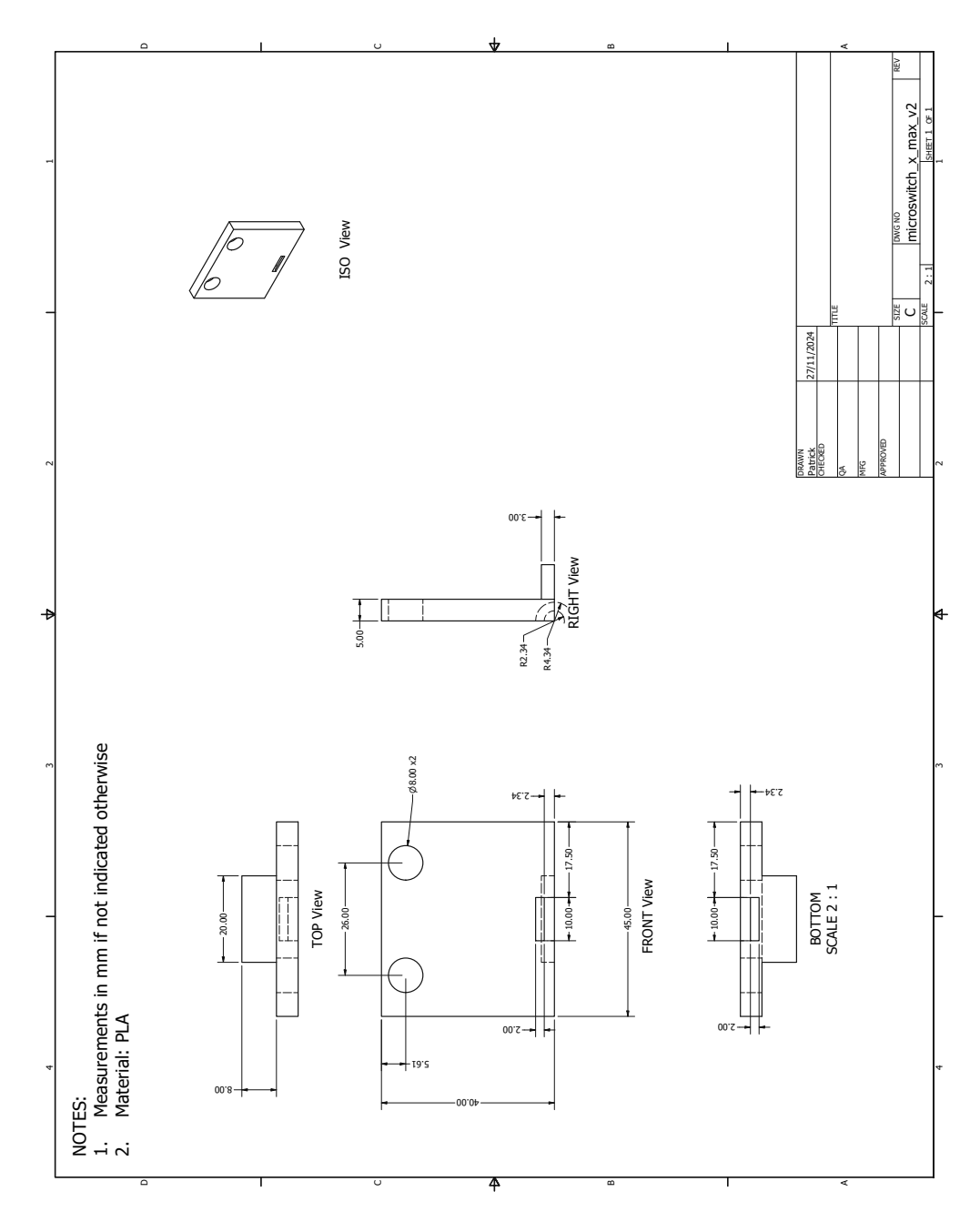


Figure 10.58

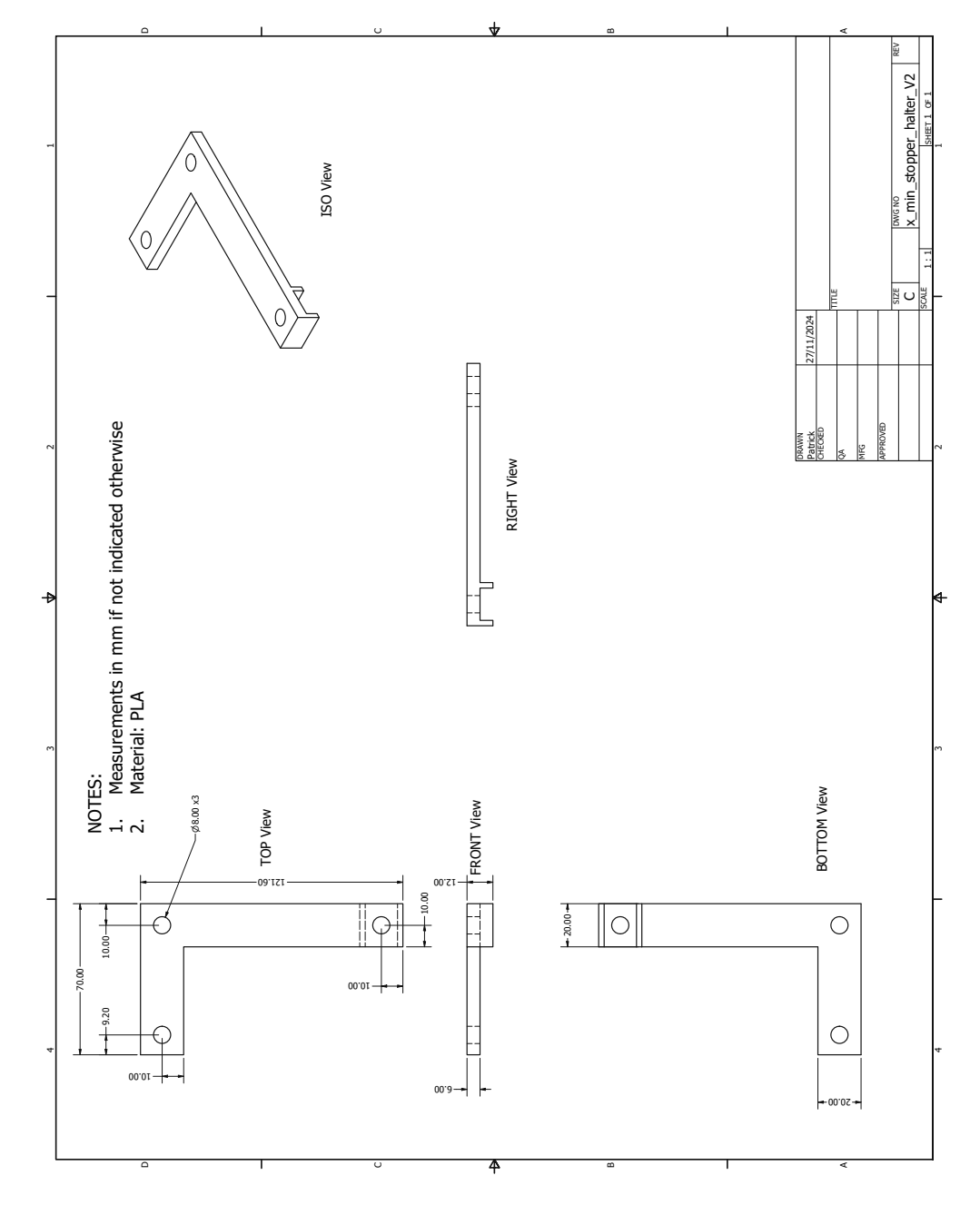


Figure 10.59

## 10.3 Setup the Light Barrier

Every time, either the detector or the X-ray tube is changed, the light barrier also needs to be removed, mounted again and adjusted.

### 10.3.1 Removing the Light Barrier

Before attempting to remove the light barrier from the frame, make sure that the USB cables to the Arduino and the supply are disconnected as not to damage the cables and holders. The next step is to remove the angle adjustment of the light barrier. This is done be loosening the screws on the top of the attachment and removing the wedge on the side (see figure 10.60).

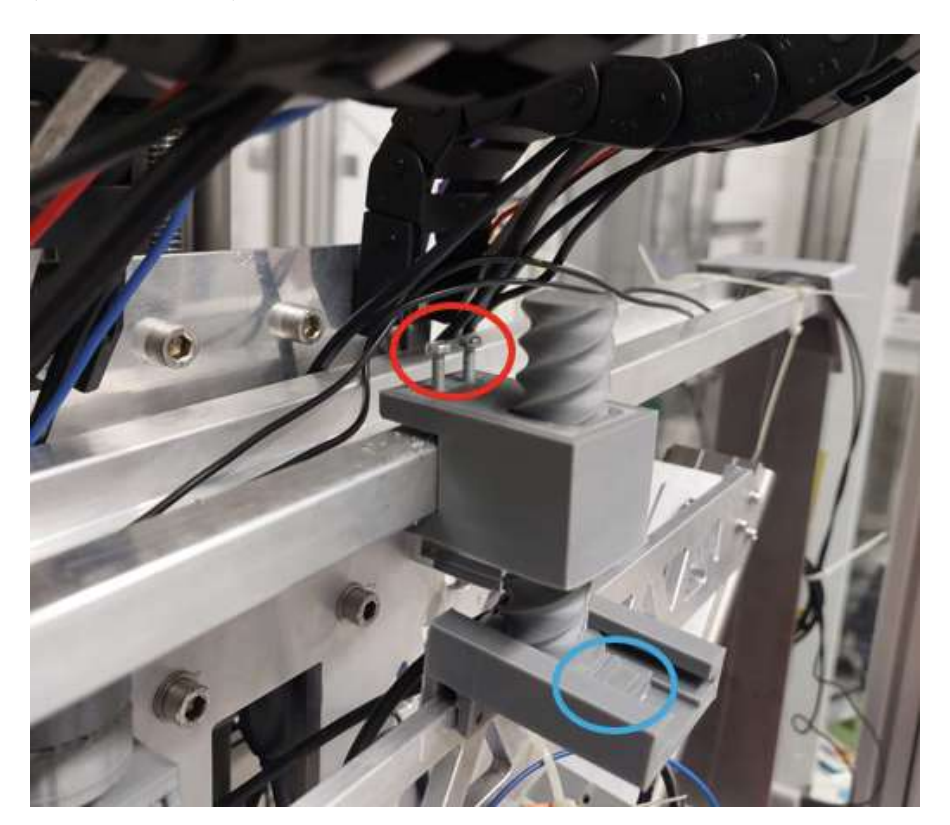


Figure 10.60: The screws that needs to be removed are circled in red and the wedge that needs to be pulled out in blue.

Gently lift the rail upwards from the pins and set it aside.

### 10.3.2 Mounting the Light Barrier

After inserting the tube or the detector back on the rail, the rail can be put back on the pins on the top of the frame. This should be done gently as not to push the pin down the thread. make sure that the entire top of the pin is inserted.

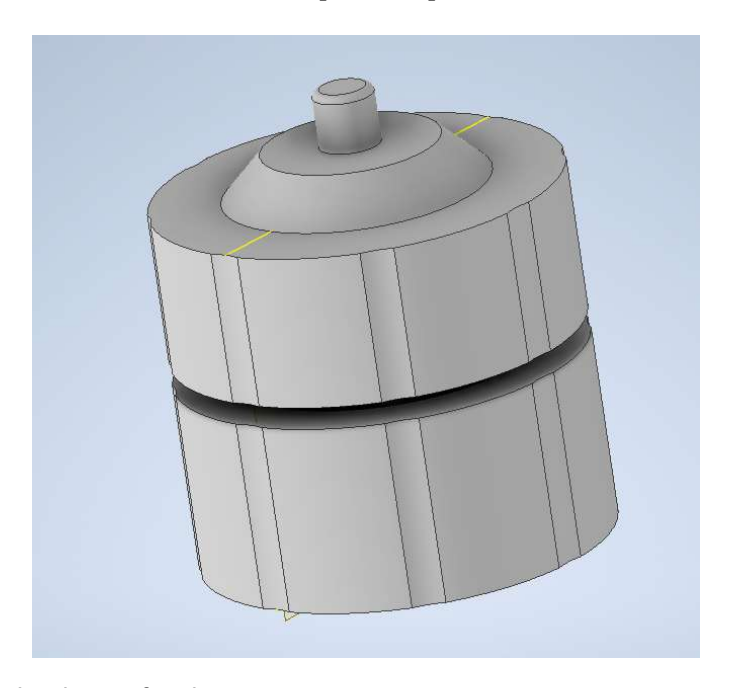


Figure 10.61: The design for the pin.

The easiest way to check the path of the laser is to used a squared paper and see wether the laser point moves up or down when moving the paper along the sample stage. If the pins gets pushed down or the plane, the laser path gets moved in is not parallel to the surface of the measuring head, see section 10.3.3, otherwise refer to section 10.3.4.

### 10.3.3 Adjustment of Pin Height

The pins have a segment that needs to be twisted to loosen the pin from the thread. It needs to be twisted in the opposite direction to set to height.

Furthermore, it may be necessary to change the angle of the laser diode or the lens to achieve a parallel beam. The screw to adjust the angle of the laser diode is located directly below the diode (figure 10.62) and the screws to adjust the orientation of the lens are located on the lens holder (figure 10.63).

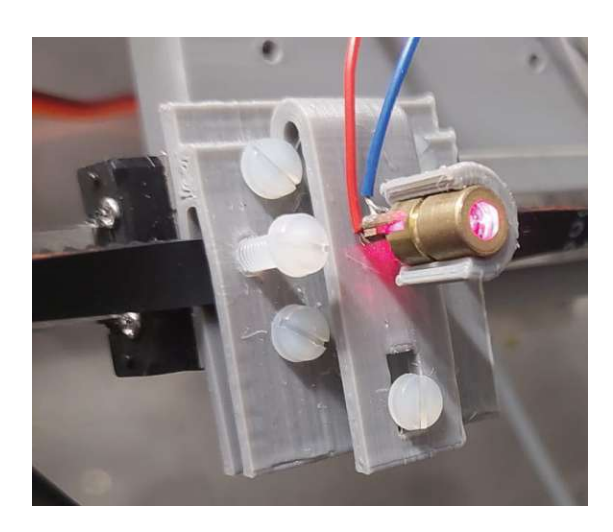


Figure 10.62: The screw is located below the diode.

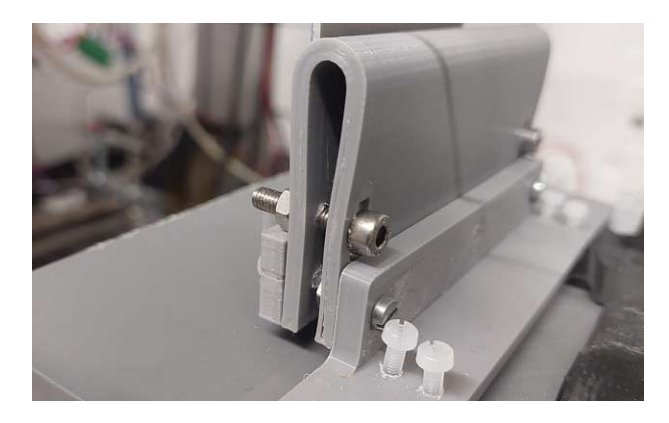


Figure 10.63: The screws are located above the lens holder.

### 10.3.4 Angle Adjustment

To check the angle of the light barrier, two commands must be used: \_set\_ymin and \_set\_ymax. These commands move the laser in the front of the measuring head and the back of the measuring head. The goal now is to change the angle until the laser is equally far away from the measuring head in both position (roughly 6mm, see figure 10.64).

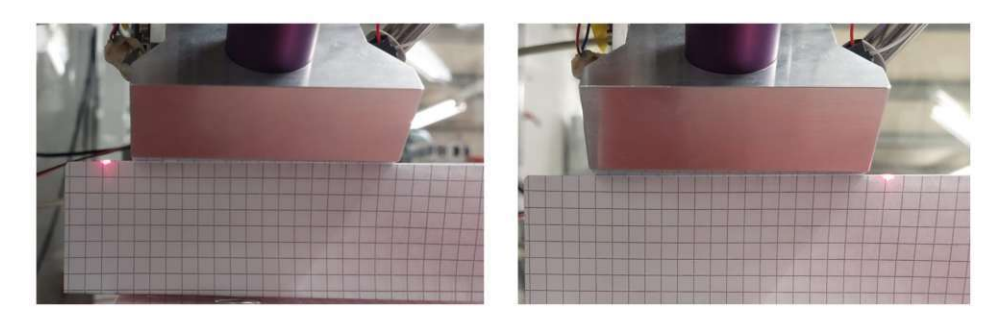


Figure 10.64: The laser position when adjusted correctly.

The angle of the light barrier can be adjusted by turning the thread seen in figure 10.60. When the correct angle is found, the wedge should be pushed below the thread to hold the rail in place.

# 11 Bibliography

- [1] Utz, A. (2012). Zweidimensionale Rntgenfluoreszenzanalyse zur Darstellung biologischer Proben in stark streuender Matrix [Diploma Thesis, Technische Universität Wien]. reposiTUm. https://resolver.obvsg.at/urn:nbn:at:at-ubtuw:1-45874
- [2] Allinger, P. (2015). High power polarized vs. low power direct EDXRF [Diploma Thesis, Technische Universität Wien]. reposiTUm. https://doi.org/10. 34726/hss.2015.27047
- [3] Klockenkaemper R., von Bohlen, A. Total - reflection X - ray fluoresenceanalytical and related methods. – Second edition. Wiley, 2015. ISBN: 978 -1-118-46027-6.
- [4] Wikipedia, the free Encyclopedia-https://en.wikipedia.org/wiki/X-ray tube# /media /File:WaterCooledXrayTube.svg
- [5] Jensen C. Improvements in low power, end – window, transmission– target X-ray tubes. MOXTEK, Inc., 2004. https://moxtek.com/wp-content/ uploads/pdfs/ improvements-in-low-power-end-window-transmission-target-xray-tubes/IMPROVEMENTS IN LOW POWER X-RAY TUBES.pdf
- [6] Tipler P. A., Mosca G., Wagner, J. Physik fuer Wissenschaftler und Ingenieure. Springer Spektrum, 2015. ISBN: 978-3-642-54165-0.
- [7] Agarwal, B.K. X - Ray Spectroscopy, An Introduction, Springer-Verlag Berlin Heidelberg GmbH, 1979. ISBN: ISBN 978-3-540-50719-2
- [8] Haschke M., Flock J., Haller  $M.X - Ray\ Fluorescence\ Spectroscopy$ for Laboratory Applications. Wiley-VCH, 2021. ISBN: 978-3-527-34463-5.
- [9] Kregsamer P., Wobrauschek P., Streli C. and Ingerle D. XRF XRP Praktikum, Technische Universität Wien, 2023
- [10]ESRF., Sourceforge PYMCA .2024, (Accessed 16.10.2024). https://pymca. sourceforge.net/download.html
- [11]IAEA., IAEA/Downloads .2024, (Accessed 16.10.2024). https://nucleusqa.iaea.org/sites/nuclear- instrumentation/Pages/Downloads.aspx

- [12]Hofstadler C. (2013) Implementation of Peak Fitting Algorithms for Energy Dispersive X-ray Fluorescence Analysis. Project work. Technische Universität Wien.
- [13] Zlabinger, J. (2022). Development of a peak deconvolution software for  $X-ray\ fluorescence\ spectra\ [Diploma\ Thesis,\ Technische\ Universit" at Wien].$ reposiTUm. https://doi.org/10.34726/hss.2022.86963
- [14] Demtröder W., Elementarphysik 2 – Elektrizitaet und Optik 7. Auflage. Springer, 2015. ISBN: 978-3-662-55789-7.
- [15] $Steimkamp\ V.\ Der\ Python-Kurs\ fuer\ Ingenieure\ und\ Naturwissenschaftler$ .Rheinwerk Verlag, 1. Auflage, 2021. isbn: 978-3-8362-7316-9.
- [16] Nasteski V. An overview of supervised machine learning methods (2017). HORIZONS.B. 4. 51-62. DOI:10.20544/HORIZONS.B.04.1.17.P05.
- [17]Amr T. W., Hands-On Machine Learning with scikit-learn and Scientific Python Toolkits. Packt Publishing, 2020. ISBN: 978-1-83882-604-8.
- [18] William R. Leo. Techniques for Nuclear and Particle Physics Experiments - A How - to Approach. Springer Verlag, 1994. isbn: 978-3-540-57280-0.
- [19]Kolanoski H., Wermes N., Teilchendetektoren - Grundlagen und Anwendungen. Springer Spektrum, 2016. isbn: 978-3-662-45349-0.
- [20]  $AMPTEK\ INC.\ Mini-X,\ Miniature\ X-Ray\ Source\ Datasheet.$ https://www.amptek.com/-/media/ametekamptek/documents/resources/ products/specs/retired/mini-x-specifications.pdf?la=en&revision=44d1bf 74-727c-47f4-a48f-db08b834ad1e&hash=29018D1771C9A1B9CAC329012396D743
- AMPTEK INC. www.amptek.com [21]
- KETEK. AXAS-D, Analytical X-ray Acquisition System. www.ketek.net. [22]
- [23]Nanotec Electronic GmbH., PD2-C  $\overset{\circ}{}$  Schrittmotor mit integriertem Controller NEMA 17.2024, (Accessed 18.09.2024). https://www.nanotec. com/eu/de/produkte/1886-pd2-c-schrittmotor-mit-integriertem-controllernema-17

147



- [24] KETEK. VITUS H150 https://www.ketek.net/wp-content/uploads/2017/01/ KETEK VITUS H150 Product Information.pdf.
- Nanotec Electronic GmbH., Plug&Drive Studio 1.2024, (Accessed 20.10.2024). [25]https://www.nanotec.com/us/en/products/2283-plug-drive-studio-1
- [26] Git Hub., Yolov 5.2024, (Accessed 18.09.2024). https://github.com/ultralytics /yolov5
- [27]Git Hub., labelImg .2024, (Accessed 18.09.2024). https://github.com /HumanSignal/labelImg
- [28] Git Hub., Achritecture Summary – Ultralytics YOLO Docs .2024, (Accessed 14.10.2024).https://docs.ultralytics.com/yolov5/tutorials/architecture description/?h=loss#4-additional-features
- [29] Hui J., mAP (mean Average Precision) for Object Detection.2018, (Accessed 18.09.2024). https://jonathan-hui.medium.com/map-mean-average-precision-for-object-detection-45c121a31173
- [30] Nanotec Electronic GmbH., NanoPro: Comissioning BLDC or Brusher Motors | Nanotec .2024, (Accessed 26.09.2024). https://www.nanotec.com/ eu/en/products/2257-nanopro
- [31] Nanotec Electronic GmbH., NanoPro: Comissioning BLDC or Brusher Motors | Nanotec - User Manual .2024, (Accessed 26.09.2024). https://www.nanotec.com/fileadmin/files/Handbuecher/Handbuecher Archiv/NanoPro /NanoPro User Manual V2.3.pdf?1656012586
- [32]National Institute of Standards and Technology (accessed 27.10.2024). Certificate of Analysis Standard Reference Material 1103 Free - Cutting Brass https://tsapps.nist.gov/srmext/certificates/archives/1103.pdf
- Wobrauschek, P., Holub, E., & Kregsamer, P. (2022, June 28). Spectral [33] Correction for Transmission X-ray Tubes for Use in the Quantification  $Software\ ATI-QUANT\ [Conference\ Presentation].\ EXRS\ 2022$  - European X-ray Spectrometry Conference, Brügge, Belgium. http://hdl.handle.net/20 .500.12708/136307

- [34] Numista.com (accessed 27.10.2024). 10 Euro Cents. https://en.numista.com/ catalogue/pieces108.html
- [35]National Institute of Standards and Technology (accessed 27.10.2024). National  $Bureau\ of\ Standards\ Standard\ Reference\ Material\ 1103\ SodaLime\ Container$ Glass. https://tsapps.nist.gov/srmext/certificates/archives/621.pdf